UC Irvine

UC Irvine Electronic Theses and Dissertations

Title

Gyrokinetic simulation of current-driven instabilities

Permalink

https://escholarship.org/uc/item/8r66p1hk

Author

McClenaghan, Joseph Timothy

Publication Date

2015

Copyright Information

This work is made available under the terms of a Creative Commons Attribution License, availalbe at https://creativecommons.org/licenses/by/4.0/

Peer reviewed|Thesis/dissertation

eScholarship.org Powered by the California Digital Library
University of California

UNIVERSITY OF CALIFORNIA,
IRVINE

Gyrokinetic simulation of current-driven instabilities

DISSERTATION

submitted in partial satisfaction of the requirements
for the degree of

DOCTOR OF PHILOSOPHY

in Physics

by

Joseph McClenaghan

Dissertation Committee:
Professor Zhihong Lin, Chair
Professor William Heidbrink
Professor Liu Chen

2015

Large portion of Chapter 4 © 2014 AIP Publishing LLC
All other materials © 2015 Joseph McClenaghan

DEDICATION

To my parents and my beautiful wife, thank you for all of the support you have given me.

TABLE OF CONTENTS

Page

LIST OF FIGURES **v**

LIST OF TABLES **vii**

ACKNOWLEDGMENTS **viii**

CURRICULUM VITAE **ix**

ABSTRACT OF THE DISSERTATION **xii**

1 Introduction **1**
- 1.1 Gyrokinetic simulation . . . 2
- 1.2 Toroidicity-induced Alfvén eigenmodes . . . 3
- 1.3 Internal kink mode in tokamaks . . . 3
- 1.4 Astrophysical jets . . . 4
- 1.5 Objectives of this thesis . . . 5

2 Gyrokinetic simulation model for kinetic MHD **7**
- 2.1 Gyrokinetic formulation with equilibrium current . . . 7
- 2.2 Equilibrium in magnetic coordinates . . . 12
- 2.3 Zonal fields . . . 13

3 Toroidicity-induced Alfvén eigenmode **16**
- 3.1 Implementing an isotropic slowing down distribution for GTC . . . 17
- 3.2 Maxwellian distribution function. . . . 18
- 3.3 Isotropic slowing down distribution function. . . . 19
- 3.4 Loading particles . . . 21
- 3.5 Calculation of β_α . . . 22
- 3.6 Numerical equilibria for ITER . . . 23
- 3.7 TAE in ITER hybrid equilibrium . . . 25
- 3.8 TAE for ITER steady state equilibrium . . . 28
- 3.9 Summary . . . 31

4 Internal kink mode in tokamaks **32**
- 4.1 Equilibrium model for kink simulations . . . 33
  - 4.1.1 Extending the simulation region to the magnetic axis . . . 36

4.2 GTC simulation of kink instability in cylindrical geometry 40
4.2.1 GTC simulations in fluid limit 40
4.2.2 GTC gyrokinetic simulations 42
4.2.3 Convergence tests 44
4.3 GTC simulations of kink instability in toroidal geometry 45
4.3.1 GTC simulations in fluid limit 45
4.3.2 GTC gyrokinetic simulations 47
4.4 GTC simulations of kink instability in DIII-D 49
4.5 Finite difference vs. finite element operator 51
4.6 Summary 53

5 Internal kink mode in astrophysical jet **54**
5.1 Model for magnetically dominated astrophysical jet 56
5.2 Structure of magnetic fields in accretion disk 57
5.3 Equilibrium model for the jet 59
5.4 Linear simulations 63
5.5 Potential mechanism for acceleration 65
5.6 Nonlinear simulations 67
5.7 Summary 69

6 Conclusions **71**

Bibliography **74**

A Shooting Method **83**
A.1 Formulation 83
A.2 Testing Eigenmode Formulation 87
A.3 Eigenmode formulation in Cylinder 88

B Finite Element method implementation for GTC **91**
B.1 Introduction 91
B.2 Calculation of triangular mesh 91
B.3 Setup of FEM equations 94

C Extending the simulation to the magnetic axis **99**
C.1 Extrapolating to the magnetic axis 100
C.2 Changes to the size of Laplacian matrix 102
C.3 New boundary conditions 104

D Increasing order of the spline algorithm for analytic equilibria **106**

LIST OF FIGURES

Page

3.1 In Panal(a), the q-profile is plotted vs. normalized poloidal flux ψ/ψ_w for both the hybrid and steady state equilibria. Panal(b) is the normalized alpha particle density n_α plotted vs. normalized poloidal flux for both scenarios. . 24

3.2 TAE growth rate and frequency for the hybrid equilibrium are plotted vs. toroidal mode number n with an alpha pressure $\beta_{\alpha 0} = 4\%$. 26

3.3 TAE growth rate and frequency for the hybrid equilibrium are plotted vs. the on-axis alpha pressure $\beta_{\alpha 0}$. A line of best fit for the growth rate which is drawn as the dashed line is projected to find the alpha pressure threshold. . 26

3.4 The electrostatic potential for toroidal mode numbers n=15,19,23 are plotted in the hybrid scenario. The last closed flux surface is shown by a solid black line, and white space represents outside of the simulation domain. 27

3.5 The poloidal harmonics m of the TAE in the hybrid equilibrium with toroidal mode numbers n=15,19,23 are plotted vs. the normalized square root of the toroidal flux ρ. 27

3.6 TAE growth rate and frequency for the steady state equilibrium are plotted vs. toroidal mode number with an alpha pressure $\beta_{\alpha 0} = 4\%$. 28

3.7 TAE growth rate and frequency for the steady state equilibrium are plotted vs. the on-axis alpha pressure $\beta_{\alpha 0}$. A line of best fit for the growth rate which is drawn as the dashed line is projected to find the alpha pressure threshold. 29

3.8 The electrostatic potential for toroidal mode numbers n=15,19,23 in the steady state scenario are plotted. The last closed flux surface is shown by a solid black line, and white space represents outside of the simulation domain. 30

3.9 The poloidal harmonics m of the TAE in the steady state equilibrium with toroidal mode numbers n=15,19,23 are plotted vs. the normalized square root of the toroidal flux ρ. The minimum of the q-profile is located at 0.4 ρ. . . . 30

4.1 The GTC laplacian operator solution and the analytic solution for F are plotted against radial coordinate, r/a. The FD boundary flux surface is drawn with a vertical dashed line. 38

4.2 The internal kink mode growth rate is plotted vs. the inverse aspect ratio r_s/R_0 of the $q = 1$ surface for cylindrical geometry. 42

4.3 The mode structure of $\delta A_\parallel$ and $\delta J_\parallel$ are plotted against the radial coordinate r/a, for the $r_s/R_0 = 0.25$ case in cylindrical geometry. 42

4.4 The mode structure of the electrostatic potential $\delta\phi$ vs. the radial coordinate r/a is plotted for the $r_s/R_0 = 0.25$ case in cylindrical geometry. 43
4.5 Panel(a): The growth rate of the internal kink mode is plotted vs. radial position of the FD boundary $r_s/R_0 = 0.25$ case. Panel(b): The GTC internal kink mode growth rate is plotted against the number of radial grid points for the $r_s/R_0 = 0.25$ case. 44
4.6 The $\delta\phi$ mode structure is plotted in the poloidal plane. The lowest-order tokamak mode structure is plotted in panel(a), and realistic tokamak model mode structure is plotted in in panel(b) 46
4.7 The growth rate vs. the ion beta β_i. 48
4.8 Internal kink mode growth rate is plotted against the kinetic effects radial cutoff, where kinetic effects are kept only outside the radial cutoff position. Inside the radial cutoff domain, the ion thermal motion is suppressed. Outside of the radial cutoff domain, all kinetic effects are kept. 48
4.9 Panel(a): The safety factor q is plotted vs. the normalized poloidal flux. Panel(b): The total pressure P_{0tot} is plotted vs. the normalized poloidal flux. 50
4.10 The poloidal cross section of $\delta\phi$ mode structure is plotted for the DIII-D equilibrium. 51
4.11 The internal kink mode structure $\delta\phi$ on the $\zeta = 0$ poloidal plane are plotted. The finite differences mode structure is plotted in panel(a), and finite element mode structure is plotted in panel(b). 52

5.1 On the left is a simplified sketch of the magnetic field structure produced by the jet that was launched by the accretion disk. On the right, various properties of the jet are plotted, including the axial current j_z, poloidal flux function ψ, and the lambda profile $\lambda = j_z/B_z$. This figure is reproduced by permission of the AAS. 57
5.2 The normalized q-profile is plotted vs. radial coordinate r/a. 60
5.3 The axial and poloidal field are plotted vs. radial coordinate r/a. The approximate analytic expressions for magnetic fields are plotted in blue and self-consistent magnetic fields in red. 62
5.4 The growth rates are plotted against the normalized axial wave number $k_z a$. 64
5.5 Panel(a): the mode structure of the electrostatic potential for the jet equilibrium with $k_\theta/k_z = 0.9$. Panel(b): the mode structure of the electrostatic potential for a typical tokamak with $k_\theta/k_z = 4$ 64
5.6 Panel(a): The nonlinear behavior of perturbed magnetic potential $\delta A_{||}$ is plotted. Panel(b): The behavior of the electrostatic potential $\delta\phi$ is plotted. . 68
5.7 The zonal parallel electric field $\overline{\delta E_{||}}$ is plotted in the radial-time space for the "parallel NL" case. 69

LIST OF TABLES

Page

3.1 On-axis values for ITER hybrid scenario operation 24
3.2 On-axis values for ITER steady state operation 24

4.1 On-axis values for DIII-D equilibrium internal kink mode simulation 50

ACKNOWLEDGMENTS

I would like to thank my thesis advisor Zhihong Lin for all of the guidance he has given me throughout graduate school. He has always been very patient, even when research progress was slow or when my writing required many revisions. His hard work ethic is inspiring and he was the initial developer of GTC, which all of the research in this thesis uses. Without him, none of the research in this thesis would be possible. I also want to thank him for providing me with many opportunities to travel and present my research at conferences and workshops. I would like to thank Hui Li and Ken Fowler for allowing me to join their research team. Their advice was vital to all of my research investigating astrophysical jets. Without their guidance and support, none of research presented in Chapter 5 would have been performed.

I thank William Heidbrink and Liu Chen for their support and their inspiration to push me to be a better researcher. I would also like to thank them for giving me quick feedback and for their understanding of the time constraints on this thesis project. Next, I would like to thank the various members of the GTC team for all of the discussions that have helped me grow as a researcher including: Wenjun Deng, Zhixuan Wang, Dan Fulton, Ihor Holod, Yong Xiao, Calvin K. Lau, Onnie Luk, Bao Jian, Animesh Kuley, Dongjian Liu, Yaqi Liu, Ge Dong, and Sam Taimourzadah.

Some text of this thesis/dissertation is a reprint of the material as it appears in (Ref[1]). The co-authors listed in this publication directed and supervised research which forms the basis for the thesis/dissertation.

I thank the American Astronomical Society and the American Institute of Physics for permission to include figures in this thesis. This work was supported by U.S. DOE SciDAC GSEP Center and DOE Grant Nos. DE-FG02-07ER54916 and DE-SC0010416, and used resources of the Oak Ridge Leadership Computing Facility at Oak Ridge National Laboratory (DOE Contract No. DE-AC05-00OR22725), and the National Energy Research Scientific Computing Center (DOE Contract No. DE-AC02-05CH11231).

CURRICULUM VITAE

Joseph McClenaghan

EDUCATION

Doctor of Philosophy in Physics and Astronomy **2015**
University of California, Irvine *Irvine, CA*

Master of Science in Physics **2012**
University of California, Irvine *Irvine, CA*

Bachelor of Science in Physics **2009**
University of California, San Diego *La Jolla, CA*

RESEARCH EXPERIENCE

Graduate Research Assistant **2011–2014**
University of California, Irvine *Irvine, California*

TEACHING EXPERIENCE

Teaching Assistant **2009–2012**
University of California, Irvine *Irvine, California*

REFEREED JOURNAL PUBLICATIONS

Verification of gyrokinetic particle simulation of current-driven instability in fusion plasmas. I. Internal kink mode
J. McClenaghan, Z. Lin, I. Holod, W. Deng, and Z. Wang. *Physics of Plamsas (1994-present)*, 21(12): 122519, 2014

Verification of gyrokinetic particle simulation of current-driven instability in fusion plasmas. II. Resistive Tearing Mode
D.J. Liu, W.L. Zhang, J. McClenaghan, J. Wang, and Z. Lin, *Physics of Plamsas (1994-present)*, 21(12): 122520, 2014

Ponderomotive acceleration by relativistic waves
C.K. Lau, P.C. Yeh, O. Luk, J. McClenaghan, T. Ebisuzaki, and T. Tajima, *Phys. Rev. ST Accel. Beams* 18, 024401, 2015

Gyrokinetic particle simulations of kink mode in astrophysical jets
J. McClenaghan, H. Li, C. Fowler, and Z. Lin, *in preparation*

REFEREED CONFERENCE PUBLICATIONS

Gyrokinetic Particle Simulation of Internal Kink Mode in Toroidal Geometry **Nov. 2011**
53rd Annual Meeting of the APS Division of Plasma Physics

GTC simulation of Internal Kink Mode **Jan. 2012**
Gyrokinetic Simulation of Energetic Particle Turbulence and Transport (GSEP) Workshop 2012

Simulation of Internal Kink Mode using GTC **Apr. 2012**
2012 International Sherwood Fusion Theory Conference

Gyrokinetic Particle Simulation of Internal Kink Mode in Toroidal Geometry **Oct. 2012**
54rd Annual Meeting of the APS Division of Plasma Physics

GTC simulation of Internal Kink Mode & kinetic-MHD **Jan. 2013**
Gyrokinetic Simulation of Energetic Particle Turbulence and Transport (GSEP) Workshop 2013

Gyrokinetic particle simulation of internal kink modes **Apr. 2013**
2013 U.S. E.U. Joint Transport Task Force Workshop

Gyrokinetic particle simulation of internal kink modes in DIII-D **Oct. 2013**
55rd Annual Meeting of the APS Division of Plasma Physics

Gyrokinetic particle simulation of internal kink modes in tokamaks **Mar. 2014**

2014 International Sherwood Fusion Theory Conference

Gyrokinetic simulations of kink modes in astrophysical jets **Oct. 2014**

56rd Annual Meeting of the APS Division of Plasma Physics

ABSTRACT OF THE DISSERTATION

Gyrokinetic simulation of current-driven instabilities

By

Joseph McClenaghan

Doctor of Philosophy in Physics

University of California, Irvine, 2015

Professor Zhihong Lin, Chair

The gyrokinetic toroidal code(GTC) capability has been extended for simulating current-driven instabilities in magnetized plasmas such as kink and resistive tearing modes with kinetic effects. This new gyrokinetic capability enables first-principles, integrated simulations of macroscopic magnetohydrodynamic(MHD) modes, which limit the performance of burning plasmas and threaten the integrity of fusion devices. The excitation and evolution of macroscopic MHD modes often depend on the kinetic effects at microscopic scales and the nonlinear coupling of multiple physical processes.

GTC simulation in the fluid limit of the internal kink modes in cylindrical geometry has been verified by benchmarking with an MHD eigenvalue code. The global simulation domain covers the magnetic axis which is necessary for simulating the macroscopic MHD modes. Gyrokinetic simulations of the internal kink modes in the toroidal geometry find that ion kinetic effects significantly reduce the growth rate even when the banana orbit width is much smaller than the radial width of the perturbed current layer at the mode rational surface. This new GTC capability for current-driven instability has now been extended to simulate fishbone instabilities excited by energetic particles and resistive tearing modes.

GTC has also been applied to study the internal kink modes in astrophysical jets that are formed around supermassive black holes. Linear simulations find that the internal kink

modes in astrophysical jets are unstable with a broad eigenmode. Nonlinear saturation amplitude of these kink modes is observed to be small, suggesting that the jets can remain collimated even in the presence of the internal kink modes. Generation of a mean parallel electric field by the nonlinear dynamics of internal kink modes and the potential implication of this field on particle acceleration in jets has been examined.

Chapter 1

Introduction

Large currents are needed to form nested magnetic surfaces for confining high temperature plasmas in axisymmetric fusion devices. These equilibrium currents often excite magnetohydrodynamic(MHD) instabilities including ideal kink modes[2] and resistive tearing modes[3]. The basic physics mechanisms of these current-driven instabilities manifest themselves in tokamak plasmas as various macroscopic MHD modes, such as fishbones [4], sawteeth[5], neoclassical tearing modes[6], and resistive wall modes[7], which can limit burning plasma performance and threaten fusion device integrity[8]. The studies of the MHD modes typically rely on MHD simulations[9, 10, 11] or reduced models[12]. However, the excitation and evolution of macroscopic MHD modes often depend on kinetic effects at microscopic scales, and on the nonlinear coupling of multiple physical processes, e.g., microturbulence, neoclassical transport, and energetic particle effects, etc. Therefore, fully self-consistent simulations require a kinetic approach to incorporate microscopic kinetic effects in these current-driven MHD modes.

In this thesis project, we have extended gyrokinetic particle simulation for current-driven MHD instabilities, and applied this new capability to study internal kink modes in both fusion plasmas and astrophysical jets.

1.1 Gyrokinetic simulation

Gyrokinetic theory is a theoretical framework which is used to model strongly magnetized plasmas for time scales longer than the ion cyclotron period and spatial scales that are comparable to the ion gyroradius[13]. Gyrokinetic theory averages over the ion cyclotron motion while maintaining finite Larmor radius effects, resulting in the averaging out of high frequency modes on the order of the ion cyclotron frequency and above, and reduces the phase space dimensionality of the particle distribution function from six to five. Since the frequency and growth rate of kinetic-MHD modes are much smaller than the ion cyclotron frequency, nonlinear gyrokinetics, which removes unwanted high frequency modes and rigorously retains all linear and nonlinear wave–particle resonances and finite Larmor radius effects, is well suited to study kinetic-MHD modes.

Gyrokinetic simulation now plays a major role in the investigation of low-frequency neoclassical and turbulent transport[14, 15], and energetic particles[16]. It has recently been extended to simulate pressure-driven kinetic-MHD processes including various Alfvén eigenmodes[17, 18]. There are two common approaches to simulating the gyrokinetic equation. The first method is the particle-in-cell method, which uses particles to sample the phase space distribution. The second is the continuum method which the gyrokinetic equation is discretized on a phase space grid. Both of these approaches have been successfully applied to study low frequency pressure-driven kinetic-MHD modes[19]. However, very few particle-in-cell simulations and no continuum simulations have attempted to study current-driven MHD modes[20, 21].

1.2 Toroidicity-induced Alfvén eigenmodes

Although this thesis project focuses on the development and application of gyrokinetic particle simulation for current-driven instabilities, I started this project with first learning the gyrokinetic particle simulation by applying Gyrokinetic Toroidal Code(GTC) to predict the stability of the toroidicity-induced Alfvén eigenmode(TAE) driven by the pressure gradient of alpha-particles in the International Thermonuclear Experimental Reactor(ITER). The pressure driven TAE is commonly observed in present tokamak experiments[22]. Unstable TAEs can lead to energetic particle transport[23, 24] that could potentially limit plasma performance in ITER. Gyrokinetic simulation has been shown to have good agreement with present experiments[18], and is currently capable of making predictions on future experiments.

1.3 Internal kink mode in tokamaks

The internal kink mode with toroidal mode number $n = 1$ and poloidal mode number $m = 1$ is an MHD perturbation that is driven unstable by the equilibrium currents in magnetized plasmas. This internal kink instability can be thought of as a rigid displacement of the plasma core[2]. While the internal kink is always MHD unstable in the cylindrical geometry[2], toroidicity[25] is thought to be able to stabilize the internal kink mode.

Internal kink modes are thought to be the trigger for the sawtooth collapse which relaxes the plasma pressure[26]. These sawtooth collapses are often observed to have $m = n = 1$ precursor and successor modes[5]. The physical interpretation is that sawtooth collapse is caused by the internal kink mode[26] or the quasi-interchange mode[27], depending on plasma parameters. One noteworthy experiment showed the characteristics of the sawtooth collapse can change from kink-like to quasi-interchange-like depending on the plasma shape[28]. One

open question is understanding the stability of the internal kink mode during the ramp phase of the sawtooth oscillations, where the on-axis safety factor is commonly observed to be well below unity[29, 30]. These kink-triggered sawtooth crashes can produce seed islands which can destabilize dangerous neoclassical tearing modes[31].

Long sawtooth free periods have been observed[32, 33] during fast ion producing ion-cyclotron-radio-frequency heating even when the on-axis safety factor can typically fall well below unity during these periods[34]. This led to theoretical explanations that fast ions can stabilize the internal kink mode through interaction with trapped ions if the fast ion energy is large enough so that the thermal ion diamagnetic frequency is much less than the fast ion precession frequency[35, 36]. However, sufficient fast ion pressure gradients can destabilize long lived saturated kink modes[37] or even excite fishbone modes[38]. These long-lived kink modes[39, 40] and fishbone modes[4, 41] have been observed to degrade fast ion confinement.

1.4 Astrophysical jets

Large plasmas in the form of powerful astrophysical jets and radial lobes are often observed near active galactic nuclei[42]. The magnetic field strength and structure that these plasma jets consist of are currently unknown. However, broadband polarized radiation which is consistent with synchrotron radiation has been observed suggesting the magnetic fields can be large[43, 44], and potentially magnetically dominated[45](i.e. kinetic energy of the jet is much less than field energy). Large currents are necessary to maintain the dynamo in proposed magnetically dominated models[46]. These currents would produce kink modes that could disrupt the jets. Understanding how kink modes nonlinearly evolve in jets is critical to understanding how the jets are capable of maintaining stability over long distances.

The source of ultra-high-energy cosmic rays with energies up to 10^{20} eV is currently unknown. These cosmic rays most likely originate within the Virgo Supercluster due to the Greisen-Zatsepin-Kuzmin limit, which limits the distance that ultra-high-energy cosmic rays can travel due to interaction with the cosmic microwave background[47, 48]. For this reason, astrophysical jets have been suggested as a possible source of ultra-high-energy cosmic rays[49]. The mechanism that could produce cosmic rays in the jet with such high energies is currently unknown as they cannot be explained through relativistic shocks in jets by conventional Fermi acceleration[50, 51].

1.5 Objectives of this thesis

First using the mature gyrokinetic capabilities of pressure-driven kinetic-MHD instabilities, predictions of the toroidicity-induced Alfvén eigenmodes instabilities thresholds are performed for the steady state and hybrid ITER operation scenarios[52, 53]. In these simulations, it is found that with the fast alpha particle pressure, TAEs are near the stability threshold for both scenarios. When beam ions are considered, these TAEs should be very unstable for these operation scenarios.

Next, we extend the GTC[54, 55] capability for simulating internal kink modes, for the first time, with kinetic effects in the toroidal geometry. The implementation of the equilibrium current and the verification of its effects on reversed shear Alfvén eigenmode[56] enable GTC simulation of current-driven instabilities, such as kink modes reported in this thesis, tearing modes, and fishbone modes. In the present work, we first extend the simulation domain to magnetic axis for global kink simulation. We then verify GTC simulations of internal kink modes in the cylindrical geometry by benchmarking with an MHD eigenvalue code. Finally, GTC gyrokinetic simulations of internal kink modes in the toroidal geometry find that ion

kinetic effects significantly reduce the growth rate even when the banana orbit width is much smaller than the radial width of the perturbed current layer.

Lastly, using the GTC capability to simulate kink modes, kink mode simulations in an astrophysical jet equilibrium are performed. With the structure of the magnetic fields in the accretion disk derived in Colgate et al.[46], a potential magnetic equilibrium for the jet is constructed. With this equilibrium, the linear stability properties of internal kink mode in the jet are examined where they are found to be unstable. Nonlinear saturation of the kink mode is examined, finding that parallel nonlinearity and zonal flows can play an important role in the saturation. A brief discussion is then given on the internal kink mode being able to create a flux surface averaged parallel electric field which can accelerate particles to large energies.

The structure of this thesis is as follows. In chapter 2, the gyrokinetic simulation model used in GTC will be described. Using the mature kinetic-MHD capabilities for studying pressure-driven modes, GTC will be used to simulate toroidal Alfvén eigenmodes in potential ITER running scenarios in chapter 3. In chapter 4, the simulation capabilities are extended to the magnetic axis, and GTC simulations of the internal kink mode are verified in the cylindrical and the toroidal geometry with kinetic effects. In chapter 5, internal kink mode simulations are performed in an astrophysical jet-like magnetic field configuration. Conclusions and discussions are given in chapter 6.

Chapter 2

Gyrokinetic simulation model for kinetic MHD

2.1 Gyrokinetic formulation with equilibrium current

In the section, the gyrokinetic equations that are used in GTC are described. Using δ as a smallness parameter, the gyrokinetic ordering is [57, 13],

$$\frac{\omega}{\Omega_i} \sim k_\parallel \rho_i \sim \frac{\delta B}{B_0} \sim k_\perp \rho_i \frac{e\delta\phi}{T} \sim \mathcal{O}(\delta). \tag{2.1}$$

The variables ω, $k_\parallel$, and $k_\perp$ are wave frequency, parallel wave vector, and perpendicular wave vector of the mode of interest; Ω_i, ρ_i, and B_0 are ion cyclotron frequency, ion Larmor radius, and equilibrium magnetic field; δB, $\delta\phi$, and T are perturbed magnetic field, perturbed electrostatic potential, and plasma temperature.

Since the electron mass is much smaller than the ion mass, the electron dynamics are on a much faster time scale compared to the ion dynamics. Due to the computational time constraints, it is often impractical to calculate the brute force electron dynamics for macroscopic MHD modes. This motivated the fluid-kinetic hybrid electron model in which the electron distribution function is expanded using the smallness parameter of the ratio of wave frequency to electron transit frequency[58]. In the zeroth order, the electrons are adiabatic and can be described by the continuity equation(i.e., massless electron model). Nonadiabatic responses are treated kinetically in the higher order. However, in this thesis only massless electrons will be considered since the important kinetic effects(finite orbit width, wave-particle resonances, and polarization drift) on the kink instability are mostly contributed by ions. The fluid-kinetic hybrid electron model removes collisionless tearing mode physics from the simulation, and avoids well known numerical difficulties associated with tearing mode physics[59]. In extension to this model, GTC simulations of resistive tearing modes using the fluid electron model with a resistivity term have recently been verified[60]. The collisionless tearing mode using a finite-mass electron model has also been verified[61].

Starting with the electron fluid and field equations for the fluid-kinetic hybrid model, the nonlinear continuity equation which can be derived from the drift kinetic equation is[56]:

$$
\begin{aligned}
&\frac{\partial n_e}{\partial t} + \mathbf{B_0}\cdot\nabla\left(\frac{n_{0e}\delta u_{\parallel e}}{B_0}\right) + B_0\mathbf{v_E}\cdot\nabla\left(\frac{n_{0e}}{B_0}\right) - \\
&n_{0e}(\delta\mathbf{v_{*e}} + \mathbf{v_E})\cdot\frac{\nabla B_0}{B_0} + \delta\mathbf{B}\cdot\nabla\left(\frac{n_{0e}u_{\parallel 0e}}{B_0}\right) + \\
&\frac{c\nabla\times\mathbf{B_0}}{B_0^2}\cdot\left[-\nabla\delta P_{\parallel e} + n_{0e}\nabla\delta\phi\right] + \\
&\delta\mathbf{B}\cdot\nabla\left(\frac{n_{0e}\delta u_{\parallel e}}{B_0}\right) + B_0\mathbf{v_E}\cdot\nabla\left(\frac{\delta n_e}{B_0}\right) + \\
&\frac{c\delta n_e}{B_0^2}\mathbf{b}_0\times\nabla B_0\cdot\nabla\delta\phi + \frac{c\delta n_e}{B_0^2}\nabla\times\mathbf{B}_0\cdot\nabla\delta\phi = 0,
\end{aligned}
\tag{2.2}
$$

where the electron density n_e and the electron parallel flow $u_{||e}$ are split into the equilibrium and perturbed quantities: $n_e = n_{0e} + \delta n_e$ and $u_{||e} = u_{||0e} + \delta u_{||e}$. The drift velocities are defined as $\mathbf{v_E} = \frac{c\mathbf{b}_0 \times \nabla \delta\phi}{B_0}$ and $\mathbf{v_{*e}} = \frac{\mathbf{b}_0 \times \nabla \left(\delta P_{||e} + \delta P_{\perp e}\right)}{n_{0e} B_0}$, where $\mathbf{b}_0$ is the unit vector along the direction of the equilibrium magnetic field, $\delta P_{||e}$ and $\delta P_{\perp e}$ are the parallel and perpendicular perturbed electron pressure, and c is the speed of light.

Using the Padé approximation, the gyrokinetic Poisson equation is[57]:

$$\frac{c^2}{4\pi v_A^2} \nabla_\perp^2 \delta\phi = -(1 - \rho_i^2 \nabla_\perp^2)(Z_i \langle \delta n_i \rangle - \delta n_e), \tag{2.3}$$

where $\langle A \rangle$ denotes the gyro-averaging of any function A. The term $\langle \delta n_i \rangle$ is the perturbed gyro-averaged ion density, v_A is the Alfvén velocity, and Z_i is the ion charge. Gyrokinetic Ampere's law is used to calculate the electron perturbed current,

$$n_{0e} e \delta u_{\|e} = \frac{c}{4\pi} \nabla_\perp^2 A_\| + Z_i n_{0i} \langle \delta u_{\|i} \rangle. \tag{2.4}$$

The variable $\langle \delta u_{||i} \rangle$ is the perturbed parallel ion flow. The perturbed magnetic potential $\delta A_{||}$, defined as $\delta \mathbf{B} = \nabla \times \delta A_\| \mathbf{b}_0$, is calculated from:

$$\frac{\partial \delta A_{||}}{\partial t} = -\mathbf{b}_0 \cdot (\delta\phi - \delta\phi_{eff}), \tag{2.5}$$

where the effective scalar potential, which describes the parallel electric field ($\delta E_{||} = \mathbf{b}_0 \cdot \nabla \phi_{eff}$), in the lowest order is:

$$\delta\phi_{eff} = eT_e \frac{\delta n_e}{n_{0e}} - \frac{\delta\psi}{n_{0e}} \frac{\partial n_{0e}}{\partial \psi_0}. \tag{2.6}$$

This effective potential comes from the non-ideal MHD effects(e.g. ion polarization drift, wave-particle interactions, etc). The parallel and perpendicular perturbed electron pressure in the lowest order are:

$$\delta P_{||e} = \delta P_{\perp e} = n_{0e} e \delta\phi_{eff} + \frac{\partial (n_{0e} T_e)}{\partial \psi_0} \delta\psi, \tag{2.7}$$

where ψ_0 and $\delta\psi$ are the equilibrium and perturbed poloidal flux, respectively.

When ion kinetic effects are suppressed and parallel electric field is set to zero, Equations 2.2-2.7 form a closed system, which will be referred to as GTC fluid simulation from now on. In this fluid limit, the $\mathbf{v}_E$ terms in the electron continuity equation are removed because they cancel out with the ions. This set of equations have been shown to recover reduced MHD[56].

To incorporate the kinetic effects from the ions, the ion flow $\langle \delta u_i \rangle$ and the ion density $\langle \delta n_i \rangle$ are calculated using the gyrokinetic equation.

$$\frac{d}{dt} f_i(\mathbf{X}, \mu, v_{||}, t) \equiv \left[\frac{\partial}{\partial t} + \dot{X} \cdot \nabla + \dot{v}_{||} \frac{\partial}{\partial v_{||}} \right] f_i = 0 \tag{2.8}$$

The term f_i is the ion gyrocenter distribution function, $\dot{\mathbf{X}}$ is the position of the gyrocenter, $v_{||}$ is the velocity parallel to the magnetic field, and μ is the magnetic moment.

The ion gyrocenter motion is governed by:

$$\dot{\mathbf{X}} = v_{\|}\mathbf{b} + \mathbf{v}_E + \mathbf{v}_d, \tag{2.9}$$

$$\dot{v}_{\|} = -\frac{1}{m_i}\frac{\mathbf{B}^*}{B_0} \cdot (\mu \nabla B_0 + Z_i \nabla \delta\phi) - \frac{Z_i}{m_i}\frac{\partial \delta A_{\|}}{\partial t}, \tag{2.10}$$

where m_i is the ion mass. The magnetic field is:

$$\mathbf{B}^* = \mathbf{B}_0^* + \boldsymbol{\delta B} = \mathbf{B}_0 + \frac{B_0 v_{\|}}{\Omega_i}\nabla \times \mathbf{b}_0 + \boldsymbol{\delta B}, \tag{2.11}$$

where magnetic drift velocity $\mathbf{v}_d$ is the sum of the curvature drift $\mathbf{v}_c$ and grad-B drift $\mathbf{v}_g$,

$$\mathbf{v}_d = \mathbf{v}_c + \mathbf{v}_g = \frac{v_{\|}^2}{\Omega_i}\nabla \times \mathbf{b}_0 + \frac{\mu}{m_i \Omega_i}\mathbf{b}_0 \times \nabla B_0. \tag{2.12}$$

Note that the equations presented in this section describe the full nonlinear equations of the gyrokinetic ion/hybrid electron model. All nonlinear terms are dropped for linear simulations.

2.2 Equilibrium in magnetic coordinates

In this section, a brief description of the equilibrium model is given. GTC uses a magnetic flux coordinate system (ψ, θ, ζ), where ψ is the poloidal magnetic flux, θ is the poloidal angle, and ζ is the toroidal angle. The covariant and contravariant representations of the magnetic field and the Jacobian $\mathcal{J}$ are shown below,[62]

$$\begin{aligned} \mathbf{B}_0 &= g(\psi)\nabla\zeta + I(\psi)\nabla\theta \\ &= q\nabla\psi \times \nabla\theta - \nabla\psi \times \nabla\zeta, \end{aligned} \tag{2.13}$$

$$\mathcal{J}^{-1} = \nabla\psi \cdot (\nabla\theta \times \nabla\zeta) = \frac{B_0^2}{gq + I}. \tag{2.14}$$

The parameters q, g, and I are the safety factor, poloidal current, and toroidal current, respectively. Using the covariant representation of the magnetic field, the equilibrium current density can be written as:

$$\nabla \times \mathbf{B}_0 = g'\nabla\psi \times \nabla\zeta + I'\nabla\psi \times \nabla\theta. \tag{2.15}$$

2.3 Zonal fields

Turbulence-driven fluctuating zonal fields and flows are important in the saturation and nonlinear dynamics of kinetic-MHD modes[63, 64]. To describe zonal flows, quantities are broken into their zonal and non-zonal components:

$$A = \widetilde{A} + \overline{A}, \tag{2.16}$$

where $\widetilde{A}$ represents the non-zonal, and $\overline{A}$ represents the zonal component of a quantity A. Zonal fields are defined as the flux average of a field:

$$\overline{A} = \frac{\int J \mathrm{d}\theta \mathrm{d}\zeta A}{\int J \mathrm{d}\theta \mathrm{d}\zeta}. \tag{2.17}$$

Using the Padé approximation, the zonal component of gyrokinetic Poisson equation can be written as[55]:

$$\frac{n_i Z_i^2}{m_i \Omega_i^2} \nabla_\perp^2 \overline{\delta\phi} = -\left(1 - \rho_i^2 \nabla_\perp^2\right) Z_i \overline{\delta n_i}. \tag{2.18}$$

The zonal component of Ampere's law is[55]:

$$\overline{A_{||}} = -\delta_e^2 \frac{4\pi n_0}{c} \left(Z_i \overline{\delta u_{||i}} - e\overline{\delta u_{||e}}\right). \tag{2.19}$$

To calculate the adiabatic component of $\overline{\delta u_{||e}}$ correctly with the hybrid electron model, $\mathcal{L}_2 f_0$ corrections to the electron gyrokinetic equation must be retained, where $\mathcal{L}_2$ is the second order term in the gyrokinetic propagator. This process was done in detail in the thesis of Z. Wang[64], and a summary of the derivation is given here. The adiabatic response of the electrons is derived from the lowest order of the electron drift-kinetic equation, which is split into non-zonal and zonal components $\delta f^{(0)} = \widetilde{\delta f^{(0)}} + \overline{\delta f^{(0)}}$.

The lowest order terms in the gyrokinetic equation for the electrons are:

$$\frac{\partial}{\partial t}\overline{\delta f^{(0)}} + v_{||}\mathbf{b}\cdot\nabla\widetilde{\delta f^{(0)}} + \quad v_{||}\frac{\delta\mathbf{B}}{B_0}\cdot f_0 - v_{||}\frac{f_0 e}{T_e}\left(\mathbf{b}\cdot\nabla\delta\phi + \frac{1}{c}\frac{\partial}{\partial t}\overline{\delta A_{||}} + \frac{\delta\mathbf{B}}{B_0}\cdot\nabla\delta\phi\right) = 0. \quad (2.20)$$

Taking the zonal components of this equation and noting that $\overline{\delta\mathbf{B}\cdot\nabla f_0} = 0$, the gyrokinetic equation reduces to:

$$\frac{\partial}{\partial t}\overline{\delta f^{(0)}} + v_{||}\frac{f_0 e}{T_e}\left(-\frac{1}{c}\frac{\partial}{\partial t}\overline{\delta A_{||}} - \overline{\frac{\delta\mathbf{B}}{B_0}\cdot\delta\phi}\right) = 0. \quad (2.21)$$

This equation has the solution of

$$\overline{\delta f^{(0)}} = v_{||}\frac{f_0 e}{cT_e}\overline{\delta A_{||}^{l}}, \text{ where } \begin{cases} \overline{\delta A_{||}^{l}} \equiv \overline{\delta A_{||}} - \overline{\delta A_{||}^{nl}} \\ \overline{\delta A_{||}^{nl}} \equiv c\int \overline{\frac{\delta\mathbf{B}}{B_0}\cdot\nabla\delta\phi} \end{cases} \quad (2.22)$$

Plugging $\delta f^{(0)}$ into Ampere's Law:

$$\begin{aligned}\overline{\delta A_{||}} &= -\delta_e^2 \frac{4\pi n_0 Z_i}{c} \overline{\delta u_{||i}} - c \int \overline{\frac{\delta \mathbf{B}}{B_0} \cdot \nabla \delta\phi}\, \mathrm{d}t \\ &\approx -c \int \overline{\frac{\delta \mathbf{B}}{B_0} \cdot \nabla \delta\phi}\, \mathrm{d}t,\end{aligned} \tag{2.23}$$

where δ_e is the electron skin depth, which is very small for the simulations in this thesis, and can be ignored. Taking the time derivative of Equation 2.23, the zonal parallel electric field is:

$$\overline{\delta E_{||}} = \frac{1}{c} \frac{\partial \overline{A_{||}^{nl}}}{\partial t} = \overline{\frac{\delta \mathbf{B}}{B_0} \cdot \nabla \phi} = \overline{\frac{\mathbf{b}}{c} \cdot (\mathbf{v}_E \times \delta \mathbf{B})}. \tag{2.24}$$

Chapter 3

Toroidicity-induced Alfvén eigenmode

In this chapter, two advanced scenarios for the International Thermonuclear Experimental Reactor(ITER) which attempt to improve upon the well known ELMy H-mode scenario[52] will be examined. The hybrid scenario has a lower plasma current than the H-mode scenario and a low magnetic shear. With the low magnetic shear, the hybrid scenario minimizes the threat to the dangerous neoclassical tearing modes and has shown higher energy confinement than the H-mode scenario in current experiments[52, 53]. The steady state scenario operates at an even lower plasma current which is driven non-inductively to allow for a sustained steady state operation[52, 53].

The toroidicity-induced Alfvén eigenmode(TAE) is commonly observed in present tokamak experiments[22]. TAEs could be potentially driven unstable by the presence of energetic beam ions and the alpha particles produced by fusion reactions in ITER. Unstable TAEs can lead to energetic particle transport that limits plasma performance[23, 24]. Understanding the role of TAEs in the various ITER scenarios is critical in predicting the overall performance of ITER.

Toroidal mode number scans and alpha pressure β_α scans of the TAE are performed for a hybrid scenario equilibrium and a steady state scenario equilibrium using Gyrokinetic Toroidal Code(GTC). The destabilization of TAEs can be influenced by the fast alpha particle distribution, which is non-Maxwellian. In this work, GTC treats ions and alpha particles gyrokinetically, and the electrons as a massless fluid. To treat the alpha particles more realistically, an isotropic slowing down alpha particle distribution was implemented.

3.1 Implementing an isotropic slowing down distribution for GTC

In this section, the implementation of the isotropic slowing down distribution function for fast alpha particles into GTC is discussed. To implement a slowing down distribution into GTC, there are two places that require change: the fast ion gyrokinetic weight equation and the fast ion particle loading. The gyrokinetic weight equation used in GTC for a general distribution function is:

$$\begin{aligned}\frac{dw_\alpha}{dt} =&(1-w_\alpha)\Bigg[-\left(v_\parallel\frac{\delta\mathbf{B}}{B_0}+\mathbf{v}_E\right)\cdot\frac{\nabla f_{0\alpha}}{f_0}\bigg|_\mu+\\ &\left(\mu\frac{\delta\mathbf{B}}{B_0}\cdot\nabla B_0+Z_\alpha\frac{\mathbf{B}^*}{B_0}\cdot\nabla\delta\phi+\frac{Z_\alpha}{c}\frac{\partial A_{||}}{\partial t}\right)\left(\frac{1}{m_\alpha f_{0\alpha}}\frac{\partial f_{0\alpha}}{\partial v_\parallel}\right)\Bigg],\end{aligned} \tag{3.1}$$

where $f_{0\alpha}$ is the equilibrium distribution, and $w_\alpha = \delta f_\alpha / f_{0\alpha}$ is the perturbed distribution divided by the equilibrium distribution, $v_{||}$ and μ are the parallel velocity and the magnetic moment, respectively. The perturbed fields $\delta A_{||}$, $\delta\phi$, and $\delta\mathbf{B}$ are the magnetic vector potential, electrostatic potential, and magnetic field, respectively. Here, v_E is the E x B drift velocity, B_0 is the equilibrium magnetic field, Z_α is the ion atomic number, and m_α is

the mass of the ion. The term c is the speed of light and the modified magnetic field $\mathbf{B}^*$ is defined by Eq. 2.11. The dependence of $f_{0\alpha}$ in the weight equation only appears in $\nabla f_{0\alpha}$ and $\frac{\partial f_{0\alpha}}{\partial v_\parallel}$, so these are the only two quantities that require change in the weight equation.

3.2 Maxwellian distribution function.

Before deriving the weight equation for the slowing down distribution, we will re-derive the weight equation for the Maxwellian distribution which has been previously implemented into GTC and documented in Holod et al[55]. This will allow for comparison between the Maxwellian and slowing down distributions, and for understanding what changes need to be made to implement the slowing down distribution. The Maxwellian distribution function is:

$$f_{0\alpha} = \frac{n_{0\alpha}}{(2\pi T_{0\alpha}/m_\alpha)^{3/2}} \exp\left[-\frac{2\mu B_0 + v_\parallel^2}{2T_{0\alpha}}\right], \tag{3.2}$$

where $n_{0\alpha}$ is the alpha density, and $T_{0\alpha}$ is the alpha temperature. In this derivation, the derivatives holding μ constant will be rewritten as derivatives holding $v_\perp$ constant because equilibrium distribution formulation is written as a bi-Maxwellian in $v_\parallel$ and $v_\perp$. The normalized gradient of $f_{0\alpha}$ is:

$$\begin{aligned}\left.\frac{\nabla f_{0\alpha}}{f_{0\alpha}}\right|_\mu &= \left.\frac{\nabla f_{0\alpha}}{f_{0\alpha}}\right|_{v_\perp} - \frac{\mu}{T_{0\alpha}}\nabla B_0 \\ &= \frac{1}{n_{0\alpha}}\frac{\partial n_{0\alpha}}{\partial \psi}\nabla\psi - \frac{\mu}{T_{0\alpha}}\nabla B_0,\end{aligned} \tag{3.3}$$

and the derivative with respect to parallel velocity is

$$\frac{1}{f_{0\alpha}}\frac{\partial f_{0\alpha}}{\partial v_{\parallel}} = -m_\alpha v_{\parallel\alpha}/T_\alpha. \tag{3.4}$$

Plugging in the derivatives, the same form of the gyrokinetic equation as Holod et al.[55] is obtained.

$$\begin{aligned}\frac{dw_\alpha}{dt} =&(1-w_\alpha)\Bigg[-\left(v_\parallel\frac{\delta\mathbf{B}}{B_0}+\mathbf{v}_E\right)\cdot\left(\frac{1}{n_{0\alpha}}\frac{\partial n_{0\alpha}}{\partial\psi}\nabla\psi-\frac{\mu}{T_{0\alpha}}\nabla B_0\right)\\ &-\left(\mu\frac{\delta\mathbf{B}}{B_0}\cdot\nabla B_0+Z_\alpha\frac{\mathbf{B}^*}{B_0}\cdot\nabla\phi+\frac{Z_\alpha}{c}\frac{\partial A_{||}}{\partial t}\right)\left(v_{\parallel\alpha}/T_\alpha\right)\Bigg]\\ =&(1-w_\alpha)\Bigg[-\left(v_\parallel\frac{\delta\mathbf{B}}{B_0}+\mathbf{v}_E\right)\cdot\left(\frac{1}{n_{0\alpha}}\frac{\partial n_{0\alpha}}{\partial\psi}\nabla\psi\right)\\ &+\frac{Z_\alpha}{T_\alpha}v_\parallel E_\parallel-\frac{Z_\alpha}{T_\alpha}\mathbf{v}_d\cdot\nabla\phi\Bigg]\end{aligned} \tag{3.5}$$

3.3 Isotropic slowing down distribution function.

Repeating the same process as Section 3.2 for the slowing down distribution, the gradient and parallel velocity of $f_{0\alpha}$ are calculated. The slowing down distribution function is defined as:

$$f_{0\alpha} = \frac{dn_{0\alpha}H(v_0-v)}{(v^3+v_c^3)}, \tag{3.6}$$

where $d = \frac{3}{4\pi \ln\left((v_0^3+v_c^3)/v_c^3\right)}$ is a normalization factor, v_c is the critical velocity, and v_0 is the birth velocity. The variable H is the Heaviside function, and the particle speed is $v = \sqrt{v_\parallel^2 + 2\mu B_0}$. The gradient and parallel velocity derivative are show below.

$$\left.\frac{\nabla f_{0\alpha}}{f_{0\alpha}}\right|_\mu = \left.\frac{\nabla f_{0\alpha}}{f_{0\alpha}}\right|_{v_\perp} - \frac{1}{m_\alpha}\frac{3\mu v}{v^3+v_c^3}\nabla B_0, \qquad \text{when } v \le v_0 \tag{3.7}$$

$$\frac{1}{f_{0\alpha}}\frac{\partial f_{0\alpha}}{\partial v_\parallel} = -\frac{1}{m_\alpha}\frac{3v_\parallel v}{v^3+v_c^3}, \qquad \text{when } v \le v_0 \tag{3.8}$$

Since these derivatives are undefined when the particle velocity is greater than the birth velocity $v > v_0$, for simplicity the derivatives when $v > v_0$ will be set to the derivatives when $v = v_0$.

$$\left.\frac{\nabla f_{0\alpha}}{f_{0\alpha}}\right|_\mu = \left.\frac{\nabla f_{0\alpha}}{f_{0\alpha}}\right|_{v_\perp} - \frac{1}{m_\alpha}\frac{3\mu v_0}{v_0^3+v_c^3}\nabla B_0, \qquad \text{when } v > v_0 \tag{3.9}$$

$$\frac{1}{f_{0\alpha}}\frac{\partial f_{0\alpha}}{\partial v_\parallel} = -\frac{1}{m_\alpha}\frac{3v_\parallel v_0}{v_0^3+v_c^3}, \qquad \text{when } v > v_0 \tag{3.10}$$

Plugging the derivatives into equation 3.5, the gyrokinetic equation for a slowing down distribution function is obtained.

$$\frac{dw_\alpha}{dt} = (1-w_\alpha)\left[-\left(v_\parallel \frac{\delta \mathbf{B}}{B_0} + \mathbf{v}_E\right)\cdot\left(\frac{1}{n_{0\alpha}}\frac{\partial n_{0\alpha}}{\partial \psi}\nabla\psi\right) + \left(Z_\alpha v_\parallel E_\parallel - Z_\alpha \mathbf{v}_d\cdot\nabla\phi\right)\left(\frac{3v}{v^3+v_c^3}\right)\right] \tag{3.11}$$

The only difference between the weight equation for the slowing down and Maxwellian distribution is that $\frac{Z_\alpha}{T_\alpha}$ term for the Maxwellian distribution function is replaced by $\left(\frac{3v}{v^3+v_c^3}\right)$ for the slowing down distribution.

3.4 Loading particles

For the particle in cell method, the marker particles need to be loaded into the proper distribution. For the Maxwellian distribution loading, a clever method is to invert the cumulative distribution to obtain the appropriate random variable distribution. While a similar method could be used for an isotropic slowing down distribution, it would be cumbersome to apply such a method to more complicated distributions. A Monte Carlo method is used for loading particles in an isotropic slowing down distribution in velocity space, and can be extended to more complicated distributions in the future. The idea of this Monte Carlo method is that a particle is given a random initial velocity, and if the velocity satisfies the conditions of the slowing down distribution, the particle is kept. If the particle is found to be outside the distribution, the particle is thrown away.

Random numbers are generated for total velocity $v = [0, v_0]$, the velocity space spherical polar angle(i.e., the angle from the magnetic field vector to the velocity vector) $\theta_v = [0, \pi]$,

and the slowing down distribution $F = [0, F_{max}]$, where $F_{max} = v_0^2/(v_0^3 + v_c^3)$. If the following condition is met with the randomly generated variables:

$$v^2 \sin\theta_v \frac{1}{(v^3 + v_c^3)} \leq F, \tag{3.12}$$

then particle is kept. Note that the $v^2 \sin\theta_v$ term is the spherical Jacobian in velocity space. The quantities used in GTC $\sqrt{\mu}$ and $\rho_{||}$ are calculated.

$$\begin{aligned} \rho_{||} &= v\cos(\theta_v)\frac{m_\alpha}{q_\alpha B_0} \\ \sqrt{\mu} &= v\sin(\theta_v)\frac{m_\alpha}{2B_0} \end{aligned} \tag{3.13}$$

This method can be extended for anisotropic distributions in the future, but would require more random variables due to coupling between real-space and velocity-space variables.

3.5 Calculation of β_α

The fast ion pressure drive β_α is an important property for determining the stability properties for the TAE. The fast ion β_α is defined as the ratio of fast ion kinetic pressure to magnetic pressure, which can be calculated by the following equation:

$$\beta_{\alpha 0} = \frac{2\mu_0 n_{\alpha 0}}{B_{0a}^2} T_{\alpha eff}, \tag{3.14}$$

where the effective fast ion temperature $T_{\alpha eff}$ is defined as:

$$T_{\alpha eff} = \int_0^{v_0} v^2 1/3 m_\alpha v^2 f \, dv. \tag{3.15}$$

For the Maxwellian distribution, this integral equation reduces to T_α. While it is possible to calculate $T_{\alpha eff}$ analytically for the slowing down distribution, the calculation does not come out as neatly as the Maxwellian case. It is best to perform this integral numerically.

3.6 Numerical equilibria for ITER

In this section, the equilibria for two advanced ITER scenarios are given. These ITER equilibrium profiles were obtained using the time dependent tokamak transport analysis code TRANSP[65] to simulate an ITER hybrid operation scenario case and an ITER steady operation scenario case. Then using the Variational Moments Equilibrium Code(VMEC)[66], the data was translated into the spdata format for GTC. In Figure 3.1, the q-profile and fast alpha profile for a hybrid and steady state scenario are shown. The hybrid scenario has a low magnetic shear. Having a larger q-profile, the steady state scenario operates at a lower plasma current, and is characterized by a strong reversed shear.

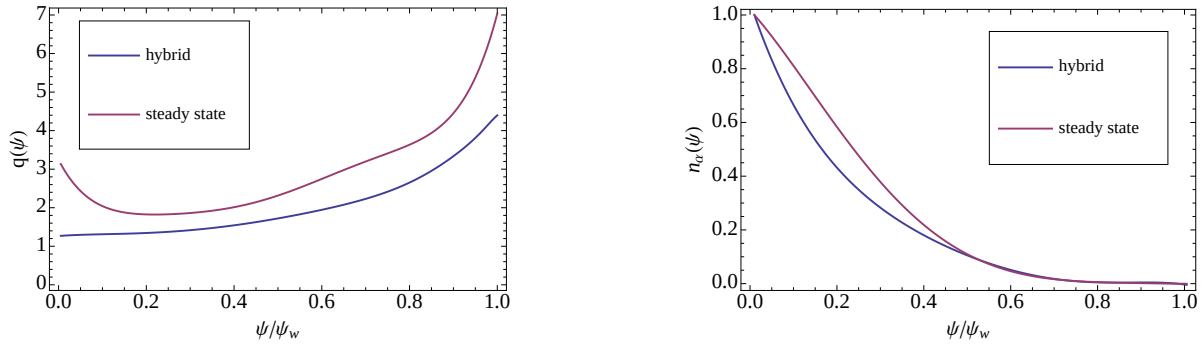

Figure 3.1: In Panal(a), the q-profile is plotted vs. normalized poloidal flux ψ/ψ_w for both the hybrid and steady state equilibria. Panal(b) is the normalized alpha particle density n_α plotted vs. normalized poloidal flux for both scenarios.

The numerical values for various physical quantities at the magnetic axis are given in Table 3.1 for the hybrid scenario and Table 3.2 for the steady state scenario. At the magnetic axis, B_{0a} is the magnetic field, R_{0a} is the major radius, n_{0ea} is the electron density, v_A is the Alfvén velocity. Note that while the size and shape of the device is the same for both equilibria, the on-axis major radii are different due to the Shafranov shift.

Hybrid equilibrium	
B_{0a}	5.03 T
R_{0a}	6.43 m
n_{0ea}	1.05×10^{20} m^{-3}
T_{0ea}	25000 eV
v_0	1.82 v_A
v_c	0.48 v_0

Table 3.1: On-axis values for ITER hybrid scenario operation

Steady state equilibrium	
B_{0a}	4.76 T
R_{0a}	6.62 m
n_{0e}	0.7×10^{20} m^{-3}
T_{0e}	25000 eV
v_0	1.48 v_A
v_c	0.57 v_0

Table 3.2: On-axis values for ITER steady state operation

3.7 TAE in ITER hybrid equilibrium

In this section, simulations of the hybrid scenario in ITER are discussed. The on-axis alpha particle pressure for this equilibrium is $\beta_{\alpha 0} = 0.94\%$. Different toroidal mode numbers are examined to determine what is the most unstable mode for this scenario. In Figure 3.2, a toroidal mode number scan is shown with an enhanced fast alpha pressure of $\beta_{\alpha 0} = 4\%$ to observe a clearly unstable mode. Different toroidal mode numbers all have similar growth rates for the range of toroidal mode numbers n in this scan, however the $n = 19$ mode growth rate is slightly larger.

Next, using the most unstable toroidal mode $n = 19$, the fast alpha pressure $\beta_{\alpha 0}$ is adjusted to find the stability threshold of the plasma. Figure 3.3 shows the hybrid scenario $n = 19$ TAE frequency and growth rate for different values of the on-axis $\beta_{\alpha 0}$. When $\beta_{\alpha 0}$ is adjusted, the TAE frequency remains approximately constant near $\omega = 0.03\,\omega_A$. The growth rate of the TAE is approximately a linear function with respect to $\beta_{\alpha 0}$. Using a line of best fit, the growth rate is projected to find the approximate threshold required to excite the instability. The $n = 19$ TAE is found to be marginally stable for the hybrid equilibrium with a threshold of about $\beta_{\alpha 0} = 1\%$.

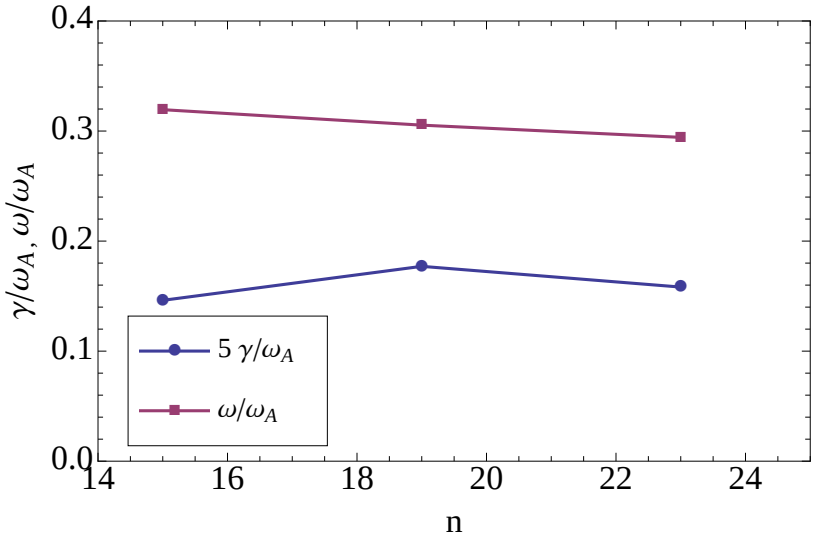

Figure 3.2: TAE growth rate and frequency for the hybrid equilibrium are plotted vs. toroidal mode number n with an alpha pressure $\beta_{\alpha 0} = 4\%$.

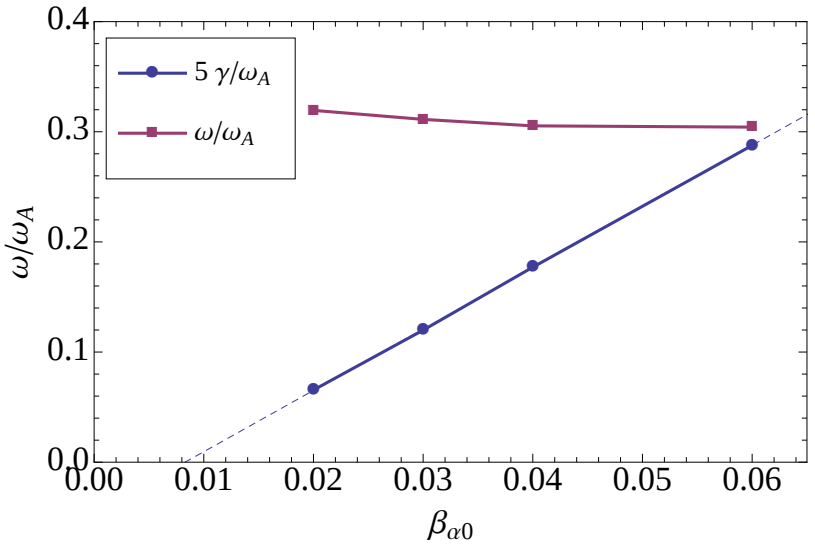

Figure 3.3: TAE growth rate and frequency for the hybrid equilibrium are plotted vs. the on-axis alpha pressure $\beta_{\alpha 0}$. A line of best fit for the growth rate which is drawn as the dashed line is projected to find the alpha pressure threshold.

The TAE mode structure for the different toroidal mode numbers scanned are shown in Figure 3.4, and the poloidal harmonics of the modes are shown in Figure 3.5. The mode structures are all broad with modest ballooning and include many poloidal m-harmonics. For the toroidal modes $n = 15$, $n = 19$, and $n = 23$, the strongest poloidal modes are $m = 21, 22,$

$m = 27, 28$, and $m = 32, 33$, respectively. Note that as the toroidal mode number increases, the radial width of the TAE decreases.

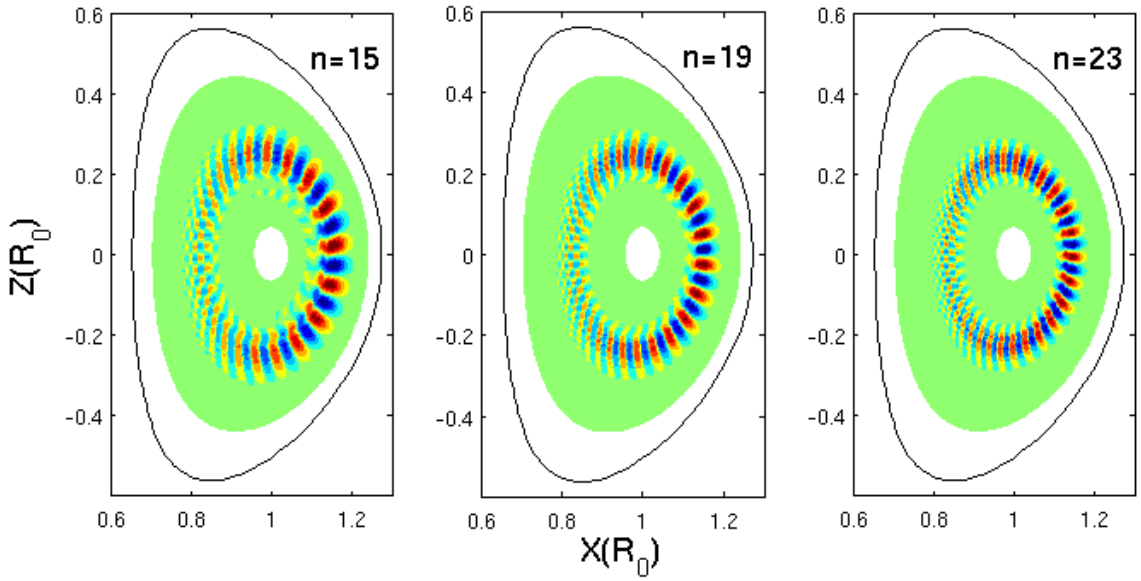

Figure 3.4: The electrostatic potential for toroidal mode numbers n=15,19,23 are plotted in the hybrid scenario. The last closed flux surface is shown by a solid black line, and white space represents outside of the simulation domain.

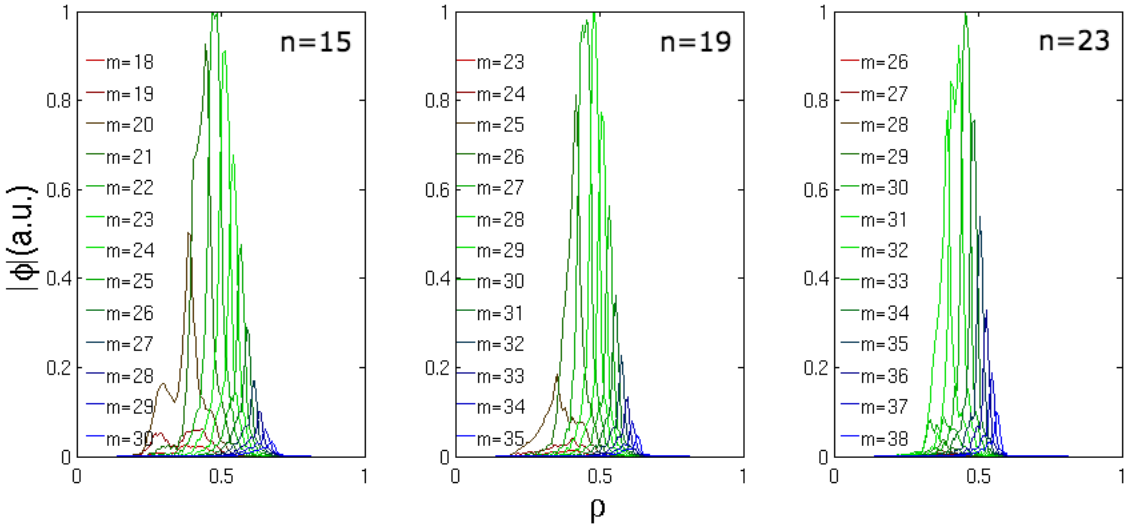

Figure 3.5: The poloidal harmonics m of the TAE in the hybrid equilibrium with toroidal mode numbers n=15,19,23 are plotted vs. the normalized square root of the toroidal flux ρ.

3.8 TAE for ITER steady state equilibrium

In this section, the same simulations as the previous section for a steady state scenario equilibrium are repeated. Different toroidal mode numbers are examined for this scenario in Figure 3.6 to determine what is the most unstable mode for an alpha pressure of $\beta_{\alpha 0} = 4\%$. The TAE frequency is $\omega = 0.032\,\omega_A$ for the $n = 15$ mode, and is $\omega = 0.034\,\omega_A$ for the $n = 17$ and $n = 19$ modes. Like the hybrid scenario, the growth rate of the $n = 19$ TAE mode has a slightly larger growth rate.

The on-axis alpha particle pressure for this equilibrium is $\beta_{\alpha 0} = 0.796\%$, and the $\beta_{\alpha 0}$ is adjusted to find the stability threshold. Figure 3.7 shows the steady state scenario $n = 19$ TAE frequency and growth rate for different values of the on-axis alpha pressure. When alpha pressure is adjusted, the TAE frequency is $\omega = 0.032\,\omega_A$ when $\beta_\alpha = 2\%$ and $\beta_\alpha = 3\%$. When $\beta_{\alpha 0}$ is increased to 4 %, the frequency raises to $\omega = 0.034\,\omega_A$. Using a line of best fit, the threshold required to excite the instability is approximately $\beta_{\alpha 0} = 0.7\%$.

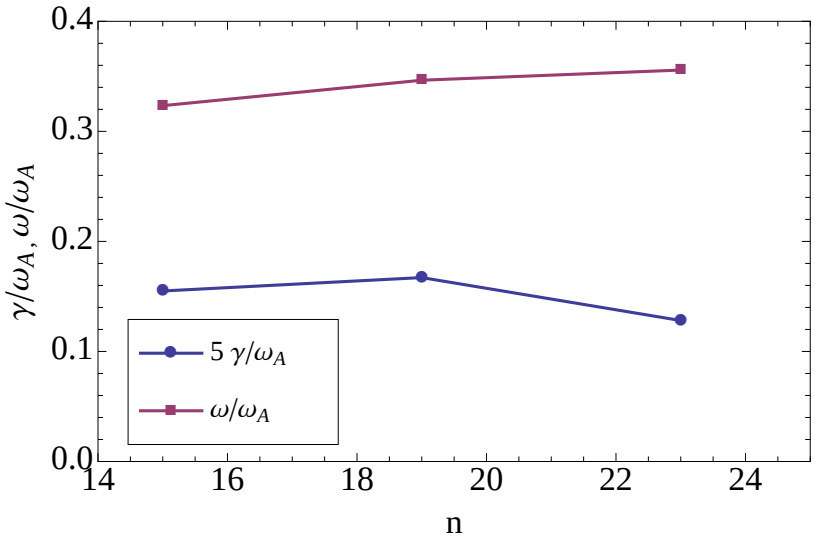

Figure 3.6: TAE growth rate and frequency for the steady state equilibrium are plotted vs. toroidal mode number with an alpha pressure $\beta_{\alpha 0} = 4\%$.

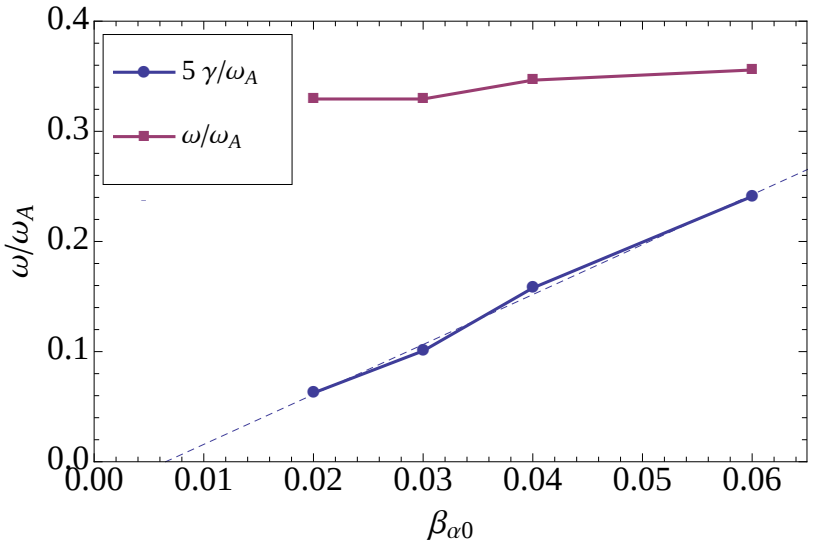

Figure 3.7: TAE growth rate and frequency for the steady state equilibrium are plotted vs. the on-axis alpha pressure $\beta_{\alpha 0}$. A line of best fit for the growth rate which is drawn as the dashed line is projected to find the alpha pressure threshold.

The steady state equilibrium TAE mode structure for the different toroidal mode numbers scanned are shown in Figure 3.8, and the poloidal harmonics of the modes are shown in Figure 3.9. The ballooning structure is stronger in the steady state scenario than it is in the hybrid scenario. The mode structure of the $n = 15$ and the $n = 19$ modes have dominant harmonics at the minimum of the q-profile. The $n = 23$ TAE mode structure is shifted radially outward from the q-profile minimum.

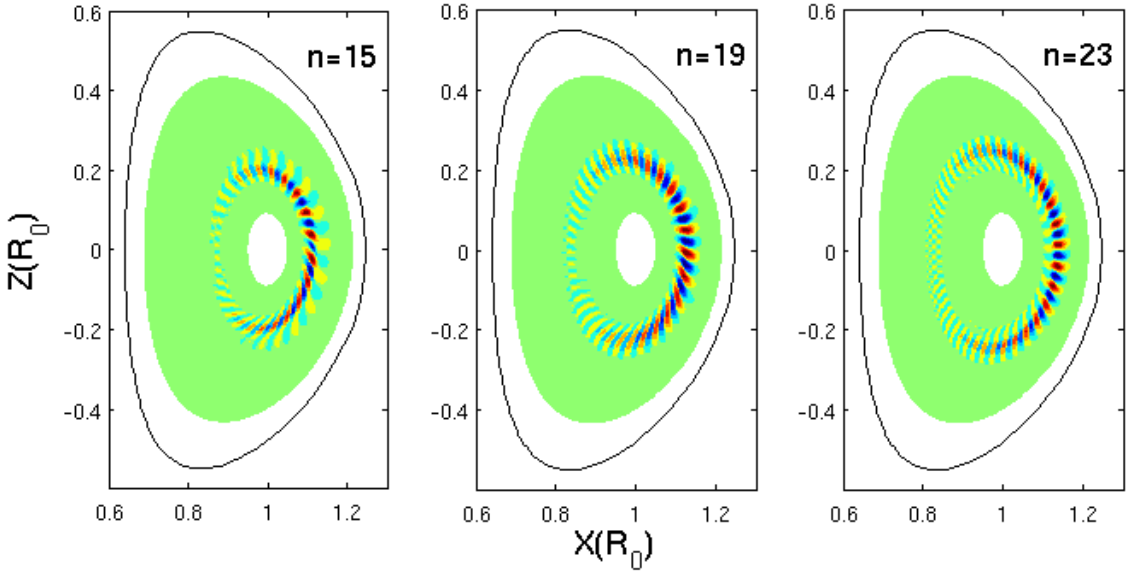

Figure 3.8: The electrostatic potential for toroidal mode numbers n=15,19,23 in the steady state scenario are plotted. The last closed flux surface is shown by a solid black line, and white space represents outside of the simulation domain.

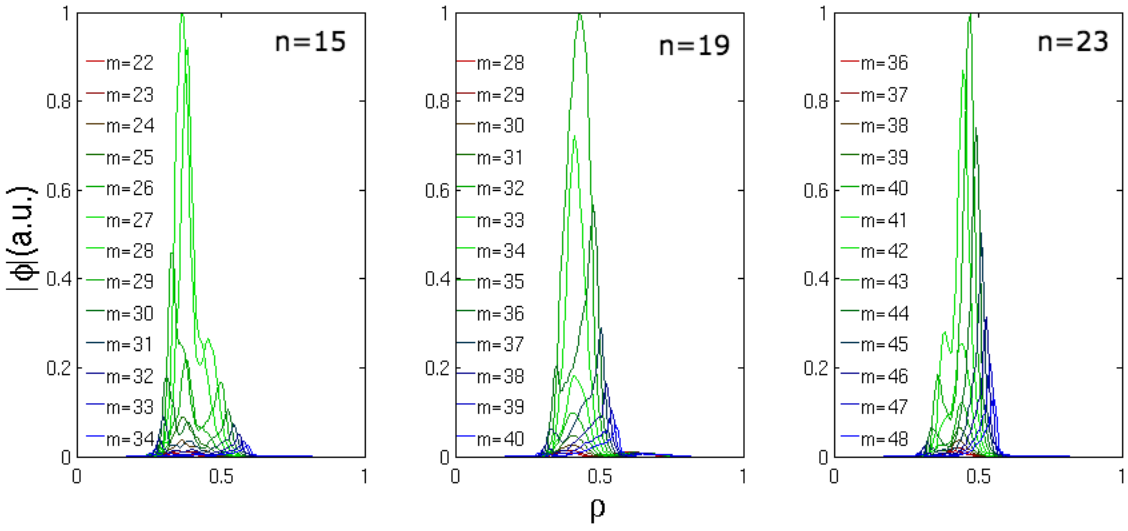

Figure 3.9: The poloidal harmonics m of the TAE in the steady state equilibrium with toroidal mode numbers n=15,19,23 are plotted vs. the normalized square root of the toroidal flux ρ. The minimum of the q-profile is located at 0.4 ρ.

3.9 Summary

In this chapter, stability thresholds of the toroidal Alfvén eigenmodes were examined for the hybrid and the steady state scenario in ITER. To perform these tests we first implemented a slowing down fast alpha distribution into GTC. The TAE in the hybrid scenario has a stability alpha pressure threshold of approximately $\beta_{\alpha 0} = 1.0\%$. In the steady state scenario, the TAE has a lower alpha pressure threshold of $\beta_{\alpha 0} = 0.7\%$. So the hybrid scenario is more stable than the steady state scenario. While it appears that both of thresholds are close to marginal stability for their respective equilibria, adding the ITER 1 MeV beam ions to the simulation should push the TAE from marginally unstable to unstable.

Chapter 4

Internal kink mode in tokamaks

The ideal MHD internal kink mode is an m=n=1 perturbation driven unstable by the equilibrium currents in a tokamak. Here m and n are the poloidal and toroidal mode number, respectively. The mode structure peaks at the rational surface with the safety factor q=1. Internal kink modes are thought to be the trigger for the sawtooth collapse, and interaction between the internal kink mode and fast ions can excite fishbone modes. Both sawtooth oscillations and fishbone modes are a potential threat to the α-particle confinement in the International Thermonuclear Experimental Reactor(ITER). The excitation of fishbone-like modes[41] by fast ions is routinely observed in current tokamak experiments. Recent experiments manipulate the current profile to destabilize the sawtooth oscillations to avoid the more dangerous neoclassical tearing modes[67]. When q is larger than unity but approaches unity, a long-lived kink mode has been observed to degrade the fast ion confinement[39, 40, 9].

The ideal MHD theory finds that the internal kink is always unstable in a cylindrical geometry with a q=1 surface[2]. In a toroidal geometry, the internal kink mode can be stabilized by the toroidicity[25] due to the coupling to the m=2 harmonic. However, the toroidicity can

be either stabilizing or destabilizing depending on the plasma beta β (defined as the ratio of kinetic pressure to magnetic pressure) [68]. The stabilization of internal kink modes by the toroidicity has been confirmed in some MHD simulations [69, 70]. Recent nonlinear two-fluid simulations with sources and sinks was able to demonstrate the long time dynamics of kink modes exhibiting sustained cycles[71].

Kinetic effects can play an important role on the stability of the internal kink mode due to the thin layer of perturbed currents near the mode rational surface[2]. The kinetic effects tend to stabilize the internal kink mode[72, 73] in general. However, sufficient fast ion pressure gradients can destabilize internal kink modes[37] or even excite fishbone modes[38]. To study the kinetic effects, gyrokinetic particle simulation has been utilized to simulate internal kink modes in the cylindrical geometry[20, 74]. The growth rate and mode structure are found[21] to depend strongly on the ratio of ion gyroradius to radial width of the perturbed current layer near the rational surface. In the toroidal geometry, a gyrokinetic eigenvalue analysis[75] shows that trapped ions can significantly affect the internal kink eigenmode structure and growth rate.

4.1 Equilibrium model for kink simulations

While GTC has the capability to simulate realistic tokamak equilibria[76, 18], this chapter will focus on using analytical equilibria to simulate kink modes for both cylindrical geometry and toroidal geometry. In cylindrical geometry, the toroidal angle is defined as $\zeta = 2\pi z/L$, where z is the axial position and L is the length of the cylinder. The effective major radius

in cylindrical geometry is $R_0 = L/2\pi$, and a periodic boundary condition is used for the toroidal angle. The cylindrical geometry equilibrium is:

$$\begin{aligned} B_0 &= B_a, \\ I &= B_a r^2/q, \\ g &= B_a R_0^2, \\ \theta &= \theta_0, \\ \zeta &= \zeta_0, \end{aligned} \tag{4.1}$$

where B_a is the on axis magnetic field strength. The variables θ_0 and ζ_0 represent the geometric poloidal and toroidal angles, and q is the safety factor.

For toroidal simulations, a tokamak with concentric flux-surfaces will be used at two levels of approximation[77]. At the lowest order in the expansion of the toroidal geometry, using the inverse aspect ratio as a smallness parameter, we approximate the magnetic flux θ-coordinate as the geometric angle θ_0,

$$\begin{aligned} B_0 &= B_a - B_a \epsilon \cos\theta_0 + \mathcal{O}(\epsilon^2), \\ I &= B_a r^2/q + \mathcal{O}(\epsilon^4), \\ g &= B_a R_0^2 + \mathcal{O}(\epsilon^2), \\ \theta &= \theta_0, \\ \zeta &= \zeta_0, \end{aligned} \tag{4.2}$$

where ϵ is the local inverse aspect ratio r/R_0. The next order is a realistic toroidal geometry equilibrium[56], which uses a more realistic magnetic flux θ-coordinate,

$$\begin{aligned} B_0 &= B_a - B_a\epsilon\cos\theta_0 + \mathcal{O}(\epsilon^2), \\ I &= B_a r^2/q + \mathcal{O}(\epsilon^4), \\ g &= B_a R_0^2 + \mathcal{O}(\epsilon^2), \\ \theta &= \theta_0 - \epsilon\sin\theta_0, \\ \zeta &= \zeta_0. \end{aligned} \tag{4.3}$$

Note that a poloidal current term g of order ϵ^2 was ignored while the toroidal current term I of same order is kept. This is because poloidal current term is an order of ϵ smaller than the toroidal current in the equilibrium current density $\nabla \times \mathbf{B}_0$ because $|\nabla\zeta/\nabla\theta| \sim \epsilon$.

For implementation of the realistic toroidal geometry equilibrium, the Cartesian coordinates $X(\psi,\theta)$ and $Z(\psi,\theta)$ are approximated for construction of a 2D spline. This is done so that each term in the X and Z are separable into a function of ψ and θ, and the 2D splines can be constructed from a 1D spline in ψ and a 1D spline in θ.

$$\begin{aligned} X &= 1 - \epsilon\cos\theta_0 \approx 1 - \epsilon\cos(\theta + \epsilon\sin\theta) \\ &\approx 1 - \epsilon\cos\theta + \epsilon^2\sin^2\theta - 1/2\epsilon^3\sin^2\theta\cos\theta \\ Z &= \epsilon\sin\theta_0 \approx \epsilon\sin(\theta - \epsilon\sin\theta) \\ &\approx \epsilon\cos\theta + \epsilon^2\sin\theta\cos\theta - 1/2\epsilon^3\sin^2\theta \end{aligned} \tag{4.4}$$

Note that higher order ϵ terms are kept for the 2D spline functions $X(\psi,\theta)$ and $Z(\psi,\theta)$ to preserve the circular cross-section of the tokamak, and is discussed in more detail in Appendix D

4.1.1 Extending the simulation region to the magnetic axis

In this subsection, a method to extrapolate solutions to the magnetic axis for the gyrokinetic Poisson equation and Ampere's Law is discussed. The simulation domain must include the magnetic axis, since the $m = n = 1$ internal kink mode structures have a finite value near the axis which will be shown in subsequent sections. This suggests that the internal kink mode could be unphysically damped by excluding the magnetic axis in the simulation. GTC uses the finite difference method to calculate the two dimensional perpendicular Laplacian on a poloidal plane away from the magnetic axis. The Laplacian operator in GTC is written in magnetic flux coordinates, as shown below[76].

$$\begin{aligned}\nabla_\perp^2 F =& g^{\psi\psi}\frac{\partial^2 F}{\partial\psi^2} + 2g^{\psi\theta}\frac{\partial^2 F}{\partial\psi\partial\theta} + \left(g^{\theta\theta} + g^{\zeta\zeta}/q^2\right)\frac{\partial^2 F}{\partial\theta_0^2} + \\ & \frac{1}{\mathcal{J}}\left(\frac{\partial \mathcal{J} g^{\psi\psi}}{\partial\psi} + \frac{\partial \mathcal{J} g^{\psi\theta}}{\partial\theta}\right)\frac{\partial F}{\partial\psi} + \\ & \frac{1}{\mathcal{J}}\left(\frac{\partial \mathcal{J} g^{\psi\theta}}{\partial\psi} + \frac{\partial \mathcal{J} g^{\psi\psi}}{\partial\theta}\right)\frac{\partial F}{\partial\theta}\end{aligned} \tag{4.5}$$

In the above equation, the contravariant tensor is defined as $g^{\alpha\beta} \approx \nabla\alpha \cdot \nabla\beta$, where α and β are any combination of the magnetic coordinates ψ, θ, or ζ. The choice of the magnetic flux coordinate system leads to numerical errors when inverting the Laplacian operator near the axis for low-m modes. To understand why the numerical errors arise, consider Laplace's equation in cylindrical coordinates, which has the Bessel functions J_m as a solution. With r being defined as the minor radius, Bessel functions behave as $J_m \propto r^m$ near the axis, and

the equilibrium poloidal flux behaves as $\psi \propto r^2$ near the magnetic axis. Since quantities like $\partial r/\partial\psi$ and $\partial^2 r/\partial\psi^2$ are singular near the magnetic axis, the Laplacian of a $m = 0, 1$ Bessel function will lead to numerical errors in differencing the ψ derivatives.

To avoid numerical errors near the magnetic axis, the Laplacian is solved using finite differences for the majority of the simulation domain, then $\delta\phi$ and $\delta A_{||}$ are extrapolated to the magnetic axis for the first few flux surfaces. The flux surface that separates the finite differences region and the extrapolation region will be referred to as the "FD Boundary" for short. The perpendicular Laplacian of a Bessel function returns the same Bessel function multiplied by a constant with $\nabla_\perp^2 J_m(\eta r)\cos(m\theta) = -\eta^2 J_m(\eta r)\cos(m\theta)$, where η is the numerical constant. This relationship can be used to extrapolate the behavior of $\delta\phi$ and $\delta A_{||}$ near the magnetic axis. The method described here retains only the $m = 0, 1$ modes near the axis. To extrapolate solutions to the magnetic axis, perturbed quantities such as $\delta\phi$ and $\delta A_{||}$ can be Fourier decomposed at the FD Boundary surface. Since the $m = 0$ Bessel function is approximately constant, and the $m = 1$ Bessel function is approximately linear in r, the Laplacian of a function near the magnetic axis can be extrapolated with the form of the equation below,

$$\nabla_\perp^2 F = a_0 + a_1 \frac{r}{r_b}\cos\theta + b_1 \frac{r}{r_b}\sin\theta. \tag{4.6}$$

The quantities a_0, a_1, and b_1, are the poloidal Fourier coefficients of the perturbed quantities at the FD Boundary flux surface. The radial location of the FD Boundary is given by r_b, where the subscript b represents the radial FD boundary grid point. To complete the

finite differences Laplacian matrix, a linear boundary condition in r is chosen between the extrapolation region and the finite difference region.

$$F_{b-1} = 2F_b - F_{b+1} \tag{4.7}$$

To test this Laplacian operator, with the variable "a" being defined as the minor radius of the wall, the function $F = re^{-50(r/a)^8}$, was chosen because it is linear in r near the magnetic axis. A perpendicular Laplacian is applied analytically on F to obtain $G = \nabla_\perp^2 F$. The function G is input into GTC, which solves the gyrokinetic Poisson equation for F. The numerical solution to the perpendicular Laplacian and the analytical function F can be seen in Figure 4.1. For this test case the first eight radial grid points were chosen to be in the extrapolation region, and the rest in the finite differences region. The GTC solution and the analytic function F agree well in both regions with no significant error near the FD boundary.

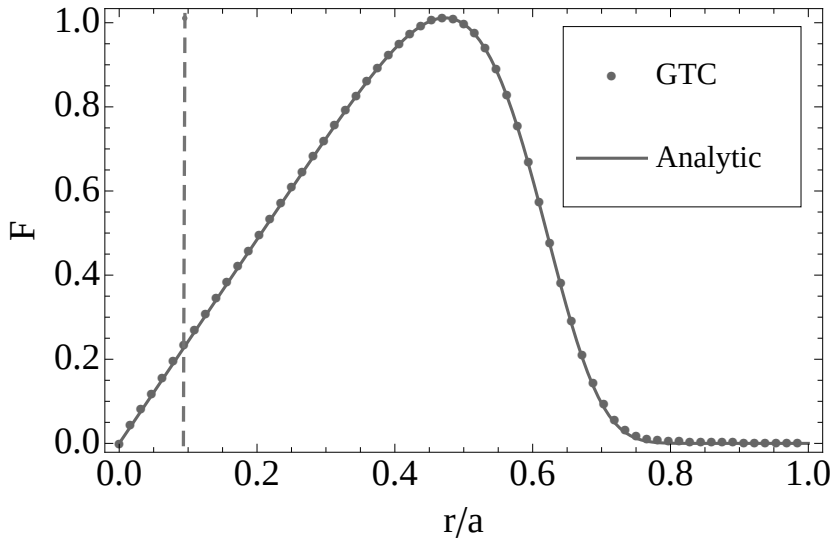

Figure 4.1: The GTC laplacian operator solution and the analytic solution for F are plotted against radial coordinate, r/a. The FD boundary flux surface is drawn with a vertical dashed line.

To treat the ion dynamics near the magnetic axis, if a particle is located within the flux surface of the first radial grid, the position is updated using Cartesian-like coordinates,

$$\begin{aligned} x &= \sqrt{\psi}\cos\theta, \\ z &= \sqrt{\psi}\sin\theta. \end{aligned} \tag{4.8}$$

The ion position is updated using the following equations,

$$\begin{aligned} x_1 &= x_0 + \Delta t\left(\frac{\partial x}{\partial \psi}\dot{\psi} + \frac{\partial x}{\partial \theta}\dot{\theta}\right), \\ z_1 &= z_0 + \Delta t\left(\frac{\partial z}{\partial \psi}\dot{\psi} + \frac{\partial z}{\partial \theta}\dot{\theta}\right). \end{aligned} \tag{4.9}$$

The subscripts 0 and 1 represent the old and new position, respectively. The term Δt is the time step size, $\dot{\theta}$ and $\dot{\psi}$ are the time derivatives of the particle position in magnetic coordinates, which are described in detail in Holod et al[55]. To return to magnetic coordinates, Equations 4.8 are inverted:

$$\begin{aligned} \psi &= x^2 + z^2, \\ \theta &= z/|z|\arccos\left[x/(x^2+z^2)\right], \end{aligned} \tag{4.10}$$

where $|z|$ is the magnitude of z.

4.2 GTC simulation of kink instability in cylindrical geometry

The first internal kink mode simulations are in cylindrical geometry in order to verify the gyrokinetic capability of simulating kink modes and to benchmark the GTC results against ideal MHD theory without added complexity of toroidicity. The MHD eigenvalue code used to benchmark the GTC internal kink simulation is based on the 1D solution to the MHD equations in the cylindrical geometry and contains all ideal MHD effects[78]. This eigenmode code is described in detail in Appendix A. The GTC fluid limit model contains only the reduced MHD physics making approximations such as $k_{||}/k_{\perp} \ll 1$, and $\delta B_{||} = 0$.

The Alfvén frequency is used to normalize the internal kink growth rate and is defined as $\omega_A = v_A/R_0$. In this simulation, a uniform pressure is used with the ion gyroradius of $\rho_i/R_0 \approx 0.001$ and an electron beta of $\beta_e = 8\pi n_{0e}T_e/B^2 = 0.4\%$. In the MHD eigenvalue code, the finite beta effect that gives rise to compressibility is found to be negligible. The safety factor is

$$q(r) = \frac{4}{5}\left(1 + \frac{r^2}{a^2}\right), \tag{4.11}$$

where a is the minor radius of the device.

4.2.1 GTC simulations in fluid limit

For the GTC fluid simulations, the linearized Equations 2.2-2.7 are used with ion kinetic effects suppressed and with the parallel electric field set to zero(i.e. $\delta\phi_{eff} = 0$). Since the effective scalar potential is set to zero and there is no equilibrium pressure gradient, β_e cancels out and does not have any effect on the system of fluid equations.

Applying an initial perturbation to $\delta A_{||}$, the simulation is ran long enough to observe exponential growth and converged mode structures. Figure 4.2 shows the growth rate of the internal kink mode for three different inverse aspect ratios. As the inverse aspect ratio increases, the growth rate of the internal kink mode increases for both GTC and MHD eigenvalue codes. For all three aspect ratios, the GTC growth rate agrees with the MHD growth rate to within 15%. This increase in growth rate for larger inverse aspect ratio can be seen in Rosenbluth et al.[2], where it was shown that the internal kink growth rate is of the order $\gamma \sim r^2/R_0^2\,\omega_A$. The frequency from the GTC simulation is zero, which is consistent with the ideal MHD theory.

With radial location of the $q = 1$ mode rational surface defined as r_s, the $r_s/R_0 = 0.25$ case will be examined more closely, since it has the largest growth rate and a broad mode width at the mode rational surface. While all m-modes are kept, the $m = 1$ mode is the dominant mode in these simulations. The GTC $m = 1$ mode structures of $\delta A_{\|}$, $\delta u_{e\|}$, and $\delta\phi$, along with their ideal MHD counterparts are shown in Figure 4.3 and 4.4. Overall, the agreement between GTC and ideal MHD mode structures is good, however, the GTC mode structures are slightly sharper at the $q = 1$ surface than the MHD mode structures. In Figure 4.3, the perturbed current $\delta J_{||}$ has a thin layer that is peaked at the $q = 1$ surface. Defining Δr_{kink} as the half width of this current layer, the current layer width is $\Delta r_{kink}/a \approx 0.061$. It is the size of this current layer that the ion gyroradius and other relevant scale lengths will be compared to in the following sections.

The small differences in growth rates and mode structure between GTC and MHD eigenvalue codes can likely be attributed to the difference between the two models such as the assumption of $k_{||}/k_{\perp} \ll 1$, and $\delta B_{||} = 0$ in GTC.

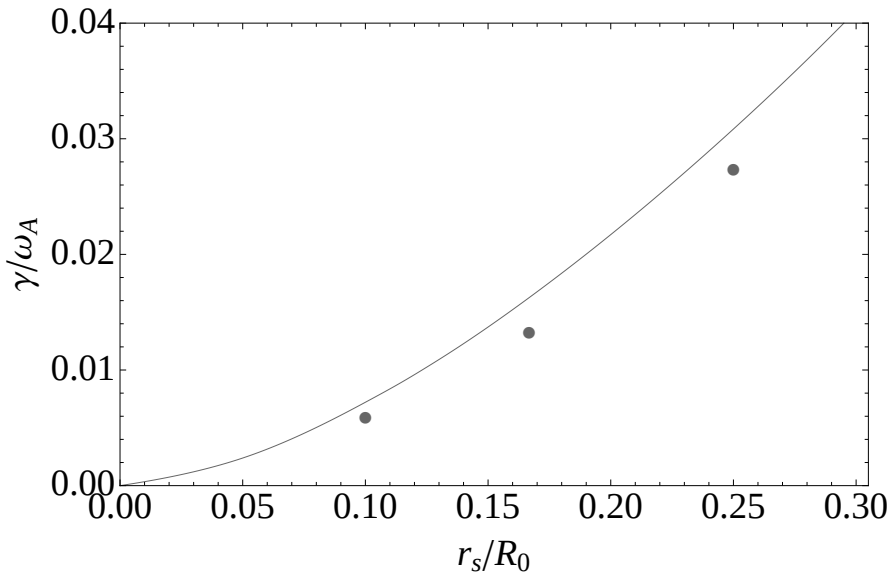

Figure 4.2: The internal kink mode growth rate is plotted vs. the inverse aspect ratio r_s/R_0 of the $q = 1$ surface for cylindrical geometry.

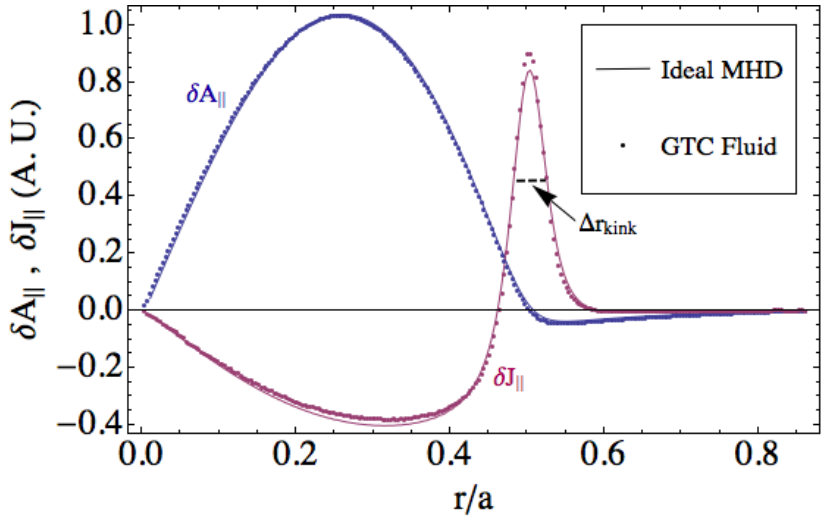

Figure 4.3: The mode structure of $\delta A_{||}$ and $\delta J_{||}$ are plotted against the radial coordinate r/a, for the $r_s/R_0 = 0.25$ case in cylindrical geometry.

4.2.2 GTC gyrokinetic simulations

For studying kinetic effects on the internal kink mode for the $r_s/R_0 = 0.25$ case, the same parameters as the fluid simulation are used, where $\beta_e = \beta_i = 0.4\%$. For the gyrokinetic simulations, the linearized Equations 2.2-2.12 are used. In this simulation, the

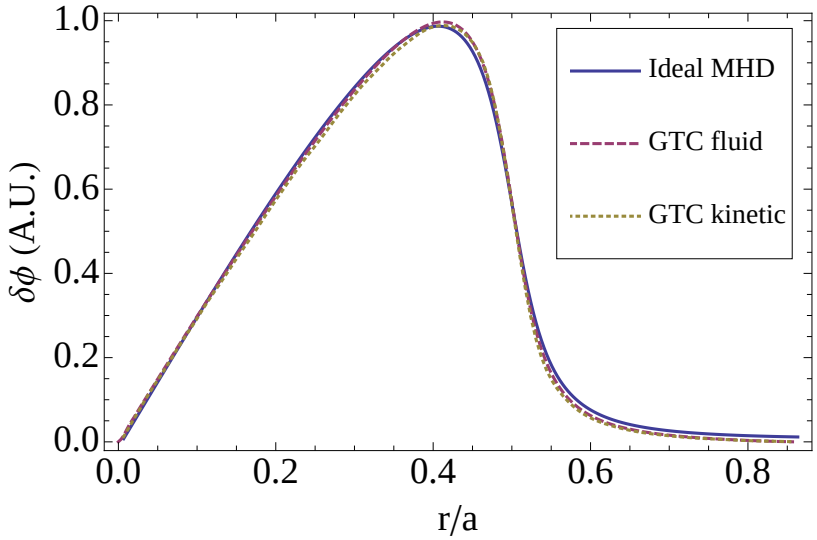

Figure 4.4: The mode structure of the electrostatic potential $\delta\phi$ vs. the radial coordinate r/a is plotted for the $r_s/R_0 = 0.25$ case in cylindrical geometry.

ion Larmor radius is much smaller than the minor radius and the perturbed current layer with $\rho_i/a \approx 0.002$ and $\rho_i/\Delta r_{kink} \approx 0.033$. Since the ion gyroradius scale length is much smaller than relevant mode scale lengths, kinetic effects should play only a small role and the result should be similar to the fluid simulation.

The internal kink mode growth rate from the kinetic simulation is $\gamma = 0.026\,\omega_A$, about 10% smaller than the fluid simulation. Figure 4.4 shows the internal kink mode electrostatic potential from GTC gyrokinetic, GTC fluid and MHD simulations. The electrostatic potential in the gyrokinetic simulation is almost identical to the GTC fluid simulation. In the regime where the Larmor radius is much smaller than the perturbed current layer, the kinetic effects are not significant as expected. This result agrees with Mishchenko et al.[21], which showed that the ion kinetic effects are not important when the ratio of the ion gyroradius to the MHD current layer $\rho_i/\Delta r_{kink}$ is approximately twice the value used in our simulation.

4.2.3 Convergence tests

In this subsection, two convergence tests that were performed for GTC fluid simulation of the $r_s/R_0 = 0.25$ case are shown in Figure 4.5. The first convergence test is to ensure that the FD boundary does not cause any numerical problems. Figure 4.5(a) shows the internal kink mode growth rate for different values of radial FD boundary point. The growth rate remains almost constant for different r_b, suggesting that the FD radial boundary location has little effect on the growth rate as long as the boundary is far away from the mode $q = 1$ surface. For the rest of the simulations in this chapter, a FD boundary point of $r_b = 0.04\,a$ is chosen where the $q = 1$ surface is at $r = 0.5\,a$.

The other convergence test is a radial grid point convergence shown in Figure 4.5(b). Since internal kink modes can have a thin current layer at the $q = 1$ surface, it is important to make sure that the thin layer is adequately resolved. The growth rate is approximately converged when there are 128 radial grid points, which corresponds to approximately 7 grid points within the current layer half width Δr_{kink}. For the $r_s/R_0 = 0.1$ simulation in Figure 4.2, the current layer at the mode rational surface Δr_{kink} is very thin. A radially nonuniform grid have also been successfully used so there can be higher resolution near the $q = 1$ surface, and lower resolution away from it.

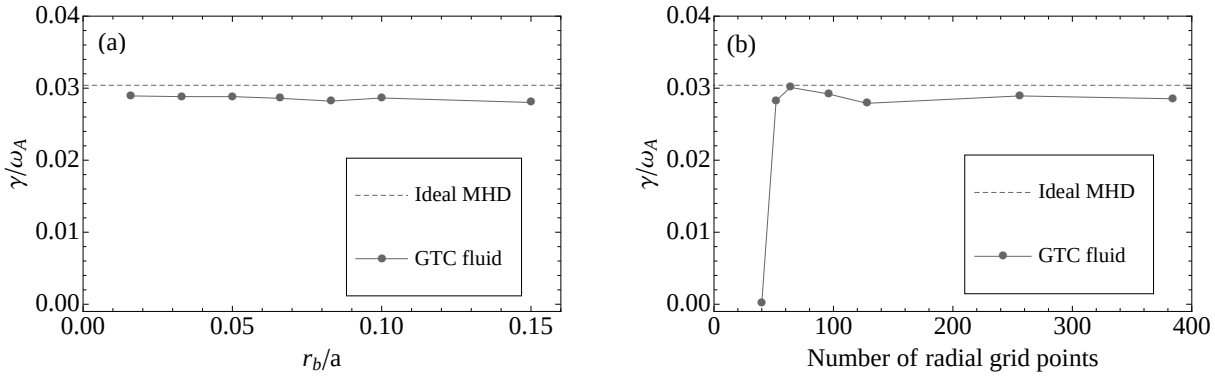

Figure 4.5: Panel(a): The growth rate of the internal kink mode is plotted vs. radial position of the FD boundary $r_s/R_0 = 0.25$ case. Panel(b): The GTC internal kink mode growth rate is plotted against the number of radial grid points for the $r_s/R_0 = 0.25$ case.

The internal kink mode growth rate is well converged for 32 grid points in the ζ direction and 300 grid points in the θ-direction at the $q = 1$ surface. In GTC gyrokinetic simulations of high-n microturbulence, the number of poloidal grid points is determined such that the arc length between grid points is approximately constant on all flux surfaces. This means there are less poloidal grid points near the axis, which is why 300 poloidal grid points at the $q = 1$ surface were needed. For simulations of the low-n modes, it is computationally more efficient to use a uniform grid in the θ-direction, which will be used in the future. For gyrokinetic simulations, ten particles per cell are adequate for convergence.

4.3 GTC simulations of kink instability in toroidal geometry

Using the analytic toroidal equilibria shown in Equation 4.2 and Equation 4.3, GTC simulations are performed with the same parameters as the cylindrical simulation to study the effects of toroidicity on internal kink modes with $r_s/R_0 = 0.25$.

4.3.1 GTC simulations in fluid limit

When the lowest-order tokamak model shown in Equation 4.2 is used, the properties of the internal kink mode are very similar to the cylindrical geometry. The growth rate is $\gamma = 0.026\,\omega_A$, which is approximately the same as the cylindrical geometry growth rate of $\gamma = 0.028\,\omega_A$. Figure 4.6 shows the electrostatic potential of internal kink mode for the two toroidal geometry models. The kink mode structure for the lowest-order toroidal model(Equation 4.2) is approximately the same as the cylindrical geometry model, and little coupling to higher m harmonics is observed.

When the realistic toroidal model shown in Equation 4.3 is used, the growth rate is $\gamma = 0.0255\,\omega_A$, which is approximately the same as the lowest order tokamak model of Equation 4.3. Figure 4.6(b) shows that for the realistic toroidal model, the internal kink mode is bent so that the mode is larger on the low field side. This bending is along the magnetic flux coordinate θ such that the internal kink mode is still almost purely an $m = 1$ mode in the flux coordinate system, with little m-mode coupling. Since the only physical difference between the lowest-order tokamak model and the realistic tokamak model is magnetic field configuration that gives rise to a different Jacobian, the change to the mode structure must be solely due to the more realistic magnetic field configuration. The growth rates for both toroidal models are approximately the same as the cylindrical geometry model, and only small stabilization due to m-mode coupling as predicted by Bussac et al[25]. However, we note that Galvao et al. predicted that the kink mode becomes more unstable for a lower aspect ratio case[68].

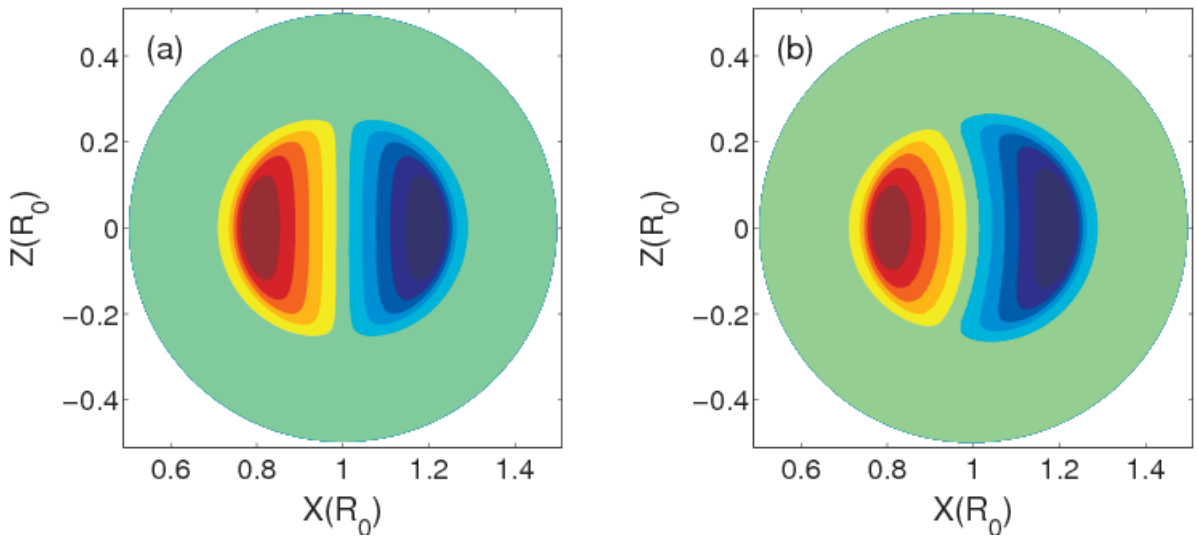

Figure 4.6: The $\delta\phi$ mode structure is plotted in the poloidal plane. The lowest-order tokamak mode structure is plotted in panel(a), and realistic tokamak model mode structure is plotted in in panel(b)

4.3.2 GTC gyrokinetic simulations

Using the linearized gyrokinetic Equations 2.2-2.12, the realistic toroidal geometry model shown in Equation 4.3 is simulated in this section with kinetic effects. The ion banana orbit width for this simulation is approximately $\Delta r_{banana} = 2q(R_0/r)^{1/2}\rho_i = 4\rho_i$. Then the ratio of the ion banana orbit width to the kink current layer width is $\Delta r_{banana}/\Delta r_{kink} \approx 0.12$, so kinetic effects due to the finite orbit width should still be minimal when $\beta_i = 0.4\%$. However, when ion kinetic effects are added to the toroidal geometry simulation, the internal kink mode growth rate decreases significantly to $\gamma = 0.0085\,\omega_A$ compared to the GTC fluid simulation of $\gamma = 0.0255\,\omega_A$ in the same geometry as discussed in subsection 4.1.

To understand the gyrokinetic result, several simulation scans were performed, which are shown in Figure 4.7. In the first scan, the ion pressure is varied while $\beta_i = \beta_e$ and the parallel electric field $\delta E_{||}$ is kept. The growth rate of the internal kink mode increases as the β_i is reduced, where at very low plasma pressure does the gyrokinetic growth rate reach the fluid growth rate. In the second scan, the β_i is varied while $\beta_i = \beta_e$ and setting $\delta E_{||} = 0$. The variations of the growth rate are approximately the same as the scan with finite parallel electric field $\delta E_{||}$. As a third scan, the ion temperature is varied while the electron temperature remains constant with $\beta_e = 0.4\%$, and $\delta E_{||} = 0$. The mode growth rates change is about the same as the previous two scans.

As a further check to see if this reduction of the growth rate is physical, Figure 4.8 shows a test excluding ion kinetic effects near the magnetic axis, while retaining kinetic effects in the rest of the simulation domain. In this test, if a particle crosses the boundary between the kinetic region and the region where thermal ion motion is suppressed, it will be reflected back into the kinetic region. When kinetic effects are removed near the $q = 1$ surface, the internal kink mode growth rate jumps from the gyrokinetic growth rate to the fluid growth

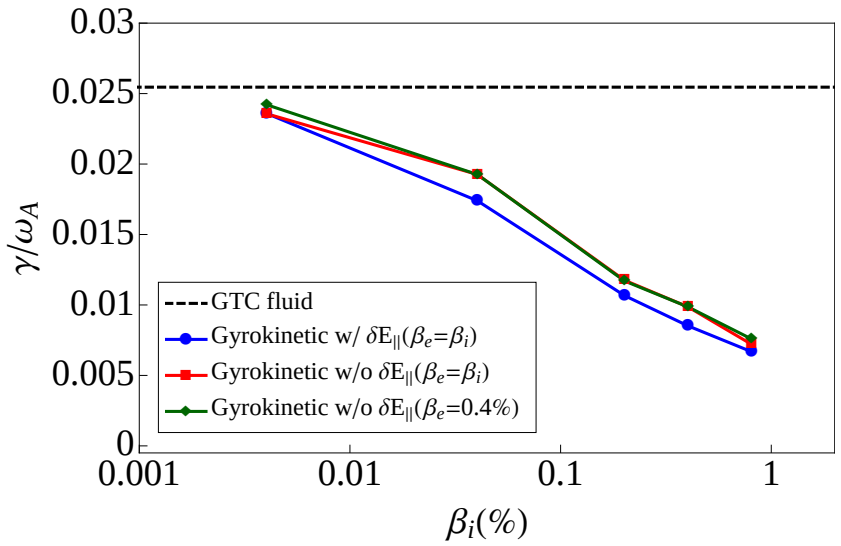

Figure 4.7: The growth rate vs. the ion beta β_i.

rate. The kinetic effect that reduces the growth rate is located near the resonant surface, which verifies that this effect is physical.

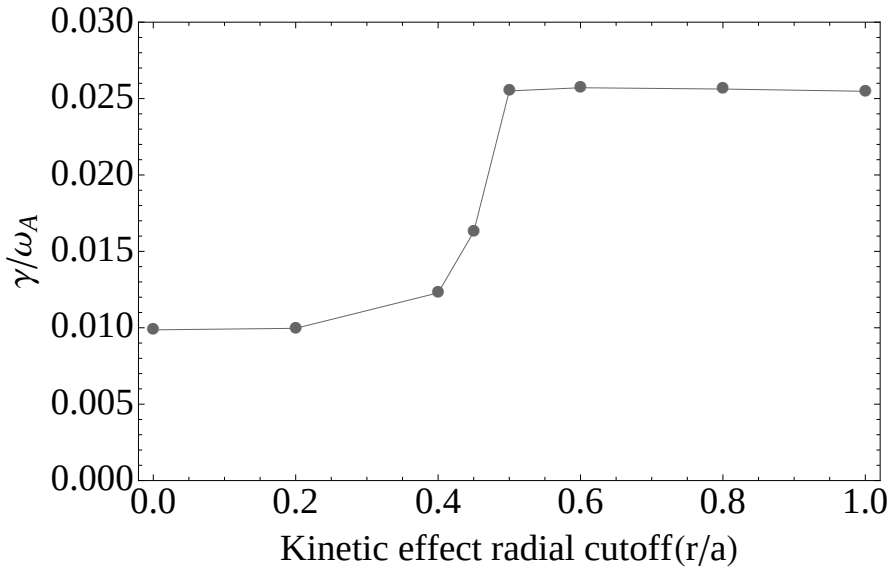

Figure 4.8: Internal kink mode growth rate is plotted against the kinetic effects radial cutoff, where kinetic effects are kept only outside the radial cutoff position. Inside the radial cutoff domain, the ion thermal motion is suppressed. Outside of the radial cutoff domain, all kinetic effects are kept.

The fact that the growth rate of the internal kink mode with the parallel electric field turned on and off are about the same suggests that the parallel electric field plays little

role. The reduction of the growth rate in kinetic simulations is due to ion kinetic effects, even though the banana orbit is much smaller than the MHD current layer. The ion kinetic effects that could cause this stabilization include trapped ions, wave-particle interactions, and polarization drift. The most likely candidate for this reduction of growth rate is due to the physics of the trapped ions interacting with the kink. Note that while the gyrokinetic eigenvalue calculation by Qin et al.[75] was in a regime where the ratio of the banana orbit width to fluid current layer $\Delta r_{banana}/\Delta r_{kink}$ is much larger than our simulation, they also observed that the trapped ions can significantly affect the internal kink growth rate. While this chapter has focused on uniform pressure profiles, in simulations with a finite pressure gradient, the pressure gradient can destabilize the internal kink mode.

4.4 GTC simulations of kink instability in DIII-D

In this section, the kink mode is simulated for a realistic geometry for the DIII-D tokamak shot #150363, at a time of 3110 ms. The simulation in this section was performed in the fluid limit. For this equilibrium as shown in panel(a) of Figure 4.9, the on axis safety factor is $q_a = 0.9$, and has a mode rational $q = 1$ surface at the $r = .34\,a$. Density and temperature profiles are typical to what are observed in DIII-D. The on-axis values are shown in Table 4.1, where B_{0a} is the magnetic field, R_{0a} is the major radius, n_{0ea} is the electron density, and T_{0ea} is the electron temperature.

DIII-D equilibrium	
B_{0a}	1.99 T
R_{0a}	1.7 m
n_{0ea}	0.56×10^{20} m^{-3}
T_{0ea}	2470 eV

Table 4.1: On-axis values for DIII-D equilibrium internal kink mode simulation

To have an appropriate pressure drive for this simulation, the thermal ion and fast ion pressures are added to the electron pressure, as shown below:

$$T_{e,sim} = (n_e T_e + n_i T_i + n_f T_f)/n_e, \tag{4.12}$$

where $T_{e,sim}$ is the electron temperature for this simulation. The total pressure is plotted in panel(b) of Figure 4.9

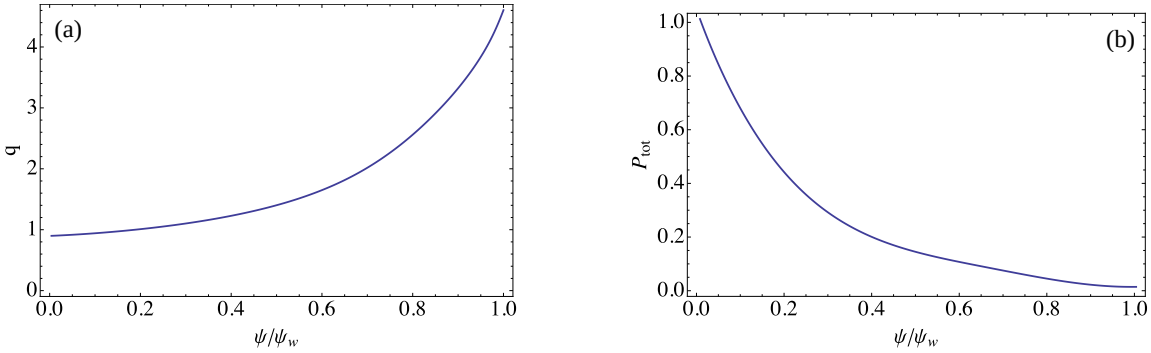

Figure 4.9: Panel(a): The safety factor q is plotted vs. the normalized poloidal flux. Panel(b): The total pressure P_{0tot} is plotted vs. the normalized poloidal flux.

The growth rate for this simulation is $\gamma = 0.015\,\omega_A$. This growth rate is in a similar range to that was observed for the analytical geometry simulations. The poloidal harmonics of the electrostatic potential for this case is plotted in Figure 4.10. Note that there is mode coupling

between the $m = 1$ and the $m = 2$ harmonics unlike the analytical equilibrium. This increase in mode coupling is most likely due to the the finite pressure gradient for the DIII-D geometry. A more recent simulation for this geometry was performed using gyrokinetic thermal and fast ions, where a fishbone mode excited by the fast ions is observed.

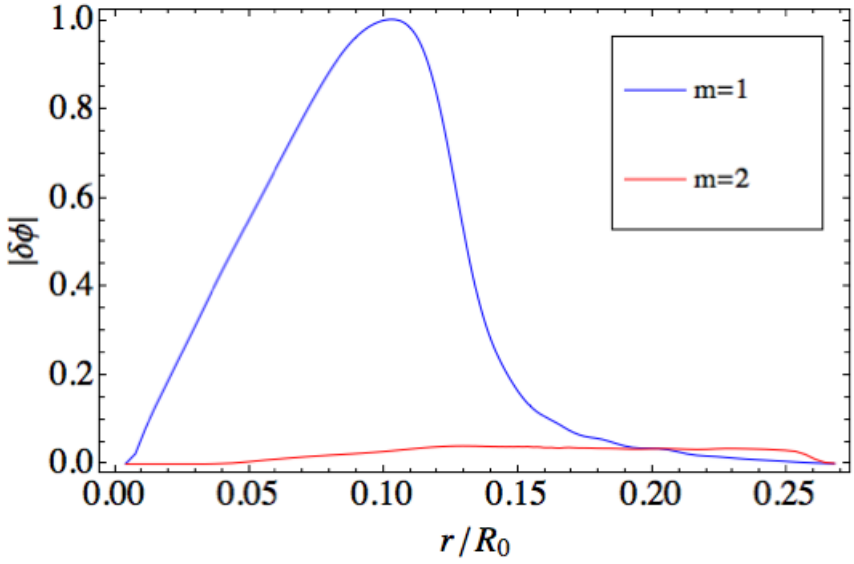

Figure 4.10: The poloidal cross section of $\delta\phi$ mode structure is plotted for the DIII-D equilibrium.

4.5 Finite difference vs. finite element operator

While the finite difference operator using the extrapolation method was found to be numerically robust in kink simulations, a Laplacian operator with any type of boundary condition near the axis is desired. To achieve this, the perpendicular Laplacian for gyrokinetic Poisson equation and Ampere's Law is also calculated using a finite element method.

The finite element method has many advantages compared to the finite difference method. In general, finite element method is considered to be more accurate than finite difference method. The finite element method is especially useful for simulations that want to incorporate the magnetic axis or separatrix into the simulation domain as its formulation is

based on Cartesian coordinates, and does not rely on the complex magnetic flux coordinates which break down at the magnetic axis and separatrix. Another advantage of finite element method is that it does not require ghost coordinates that could lead to error like the current formulation of the finite difference method in GTC. A more detailed discussion of the implementation of the finite element solver is given in Appendix B.

In finite differences method simulation, the internal kink mode growth rate is $\gamma = 0.028\,\omega_A$, while the finite element method simulation gives a growth rate of $\gamma = 0.027\,\omega_A$. The two growth rates are approximately the same. The electrostatic potential of the internal kink mode is plotted in Figure 4.11 for both the finite difference method and the finite element method. The mode structures of the electrostatic potentials between the two models agree very well. Note that the slight tilt of the mode structure in these plots is the phase of the internal kink mode due to choice of initial perturbation.

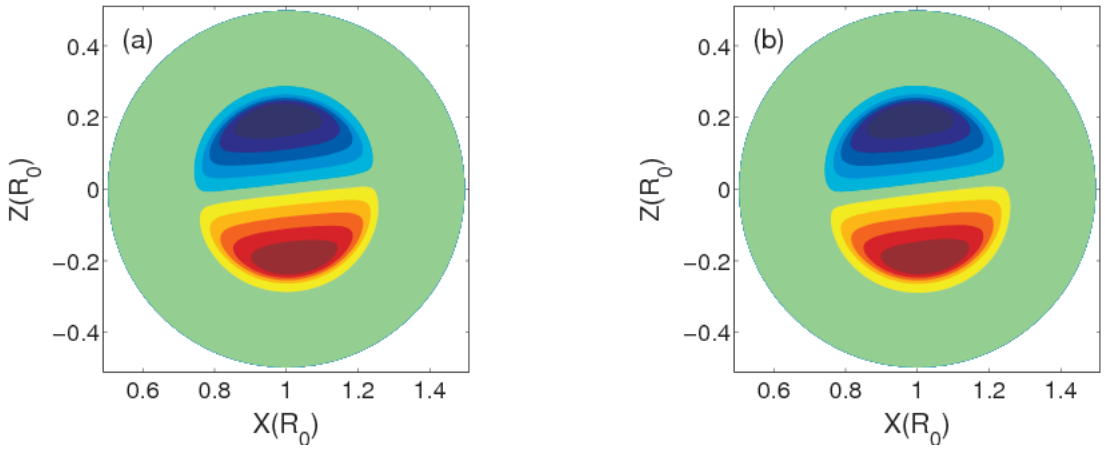

Figure 4.11: The internal kink mode structure $\delta\phi$ on the $\zeta = 0$ poloidal plane are plotted. The finite differences mode structure is plotted in panel(a), and finite element mode structure is plotted in panel(b).

4.6 Summary

A method extending the simulation domain to the magnetic axis was implemented in GTC. With this capability, the internal kink mode was simulated in both cylindrical and toroidal geometry. In the cylindrical geometry, the simulations were benchmarked and showed good agreement with ideal MHD. In the toroidal geometry, fluid simulations have a similar growth rate compared to the fluid simulations in the cylindrical geometry. However, for the realistic toroidal geometry model there is a change in mode structure due to the change in magnetic field configuration. When ion kinetic effects are added to the toroidal geometry simulation, the internal kink mode growth rate is significantly reduced even when the radial width of the perturbed current layer is an order of magnitude larger than the banana orbit width. Nevertheless, this reduction of growth rate is attributed fully to the ion kinetic effects.

Chapter 5

Internal kink mode in astrophysical jet

Powerful astrophysical jets and radial lobes are often observed near active galactic nuclei, where a stream of plasma emerges from the center of a galaxy. These jets can reach lengths of tens of kiloparsecs(i.e. many orders of magnitude larger than the radius of the jets)[42].

Accretion disks which can produce large scale magnetic fields around the black hole are believed to play a pivotal role in the launching of astrophysical jets [79, 80, 81, 82]. Astrophysical jet formation and collimation has been investigated in both the hydrodynamic limit [83, 84, 85], where the kinetic energy in the jet is assumed to be much greater than the magnetic energy, and in the Poynting flux limit[86, 87, 88, 89, 90, 91], where the energy from the accretion disk is carried predominantly by the electromagnetic field.

To maintain collimation over length scales of kiloparsecs(1 kiloparsec = 3262 light years), the plasma must be incredibly stable. Jet propagation and stability has been investigated extensively in the hydrodynamic limit. Many researchers have performed simulations similar to the work of Norman et al.[92] which studied how highly supersonic matter propagates in a

background medium[93, 94, 95, 96, 97]. Overall, even though some of these studies included a background magnetic field, they found that the jets in this regime tend to be highly unstable to the hydrodynamic Kelvin-Helmholtz instability driven by sheared flows.

Recent observations have suggested that the magnetic energy inside the radio lobes of the jet is large[44, 98]. This suggests that the magnetic energy inside the jet could also be significant and that the jet could possibly be magnetically dominated. A strong magnetic field could help suppress the Kelvin-Helmholtz instability and explain how these jets are able to remain collimated over such long distances. However, such a jet would most likely be unstable to dangerous kink modes associated with the current that produces the magnetic field, which has been studied extensively in fusion literature.

Another open problem in active galactic nuclei is in understanding the source of ultra-high-energy cosmic rays that have been observed with energies up to 10^{20} eV. It has been speculated that since jets contain a significant amount of energy from the supermassive black hole, the acceleration of these cosmic rays likely occur in the jets or lobes[99]. The acceleration mechanism for these cosmic rays is currently unknown and an area of active research, as they cannot be explained through relativistic shocks in the launching of jets using conventional Fermi acceleration[50, 51].

In this chapter, we describe the first gyrokinetic simulation of kink modes in a proposed astrophysical jet equilibrium to investigate the stability of the jet and mechanisms for production of ultra-high-energy cosmic rays, which was done in collaboration with Hui Li and Ken Fowler. First, a magnetically dominated model is introduced. Then, a brief overview of the magnetic field structure in the accretion disk as derived in Colgate et al.[46] is presented. Using the structure of the magnetic fields in the accretion disk, a potential equilibrium for the jet is constructed. With this equilibrium, the linear stability properties of kink modes in the jet are examined, where the kink modes for the jet equilibrium are found to vary significantly in mode structure and growth rate from the kink modes seen in

tokamaks. Next, in an attempt to understand the ultra-high-energy cosmic rays, a potential mechanism for particle acceleration in the jet is proposed. Nonlinear dynamics of the kink modes are also examined, where the kink is observed to saturate and remain benign. A brief discussion is given for kink modes being able to create parallel electric field which can accelerate particles to large energies.

5.1 Model for magnetically dominated astrophysical jet

In this section, the properties of the magnetically dominated jet model are explained as an aid in understanding this model. An illustration of an astrophysical jet from Colgate et al.[46] is shown in Figure 5.1 that shows the structure of the magnetic fields. This illustration depicts a jet of length L and radius R that is propagating upward on the page, and shows important characteristics of the jet such as: the central column, accretion disk, diffuse pinch region, and the closing of the current loop.

Using cylindrical coordinates(r,θ,z), Figure 5.1 describes the astrophysical jet model with the jet being axisymmetric in the θ-direction. The supermassive black hole is located at the origin ($r = 0$, $z = 0$). The accretion disk shown at the bottom of the left figure is a diffuse plasma structure orbiting the black hole. This disk produces the initial magnetic fields and is believed to be important in the initial launching of the jet. At the end of the jet $z = L$ is the nose, where the current begins the return back to the accretion disk to close the magnetic field lines. Breaking the jet into radial sections, the central column $r \leq a$ which is shown as the red bar in Figure 5.1 is where the majority of the plasma current is located. Figure 5.1 also defines the diffuse pinch region $a < r \leq R_0$, which is radially outward from the central column and where the plasma current falls off rapidly. Next is the closed flux region $r > R_0$,

where the λ-profile $\lambda = j_z/B_z$ is approximately constant, and lastly is the region where the current returns.

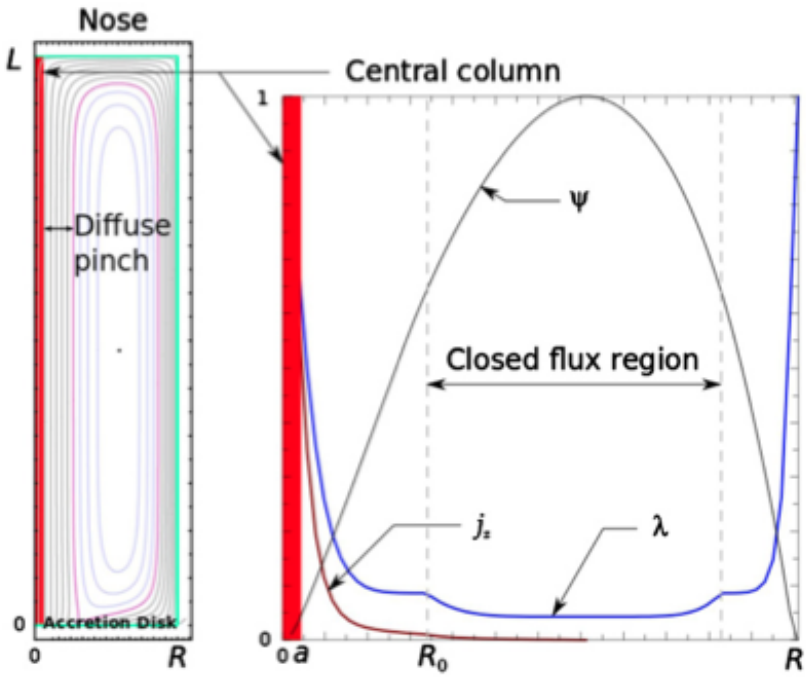

Figure 5.1: On the left is a simplified sketch of the magnetic field structure produced by the jet that was launched by the accretion disk. On the right, various properties of the jet are plotted, including the axial current j_z, poloidal flux function ψ, and the lambda profile $\lambda = j_z/B_z$. This figure is reproduced by permission of the AAS.

5.2 Structure of magnetic fields in accretion disk

The behavior of the equilibrium magnetic fields in the accretion disk could have a strong influence on the fields in the jet. A brief description of the derivation of the magnetic fields structure in the accretion disk by Colgate et al.[46] is given here. The accretion disk has a finite length that starts at $z = 0$ and ends at $z = H$, where the thickness of the accretion disk is much smaller than the length of the jet $H \ll L$. The behavior of the fields in the disk comes from the momentum equation of the accretion disk. To obtain this behavior, using the boundary conditions of $B_r = 0$ at $z = H$, and that the jet begins where gravity induced

accretion ceases(i.e. hydrodynamic terms approach zero at $z = H$), the accretion disk radial momentum equation can be written as the pressureless screw pinch equation,

$$\frac{\partial B_{z,disk}^2}{\partial r} + \frac{1}{r^2}\frac{\partial \left(r^2 B_{\theta,disk}^2\right)}{\partial r} = 0; \quad \text{at } z = H, \tag{5.1}$$

where $B_{z,disk}$ and $B_{\theta,disk}$ are axial and azimuthal magnetic field in the accretion disk. The length of the accretion disk $z = [0, H]$ is integrated over for the angular momentum equation and the following equation is obtained:

$$g\left[\dot{M}/2\Omega_K\right] = r\left(rB_{\theta,disk}\left|B_{z,disk}\right|\right)_{r,H}, \tag{5.2}$$

where g represents the fraction of the angular momentum extracted by the jet and is defined as:

$$g = \left[\dot{M}/2\Omega_K\right]^{-1}\int_0^H dz\, 4\left(\pi/r\right)\frac{\partial}{\partial r}\left\{r\rho|v_r|r^2\Omega\left[1 + (\nu/|v_r|)\partial(\ln\Omega)/\partial r\right]\right\}, \tag{5.3}$$

where $\Omega_K = GM/r^3$ is the Kepler rotation of the disk with G being the Newtonian gravitational constant and M being the black hole mass. Ω is the accretion disk angular rotation velocity, and $\dot{M} = dM/dt$ is the mass accretion rate. The term ν is the kinematic viscosity of the disk, ρ is the mass density, and v_r is the accretion disk fluid velocity along the radial direction. By exploring the limiting cases when $g = 1$(zero viscosity), and when the accretion disk rotation is the Kepler rotation $\Omega = \Omega_K$, the behavior of the fields in the

diffuse pinch zone has been shown to be in the asymptotic limit when the radius is much larger than the central column $r >> a$:

$$\begin{aligned} B_{z,disk} &\propto r^{-3/2}, \\ B_{\theta,disk} &\propto r^{-1}. \end{aligned} \tag{5.4}$$

These asymptotic expressions for the magnetic fields in the accretion disk are used to construct the magnetic fields in the jet in the following section.

5.3 Equilibrium model for the jet

In this section, an equilibrium magnetic field model for an astrophysical jet is constructed. The simulation region that will be studied in this work contains only a small section of the jet near the central column, thus the equilibrium magnetic fields are assumed to be symmetric along θ and z. Making the assumption that the behavior of the fields in the jet are similar to the fields in the accretion disk, the magnetic fields are chosen to have the same asymptotic relation as the disk. One choice that satisfies the asymptotic expression in equation 5.4 is the approximate axial magnetic field $B_{z,approx}$ and approximate azimuthal magnetic field $B_{\theta,approx}$ are:

$$\begin{aligned} B_{z,approx} &= B_{0a}[1 + (r/a)^{3/2}]^{-1}, \\ B_{\theta,approx} &= B_{0a}(r/a)[1 + (r/a)^{2}]^{-1}, \end{aligned} \tag{5.5}$$

where B_{0a} is the on-axis magnetic field. While these approximate fields satisfy the behavior of the asymptotic expressions in Equation 5.4 when the radial distance is much greater than the central column $r \gg a$, they do not represent a force free equilibrium. To obtain force free fields B_z and B_θ in the jet, we use the equations for the q-profile and the pressureless screw pinch equilibrium, shown below. The q-profile is defined as:

$$q = (2\pi r B_z)/(L B_\theta) = \frac{2\pi a}{L} \frac{1 + (r/a)^2}{1 + (r/a)^{3/2}}, \tag{5.6}$$

and the screw pinch equilibrium pressure equation is:

$$\frac{\partial}{\partial r}\left(\frac{B_\theta + B_z}{2\mu_0}\right) + \frac{B_\theta}{\mu_0 r} = 0. \tag{5.7}$$

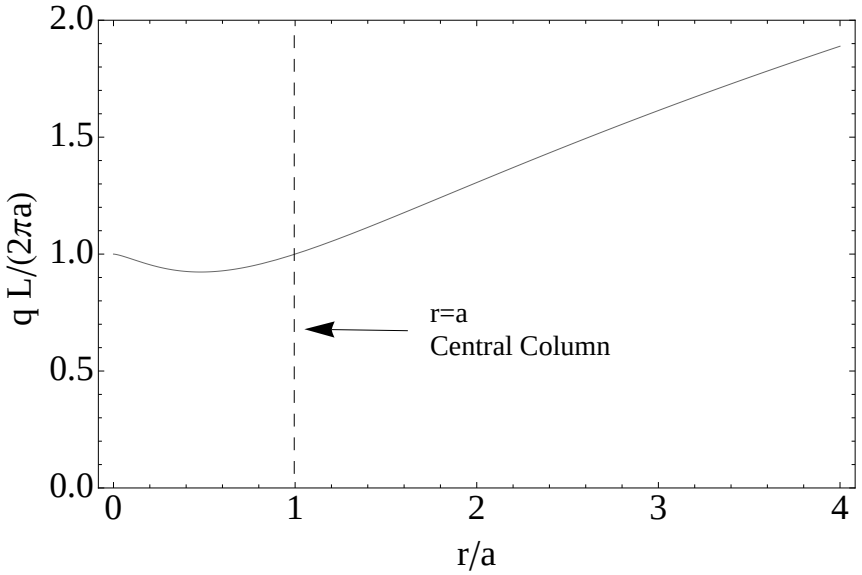

Figure 5.2: The normalized q-profile is plotted vs. radial coordinate r/a.

Solving these two equations, a numerical equilibrium is constructed for the jet fields B_z and B_θ. The numerical values of B_z and B_θ are plotted in Figure 5.3 along with the approximate analytical expressions $B_{z,approx}$ and $B_{\theta,approx}$. While the numerical fields and the approximate fields are noticeably different near the central column, the numerical fields still retain the desired asymptotic behavior of Equation 5.4.

In tokamak geometry, the q-profile is the most important quantity in determining the strength of the kink instability and the shape of the mode structure. In astrophysical jets, there is no physical periodicity in the axial direction, and modes of any k_z are possible. With the assumption that the mode resonance will be somewhat near the central column, then the modes of interest are on a much smaller length scale than the jet length, and it is safe to assume that the modes are periodic in the axial direction(i.e., we consider a local problem in the axial direction). In the jet, an nq-profile can be used to determine stability properties of the internal kink mode for a specific k_z, where n is the axial mode number. We define the wavelength along the plasma column as $\lambda_z = L/n$ and wave vector as $k_z = 2\pi/\lambda_z$, with $n \gg 1$. If there is an $nq = 1$ surface, then the internal kink mode will be unstable. For these simulations, $n \gg 1$, but for simplicity only one wavelength in the z-direction will be simulated $\Delta z = L/n = \lambda_z$.

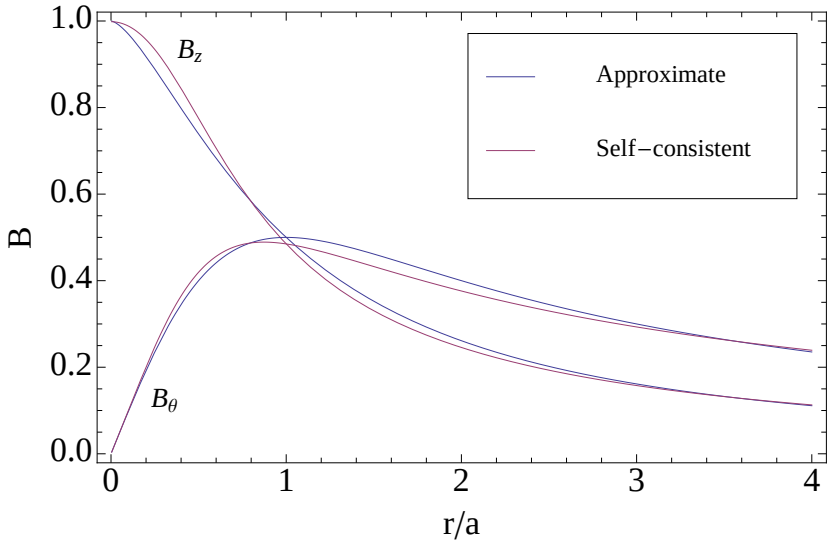

Figure 5.3: The axial and poloidal field are plotted vs. radial coordinate r/a. The approximate analytic expressions for magnetic fields are plotted in blue and self-consistent magnetic fields in red.

GTC does not use the vector components of the equilibrium magnetic fields B_z and B_θ directly. Rather, GTC uses the magnetic flux coordinates with scalar quantities of current, total magnetic field, and safety factor. To implement equilibrium quantities into GTC, the poloidal current $2\pi g$, toroidal current $2\pi I$, the safety factor q, and total magnetic field strength B_0 are needed. In cylindrical geometry, these physical quantities can be written in terms of the azimuthal and axial magnetic field.

$$\begin{aligned} B_0 &= B_z^2 + B_\theta^2, \\ I &= rR_0B_\theta, \\ g &= B_zR_0^2 \\ q &= rB_z/R_0B_\theta \end{aligned} \tag{5.8}$$

For these jet simulations, we simulate a wavelength λ_z in the axial direction. The toroidal angle is defined as $\zeta = 2\pi z/\lambda_z$, where z is the axial position and λ_z is the length of the cylinder section being simulated. The effective major radius for the cylindrical geometry is $R_0 = \lambda_z/2\pi$, and a periodic boundary condition is used for the toroidal angle.

5.4 Linear simulations

The actual strength of the magnetic fields in the jet are unknown. We assume that the jet is magnetically dominated and that the gyroradius is very small compared the jet. It is convenient to use the same parameters as the tokamak simulations in Chapter 4 which satisfy both these conditions. With plasma beta $\beta_e = 0.4\%$ and ion gyroradius $\rho_i/a = 0.001$, these quantities should be sufficiently small.

In Figure 5.4, the growth rate of the kink mode is plotted while varying the axial wave vector k_z. A maximum growth rate is found when $k_z a = 0.8$, or when the z-length is about 8 times of the radius of the central column. To explain the peak growth rate of this kink, two limiting cases are examined. When $k_z a > 1$, the main limit is that the nq-profile raises above unity to stabilize the kink. In the long wavelength limit $k_z a \ll 1$, the typical kink growth rate is limited by the Alfvén speed $\gamma \propto k_z v_A$[100]. This results in the largest growth rate lying between these two k_z values. We also note that the growth rates for this jet model are large for internal kink modes with growth rates on the order of $0.1\,\omega_A$, where $\omega_A = v_A/R_0$. In the tokamak simulations performed in Chapter 4, growth rates were on the order of $0.01\,\omega_A$.

In Figure 5.5, the mode structure of the internal kink mode for astrophysical jets and for the tokamak case are plotted vs. radial coordinate r/a. The astrophysical jet mode structure is significantly different than the tokamak mode structure. Where the tokamak case has a thin layer at the $q = 1$ surface, there is no such layer for the astrophysical jet case. The peak

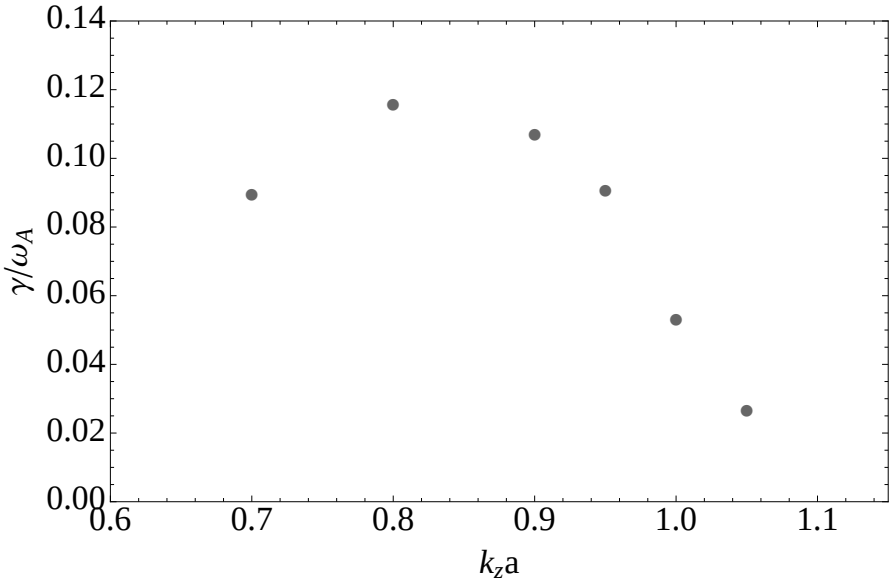

Figure 5.4: The growth rates are plotted against the normalized axial wave number $k_z a$.

of the mode structure for the astrophysical jet is near the plasma column $r = a$, where the peak of the equilibrium current is. The mode structure of $\delta\phi$ in this case also has a long tail in the radial direction, where the mode gradually approaches zero.

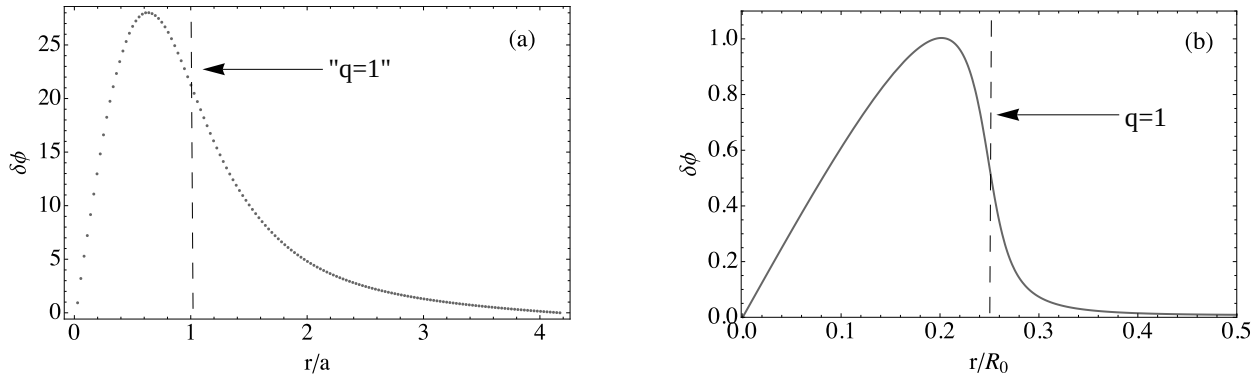

Figure 5.5: Panel(a): the mode structure of the electrostatic potential for the jet equilibrium with $k_\theta/k_z = 0.9$. Panel(b): the mode structure of the electrostatic potential for a typical tokamak with $k_\theta/k_z = 4$

As seen in the tokamak equilibria, when the $k_\theta \gg k_z$, the resonant layer at the mode rational surface is sharp. This has been explored in Appendix A, where it is shown that the size of the layer at the mode rational surface is heavily dependent on the aspect ratio a/R_0 or the ratio between the wave vector in the azimuthal direction to the wave vector in the axial direction

k_θ/k_z. The layer broadens as k_θ/k_z decreases. In the tokamak case shown in Figure 5.5, the mode structure is already fairly broad at $k_\theta/k_z = 4$. For this astrophysical jet equilibrium, the $k_\theta/k_z \sim 1$, so the perturbed current layer should be very broad to the point where the current layer scale length is on the same order as the global kink mode structure. So the difference in mode structure between the astrophysical jet case and the classic tokamak case can be explained by the ratio of k_θ/k_z.

We also note that for this astrophysical jet equilibrium, the resonant surface of the mode is far away from the bulk of the mode structure. This property is similar to an external mode where the resonant surface would be outside of the plasma.

5.5 Potential mechanism for acceleration

The physical mechanism that accelerates cosmic rays to ultra high energies is currently unknown since it can not be explained by conventional acceleration mechanisms[50, 51]. Using MHD dynamo theory[101], the fields created by a saturated kink mode could potentially be the source of the acceleration. Dynamo theory has been used to explain how magnetic fields are maintained in planets and stars, and is required to explain how a large spatial scale magnetic field can be maintained throughout the jet. There has been some experimental evidence of this volume averaged electric field arising from the dynamo effects. On the spheromak SPHEX, there was observed ion acceleration and a significant volume averaged parallel electric field [102]. Picturing the jet as a large circuit, the current of this circuit travels through the central column of the jet, turns around at the nose, and returns the current in the radio lobes. A DC parallel electric field would then be required to maintain the current in the jet. MHD dynamo theory suggests that the fluctuations between the plasma bulk velocity and the magnetic field $\delta\mathbf{v} \times \delta\mathbf{B}$ could potentially provide this mean

parallel electric field and can maintain the current in the jet. The magnetic energy that is lost due to resistivity is replaced by $\delta\mathbf{v} \times \delta\mathbf{B}$. This can be seen by looking at Ohm's law:

$$\mathbf{E} + \delta\mathbf{v} \times \mathbf{B_0}/c \approx \overline{\delta\mathbf{v} \times \delta\mathbf{B}/c} = \mathbf{D}, \tag{5.9}$$

where $\mathbf{D}$ represents a hyper-resistivity which describes transport. Then the mean parallel electric field can be written as

$$\overline{\delta E_{||}} = \overline{\mathbf{b} \cdot \delta\mathbf{v} \times \delta\mathbf{B}/c} = \mathbf{b} \cdot (\delta\mathbf{u}_E \times \delta\mathbf{B})/c, \tag{5.10}$$

With a turbulent electric field $\delta\mathbf{E} = \mathbf{a}\cos\omega t + \mathbf{b}\cos\omega t$ and magnetic field $\delta\mathbf{B} = \mathbf{c}\cos\omega t + \mathbf{d}\cos\omega t$, then $\delta E_{||}$ could have a finite DC component if $\delta\mathbf{E}$ and $\delta\mathbf{B}$ are not perfectly out of phase. While in linear ideal MHD $\delta\mathbf{E}$ and $\delta\mathbf{B}$ are out of phase, with non-ideal MHD effects and nonlinear effects, $\overline{\delta E_{||}}$ could potentially be non-zero.

Going one step further, we suggest that these fluctuations could be a source of particle acceleration, where the fluctuations between the bulk plasma velocity and the magnetic field can create a volume averaged parallel electric field, and this electric field could accelerate particles to high energies. We propose a model where acceleration occurs as it would in a laboratory plasma when plasma is connected to a voltage source when density is so low that

voltage causes ions to "run away", only impeded by radiation. In this simple circuit, the parallel acceleration equation of ions is:

$$\frac{dp_{||}}{dt} = e(E_{||} - E_{RAD}), \tag{5.11}$$

where $p_{||}$ is the ion momentum, $E_{||}$ is the parallel electric field, and E_{RAD} represents deceleration due to radiation. This flux averaged electric field that is discussed in this section was introduced into GTC in the form of: $\overline{\delta E_{||}} = \mathbf{b} \cdot (\delta \mathbf{u}_E \times \delta \mathbf{B}) / c$, as was derived by Wang et al., and is described in section 2.3.

5.6 Nonlinear simulations

In this section, nonlinear simulations are performed to find stability properties and to look for a volume average parallel electric field that could accelerate particles. We will focus on the nonlinear mode properties of the $k_z a = 0.9$ case.

Figure 5.6 shows the nonlinear evolution of the kink quantities $\delta A_{||}$ and $\delta\phi$ including saturation for three gyrokinetic cases. The first case is a gyrokinetic simulation ignoring the parallel nonlinear physics and zonal fields. This simulation does not saturate, and the kink instability grows until the simulation blows up. For the second case, a gyrokinetic simulation is performed which incorporates the ion parallel nonlinearity, but excludes zonal fields. This case has a saturation level that corresponds to a perturbed magnetic field of $\delta B/B_0 = 0.01$. The evolution of the perturbed electrostatic potential $\delta\phi$ is chaotic after saturation compared to the mangetic potential $\delta A_{||}$. Lastly, a simulation is performed with parallel nonlinearity and the addition of zonal flows and currents. This simulation has the lowest saturation amplitude of $\delta B = 0.003$, however, the non-zonal electrostatic potential

is highly oscillatory with a frequency of $\omega \sim \omega_A$. This results in the simulation becoming numerically unstable shortly after saturation.

Since the saturation of the perturbed magnetic field is small compared to the equilibrium magnetic field, the plasma should be relatively undisturbed by this saturated kink. With a low saturation amplitude, these saturated kinks could nonlinearly evolve in the astrophysical jet, and provide turbulent fields to accelerate ions.

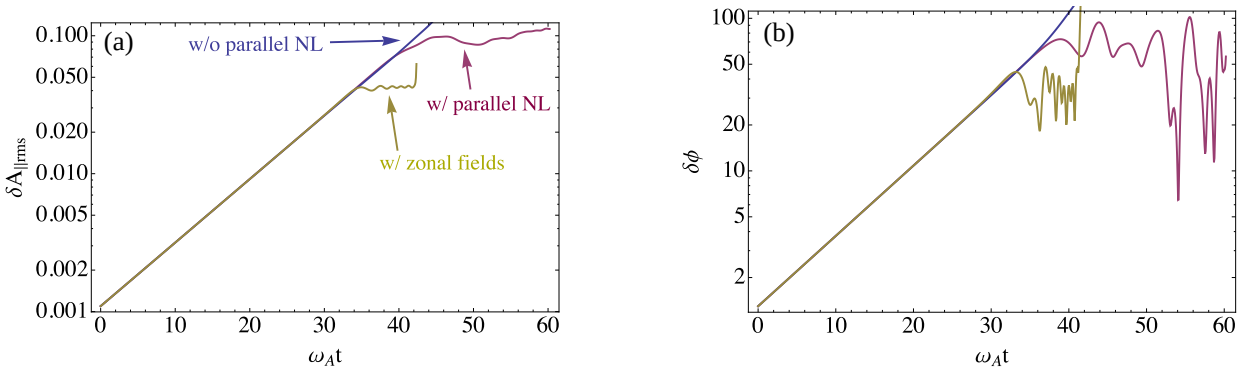

Figure 5.6: Panel(a): The nonlinear behavior of perturbed magnetic potential $\delta A_{||}$ is plotted. Panel(b): The behavior of the electrostatic potential $\delta\phi$ is plotted.

Next, the volume average parallel electric field $\overline{\delta E_{||}}$ as was discussed in Section 2.3 and 5.5 will be investigated. Figure 5.7 shows the radial-time history of zonal quantity $\overline{\delta E_{||}}$ that is calculated without being fed back into the simulation for the "w/ parallel NL" case(i.e., zonal fields are not kept in the simulation). The electric field $\overline{\delta E_{||}}$ shows no strongly coherent mode structure, and has a saturation amplitude of $\overline{\delta E_{||}} R_0/\phi_{rms} \sim 10^{-8}$. The small amplitude of $\overline{\delta E_{||}}$ and the lack of a coherent radial structure reduces the prospect of the internal kink accelerating particles.

The self-consistent simulation with zonal fields could enhance the electric field $\overline{\delta E_{||}}$, which will be studied in the future work. We point out that this is our first attempt of nonlinear gyrokinetic simulation of the internal kink modes. More nonlinear simulations are needed

to clarify the nonlinear saturation mechanism and the possible mechanism of particle acceleration.

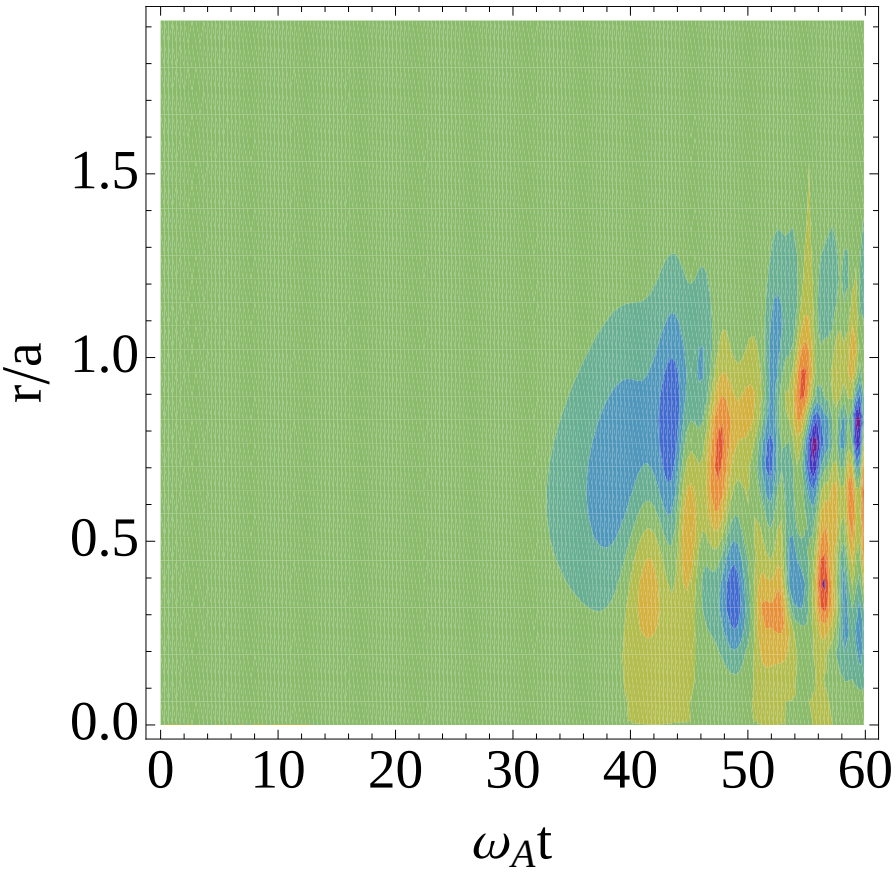

Figure 5.7: The zonal parallel electric field $\overline{\delta E_{||}}$ is plotted in the radial-time space for the "parallel NL" case.

5.7 Summary

Using the experience from kink mode simulation in tokamaks, kink modes in astrophysical jets have been simulated using GTC. First, a numerical equilibrium is constructed for a potential jet magnetic field configuration. Linear stability properties were then examined where it was found that the strongest kink instability had an axial length eight times of the radius of the central column, and that the internal kink mode structure varies significantly to the standard tokamak picture of the kink mode. In the nonlinear regime, the kink mode

saturates at a low amplitude where the magnetic field remains relatively unperturbed. There are two saturation mechanisms of the kink observed from the ion kinetic effects: the parallel nonlinearity and generation of zonal flows. We also observe a volume averaged parallel electric field, but this field is small compared to the rms electric field and it is fairly turbulent. A more detailed nonlinear investigation will be performed in the future work.

Chapter 6

Conclusions

In this thesis, Gyrokinetic Toroidal Code has been applied to further understand the physics for current-driven MHD instabilities. As a first step to learn GTC, stability parameters of the toroidal Alfvén eigenmode were examined for the hybrid and the steady state scenario in ITER. To perform these tests we first implemented a slowing down fast alpha distribution into GTC. The steady state scenario has a lower alpha beta threshold than the hybrid scenario. This suggests that the TAEs could be more unstable in the steady state running scenario in ITER which could lead to more energetic particle transport. We also note that both thresholds are close to marginal stability for their respective equilibrium. These simulations are missing effects from energetic beam ions, which could drive the TAEs unstable.

Next, a method extending the simulation domain to the magnetic axis was implemented into GTC. With this capability, the current-driven internal kink mode was simulated in both the cylindrical and toroidal geometry. In the cylindrical geometry, the simulations were benchmarked and showed good agreement with ideal MHD. In the toroidal geometry, fluid simulations have a similar growth rate compared to the fluid simulations in the cylindrical geometry. However, for the realistic toroidal geometry model there is a change in mode

structure due to the change in magnetic field configuration. When ion kinetic effects are added to the toroidal geometry simulation, the internal kink mode growth rate is significantly reduced even when the radial width of the perturbed current layer is an order of magnitude larger than the banana orbit width. Nevertheless, this reduction of growth rate is attributed fully to the ion kinetic effects.

Using the experience from kink mode simulation in tokamaks, kink modes in astrophysical jets have been simulated using GTC. First, a numerical equilibrium is constructed for a model jet magnetic field configuration. Linear stability properties were then examined where it was found that the strongest kink instability has an axial length eight times of the radius of the central column, and that the internal kink mode structure varies significantly from the standard tokamak picture of the kink mode. This astrophysical jet kink saturates at a low amplitude where the equilibrium magnetic field remains relatively unperturbed. The saturation mechanisms of the kink observed are from the parallel nonlinearity and generation of zonal flows. There is an observed flux surface averaged parallel electric field that is generated from this saturated kink, but it is small compared to the total electric field.

Future work for this thesis project will include improvements upon the current-driven MHD simulation capabilities. One example is that the gyrokinetic equation and electron continuity equation are still written using magnetic flux coordinates which rely on gradients that are singular near the magnetic axis. One potential solution to this problem is to write these equations using a finite element method, similar to the finite element implementation of the Laplacian operator presented in this thesis. Another example is to figure out how to properly handle the $m = 0$ harmonic of the kink, which can cause numerical problems in gyrokinetic simulations of the kink and fishbone mode in a realistic geometry with a finite pressure gradient. One potential method which might ease this problem is to use the gyrokinetic vorticity equation instead of the gyrokinetic Poisson equation, and explicitly cancel the E x B terms which are likely the source of this strong $m = 0$ harmonic of the kink

in the electron and ion density. This type of method has been used to improve simulation performance of low-n TAEs[103].

The gyrokinetic capabilities developed during this research on the current-driven internal kink mode has led to the verification of a resistive tearing model in GTC[60] and to gyrokinetic simulations of the fishbone mode in DIII-D. The future work for current-driven instabilities in tokamaks is to make a detailed comparison for the kink and fishbone modes in the DIII-D and NSTX tokamaks. Investigation into what plasma parameters such as the fast ion gradient and q-profile would produce long-lived saturated kinks, and what parameters would excite fishbone modes on these devices will be performed. Next is to extend simulations to the nonlinear regime for kink and fishbone modes and examine saturation mechanism and nonlinear evolution. A longer term goal is to self-consistently simulate the dangerous neoclassical tearing mode which may trigger disruptions in ITER. This would require simulation of neoclassical effects which have been implemented in GTC, and further development of nonlinear simulation capabilities of current-driven MHD modes.

Future work for the astrophysical jet kink simulations include further investigation into the nonlinear saturation mechanism of the jet and possible production of a flux surface averaged parallel electric field. This flux surface averaged parallel electric field was hypothesized to be produced from saturated kink modes. If nonlinear simulation times could be extended further incorporating zonal fields, then maybe this DC electric field could be observed. Also, periodic boundary conditions that are imposed in the axial direction could potentially impede production of this parallel electric field. While it would be quite difficult to use non-periodic boundary conditions in GTC, simulation of multiple axial wave numbers might aid in observing this field.

Bibliography

[1] J. McClenaghan, Z. Lin, I. Holod, W. Deng, and Z. Wang. Verification of gyrokinetic particle simulation of current-driven instability in fusion plasmas. i. internal kink mode. *Physics of Plasmas (1994-present)*, 21(12):122519, 2014.

[2] Marshall N. Rosenbluth, R. Y. Dagazian, and P. H. Rutherford. Nonlinear properties of the internal m=1 kink instability in the cylindrical tokamak. *Physics of Fluids (1958-1988)*, 16(11):1894–1902, 1973.

[3] Harold P. Furth, John Killeen, and Marshall N. Rosenbluth. Finiteresistivity instabilities of a sheet pinch. *Physics of Fluids (1958-1988)*, 6(4), 1963.

[4] K. McGuire, R. Goldston, M. Bell, M. Bitter, K. Bol, K. Brau, D. Buchenauer, T. Crowley, S. Davis, F. Dylla, H. Eubank, H. Fishman, R. Fonck, B. Grek, R. Grimm, R. Hawryluk, H. Hsuan, R. Hulse, R. Izzo, R. Kaita, S. Kaye, H. Kugel, D. Johnson, J. Manickam, D. Manos, D. Mansfield, E. Mazzucato, R. McCann, D. McCune, D. Monticello, R. Motley, D. Mueller, K. Oasa, M. Okabayashi, K. Owens, W. Park, M. Reusch, N. Sauthoff, G. Schmidt, S. Sesnic, J. Strachan, C. Surko, R. Slusher, H. Takahashi, F. Tenney, P. Thomas, H. Towner, J. Valley, and R. White. Study of high-beta magnetohydrodynamic modes and fast-ion losses in pdx. *Phys. Rev. Lett.*, 50:891–895, Mar 1983.

[5] S. von Goeler, W. Stodiek, and N. Sauthoff. Studies of internal disruptions and $m = 1$ oscillations in tokamak discharges with soft¯x-ray tecniques. *Phys. Rev. Lett.*, 33:1201–1203, Nov 1974.

[6] Z. Chang, J. D. Callen, E. D. Fredrickson, R. V. Budny, C. C. Hegna, K. M. McGuire, M. C. Zarnstorff, and TFTR group. Observation of nonlinear neoclassical pressure-gradient˘driven tearing modes in tftr. *Phys. Rev. Lett.*, 74:4663–4666, Jun 1995.

[7] D. Pfirsch and H. Tasso. A theorem on mhd-instability of plasmas with resistive walls. *Nuclear Fusion*, 11(3):259, 1971.

[8] T.C. Hender, J.C Wesley, J. Bialek, A. Bondeson, A.H. Boozer, R.J. Buttery, A. Garofalo, T.P Goodman, R.S. Granetz, Y. Gribov, O. Gruber, M. Gryaznevich, G. Giruzzi, S. Gnter, N. Hayashi, P. Helander, C.C. Hegna, D.F. Howell, D.A. Humphreys, G.T.A. Huysmans, A.W. Hyatt, A. Isayama, S.C. Jardin, Y. Kawano, A. Kellman, C. Kessel, H.R. Koslowski, R.J. La Haye, E. Lazzaro, Y.Q. Liu, V. Lukash,

J. Manickam, S. Medvedev, V. Mertens, S.V. Mirnov, Y. Nakamura, G. Navratil, M. Okabayashi, T. Ozeki, R. Paccagnella, G. Pautasso, F. Porcelli, V.D. Pustovitov, V. Riccardo, M. Sato, O. Sauter, M.J. Schaffer, M. Shimada, P. Sonato, E.J. Strait, M. Sugihara, M. Takechi, A.D. Turnbull, E. Westerhof, D.G. Whyte, R. Yoshino, H. Zohm, Disruption the ITPA MHD, and Magnetic Control Topical Group. Chapter 3: Mhd stability, operational limits and disruptions. *Nuclear Fusion*, 47(6):S128, 2007.

[9] Xian-Qu Wang, Rui-Bin Zhang, Liang Qin, and Xiao-Gang Wang. Non-resonant fishbone instabilities of q min1 in tokamak plasmas with weakly reversed magnetic shear. *Plasma Physics and Controlled Fusion*, 56(9):095013, 2014.

[10] Huishan Cai and Guoyong Fu. Hybrid simulation of energetic particle effects on tearing modes in tokamak plasmas. *Physics of Plasmas (1994-present)*, 19(7):072506, 2012.

[11] Charlson C. Kim and the NIMROD team. Impact of velocity space distribution on hybrid kinetic-magnetohydrodynamic simulation of the (1,1) mode. *Physics of Plasmas (1994-present)*, 15(7):072507, 2008.

[12] Q. Yu and S. Gunter. Locking of neoclassical tearing modes by error fields and its stabilization by rf current. *Nuclear Fusion*, 48(6):065004, 2008.

[13] A. J. Brizard and T. S. Hahm. Foundations of nonlinear gyrokinetic theory. *Rev. Mod. Phys.*, 79:421–468, Apr 2007.

[14] Z. Lin, I. Holod, L. Chen, P. H. Diamond, T. S. Hahm, and S. Ethier. Wave-particle decorrelation and transport of anisotropic turbulence in collisionless plasmas. *Phys. Rev. Lett.*, 99:265003, Dec 2007.

[15] Yong Xiao and Zhihong Lin. Turbulent transport of trapped-electron modes in collisionless plasmas. *Phys. Rev. Lett.*, 103:085004, Aug 2009.

[16] Wenlu Zhang, Zhihong Lin, and Liu Chen. Transport of energetic particles by microturbulence in magnetized plasmas. *Phys. Rev. Lett.*, 101:095001, Aug 2008.

[17] H. S. Zhang, Z. Lin, and I. Holod. Nonlinear frequency oscillation of alfvén eigenmodes in fusion plasmas. *Phys. Rev. Lett.*, 109:025001, Jul 2012.

[18] Zhixuan Wang, Zhihong Lin, Ihor Holod, W. W. Heidbrink, Benjamin Tobias, Michael Van Zeeland, and M. E. Austin. Radial localization of toroidicity-induced alfvén eigenmodes. *Phys. Rev. Lett.*, 111:145003, Oct 2013.

[19] D. A. Spong, E. M. Bass, W. Deng, W. W. Heidbrink, Z. Lin, B. Tobias, M. A. Van Zeeland, M. E. Austin, C. W. Domier, and N. C. Luhmann. Verification and validation of linear gyrokinetic simulation of alfvn eigenmodes in the diii-d tokamak. *Physics of Plasmas (1994-present)*, 19(8):082511, 2012.

[20] Hiroshi Naitou, Kenji Tsuda, W. W. Lee, and R. D. Sydora. Gyrokinetic simulation of internal kink modes. *Physics of Plasmas (1994-present)*, 2(11):4257–4268, 1995.

[21] Alexey Mishchenko and Alessandro Zocco. Global gyrokinetic particle-in-cell simulations of internal kink instabilities. *Physics of Plasmas (1994-present)*, 19(12):122104, 2012.

[22] W. W. Heidbrink. Basic physics of alfvn instabilities driven by energetic particles in toroidally confined plasmasa). *Physics of Plasmas (1994-present)*, 15(5):055501, 2008.

[23] K. L. Wong, R. J. Fonck, S. F. Paul, D. R. Roberts, E. D. Fredrickson, R. Nazikian, H. K. Park, M. Bell, N. L. Bretz, R. Budny, S. Cohen, G. W. Hammett, F. C. Jobes, D. M. Meade, S. S. Medley, D. Mueller, Y. Nagayama, D. K. Owens, and E. J. Synakowski. Excitation of toroidal alfvén eigenmodes in tftr. *Phys. Rev. Lett.*, 66:1874–1877, Apr 1991.

[24] W.W. Heidbrink, E.J. Strait, E. Doyle, G. Sager, and R.T. Snider. An investigation of beam driven alfvn instabilities in the diii-d tokamak. *Nuclear Fusion*, 31(9):1635, 1991.

[25] M.N. Bussac, R. Pellat, D. Edery, and J.L. Soule. Internal kink modes in toroidal plasmas with circular cross sections. *Journal Name: Phys. Rev. Lett., v. 35, no. 24, pp. 1638-1641*, Dec 1975.

[26] BB Kadomtsev. Reconnection of field lines and disruptive instability in tokamaks. In *Plasma Physics and Controlled Nuclear Fusion Research 1976, Volume 1*, volume 1, pages 555–565, 1977.

[27] J. A. Wesson, B. Alper, A. W. Edwards, and R. D. Gill. Transport in the sawtooth collapse. *Phys. Rev. Lett.*, 79:5018–5021, Dec 1997.

[28] E A Lazarus et al. A comparison of sawtooth oscillations in bean and oval shaped plasmas. *Plasma Physics and Controlled Fusion*, 48(8):L65, 2006.

[29] H. Soltwisch. Measurement of currentdensity changes during sawtooth activity in a tokamak by farinfrared polarimetry (invited). *Review of Scientific Instruments*, 59(8), 1988.

[30] John Wesson. *Tokamaks*, volume 149. Oxford University Press, 2011.

[31] O. Sauter, R. J. La Haye, Z. Chang, D. A. Gates, Y. Kamada, H. Zohm, A. Bondeson, D. Boucher, J. D. Callen, M. S. Chu, T. A. Gianakon, O. Gruber, R. W. Harvey, C. C. Hegna, L. L. Lao, D. A. Monticello, F. Perkins, A. Pletzer, A. H. Reiman, M. Rosenbluth, E. J. Strait, T. S. Taylor, A. D. Turnbull, F. Waelbroeck, J. C. Wesley, H. R. Wilson, and R. Yoshino. Beta limits in long-pulse tokamak discharges. *Physics of Plasmas (1994-present)*, 4(5), 1997.

[32] J Jacquinot et al. Icrf studies on jet. *Plasma Physics and Controlled Fusion*, 28(1A):1, 1986.

[33] D. J. Campbell, D. F. H. Start, J. A. Wesson, D. V. Bartlett, V. P. Bhatnagar, M. Bures, J. G. Cordey, G. A. Cottrell, P. A. Dupperex, A. W. Edwards, C. D. Challis, C. Gormezano, C. W. Gowers, R. S. Granetz, J. H. Hammen, T. Hellsten, J. Jacquinot, E. Lazzaro, P. J. Lomas, N. Lopes Cardozo, P. Mantica, J. A. Snipes, D. Stork, P. E. Stott, P. R. Thomas, E. Thompson, K. Thomsen, and G. Tonetti. Stabilization of sawteeth with additional heating in the jet tokamak. *Phys. Rev. Lett.*, 60:2148–2151, May 1988.

[34] F Porcelli. Fast particle stabilisation. *Plasma Physics and Controlled Fusion*, 33(13):1601, 1991.

[35] F. Pegoraro, F. Porcelli, and T. J. Schep. Internal kink modes in the ionkinetic regime. *Physics of Fluids B: Plasma Physics (1989-1993)*, 1(2), 1989.

[36] R. B. White, P. H. Rutherford, P. Colestock, and M. N. Bussac. Sawtooth stabilization by energetic trapped particles. *Phys. Rev. Lett.*, 60:2038–2041, May 1988.

[37] G. Y. Fu, W. Park, H. R. Strauss, J. Breslau, J. Chen, S. Jardin, and L. E. Sugiyama. Global hybrid simulations of energetic particle effects on the n=1 mode in tokamaks: Internal kink and fishbone instability. *Physics of Plasmas (1994-present)*, 13(5):052517, 2006.

[38] Liu Chen, R. B. White, and M. N. Rosenbluth. Excitation of internal kink modes by trapped energetic beam ions. *Phys. Rev. Lett.*, 52:1122–1125, Mar 1984.

[39] J. E. Menard, R. E. Bell, D. A. Gates, S. M. Kaye, B. P. LeBlanc, F. M. Levinton, S. S. Medley, S. A. Sabbagh, D. Stutman, K. Tritz, and H. Yuh. Observation of instability-induced current redistribution in a spherical-torus plasma. *Phys. Rev. Lett.*, 97:095002, Aug 2006.

[40] I.T. Chapman, M.-D. Hua, S.D. Pinches, R.J. Akers, A.R. Field, J.P. Graves, R.J. Hastie, C.A. Michael, and the MAST Team. Saturated ideal modes in advanced tokamak regimes in mast. *Nuclear Fusion*, 50(4):045007, 2010.

[41] W. W. Heidbrink, Ralph Hay, and J. D. Strachan. Confinement of fusion reaction products during the fishbone instability. *Phys. Rev. Lett.*, 53:1905–1908, Nov 1984.

[42] Michael D. Smith. Astrophysical jets and beams. page 3, 2012.

[43] Marek Sikora, Mitchell C Begelman, and Martin J Rees. Comptonization of diffuse ambient radiation by a relativistic jet: The source of gamma rays from blazars? *The Astrophysical Journal*, 421:153–162, 1994.

[44] Frazer N Owen, Jean A Eilek, and Namir E Kassim. M87 at 90 centimeters: a different picture. *The Astrophysical Journal*, 543(2):611, 2000.

[45] Hui Li, Giovanni Lapenta, John M Finn, Shengtai Li, and Stirling A Colgate. Modeling the large-scale structures of astrophysical jets in the magnetically dominated limit. *The Astrophysical Journal*, 643(1):92, 2006.

[46] Stirling A Colgate, T Kenneth Fowler, Hui Li, and Jesse Pino. Quasi-static model of collimated jets and radio lobes. i. accretion disk and jets. *The Astrophysical Journal*, 789(2):144, 2014.

[47] Kenneth Greisen. End to the cosmic-ray spectrum? *Phys. Rev. Lett.*, 16:748–750, Apr 1966.

[48] G. T. Zatsepin and V. A. Kuz'min. Upper Limit of the Spectrum of Cosmic Rays. *Soviet Journal of Experimental and Theoretical Physics Letters*, 4:78, August 1966.

[49] Glennys R. Farrar and Andrei Gruzinov. Giant agn flares and cosmic ray bursts. *The Astrophysical Journal*, 693(1):329, 2009.

[50] ENRICO Fermi. On the origin of the cosmic radiation. *Phys. Rev.*, 75:1169–1174, Apr 1949.

[51] AM Hillas. The origin of ultra-high-energy cosmic rays. *Annual Review of Astronomy and Astrophysics*, 22:425–444, 1984.

[52] V Mukhovatov, M Shimada, A N Chudnovskiy, A E Costley, Y Gribov, G Federici, O Kardaun, A S Kukushkin, A Polevoi, V D Pustovitov, Y Shimomura, T Sugie, M Sugihara, and G Vayakis. Overview of physics basis for iter. *Plasma Physics and Controlled Fusion*, 45(12A):A235, 2003.

[53] Adrianus CC Sips et al. Advanced scenarios for iter operation. *Plasma physics and controlled fusion*, 47(5A):A19, 2005.

[54] Z. Lin, T. S. Hahm, W. W. Lee, W. M. Tang, and R. B. White. Turbulent transport reduction by zonal flows: Massively parallel simulations. *Science*, 281(5384):1835–1837, 1998.

[55] I. Holod, W. L. Zhang, Y. Xiao, and Z. Lin. Electromagnetic formulation of global gyrokinetic particle simulation in toroidal geometry. *Physics of Plasmas (1994-present)*, 16(12):122307, 2009.

[56] W. Deng, Z. Lin, and I. Holod. Gyrokinetic simulation model for kinetic magnetohydrodynamic processes in magnetized plasmas. *Nuclear Fusion*, 52(2):023005, 2012.

[57] W.W Lee. Gyrokinetic particle simulation model. *Journal of Computational Physics*, 72(1):243 – 269, 1987.

[58] Zhihong Lin and Liu Chen. A fluidkinetic hybrid electron model for electromagnetic simulations. *Physics of Plasmas (1994-present)*, 8(5), 2001.

[59] J. C. Cummings. Ph.d. thesis. *Princeton University*, 1995.

[60] Dongjian Liu, Wenlu Zhang, Joseph McClenaghan, Jiaqi Wang, and Zhihong Lin. Verification of gyrokinetic particle simulation of current-driven instability in fusion plasmas. ii. resistive tearing mode. *Physics of Plasmas (1994-present)*, 21(12):122520, 2014.

[61] Dongjian Liu and Liu Chen. A finite-mass fluid electron simulation model for low-frequency electromagnetic waves in magnetized plasmas. *Plasma Physics and Controlled Fusion*, 53(6):062002, 2011.

[62] R. B. White, A. H. Boozer, and Ralph Hay. Drift hamiltonian in magnetic coordinates. *Physics of Fluids (1958-1988)*, 25(3):575–576, 1982.

[63] Zhang Huasen and Lin Zhihong. Nonlinear generation of zonal fields by the beta-induced alfvn eigenmode in tokamak. *Plasma Science and Technology*, 15(10):969, 2013.

[64] Z. Wang. Gyrokinetic simulation of tae in fusion plasmas. *UC Irinve Ph.D dissertation*, 2014.

[65] Alexei Pankin, Douglas McCune, Robert Andre, Glenn Bateman, and Arnold Kritz. The tokamak monte carlo fast ion module {NUBEAM} in the national transport code collaboration library. *Computer Physics Communications*, 159(3):157 – 184, 2004.

[66] S.P Hirshman and O Betancourt. Preconditioned descent algorithm for rapid calculations of magnetohydrodynamic equilibria. *Journal of Computational Physics*, 96(1):99 – 109, 1991.

[67] J. P. Graves, I. Chapman, S. Coda, L.-G. Eriksson, and T. Johnson. Sawtooth-control mechanism using toroidally propagating ion-cyclotron-resonance waves in tokamaks. *Phys. Rev. Lett.*, 102:065005, Feb 2009.

[68] R. M. O. Galvão, P. H. Sakanaka, and H. Shigueoka. Influence of toroidal effects on the stability of the internal kink mode. *Phys. Rev. Lett.*, 41:870–873, Sep 1978.

[69] W. Kerner, R. Gruber, and F. Troyon. Numerical study of the internal kink mode in tokamaks. *Phys. Rev. Lett.*, 44:536–540, Feb 1980.

[70] J. Manickam. Stability of n = 1 internal modes in tokamaks. *Nuclear Fusion*, 24(5):595, 1984.

[71] F D Halpern, D Leblond, H Ltjens, and J-F Luciani. Oscillation regimes of the internal kink mode in tokamak plasmas. *Plasma Physics and Controlled Fusion*, 53(1):015011, 2011.

[72] G. Ara, B. Basu, B. Coppi, G. Laval, M.N. Rosenbluth, and B.V. Waddell. Magnetic reconnection and m = 1 oscillations in current carrying plasmas. *Annals of Physics*, 112(2):443 – 476, 1978.

[73] J. F. Drake. Kinetic theory of m=1 internal instabilities. *Physics of Fluids (1958-1988)*, 21(10):1777–1789, 1978.

[74] Hiroshi Naitou, Yusuke Yamada, Kenji Kajiwara, Wei li Lee, Shinji Tokuda, and Masatoshi Yagi. Global and kinetic mhd simulation by the gpic-mhd code. *Plasma Science and Technology*, 13(5):528, 2011.

[75] H. Qin, W. M. Tang, and G. Rewoldt. Linear gyrokinetic theory for kinetic magnetohydrodynamic eigenmodes in tokamak plasmas. *Physics of Plasmas (1994-present)*, 6(6):2544–2562, 1999.

[76] Yong Xiao, Ihor Holod, Zhixuan Wang, Zhihong Lin, and Taige Zhang. Gyrokinetic particle simulation of microturbulence for general magnetic geometry and experimental profiles. *Physics of Plasmas (1994-present)*, 22(2):022516, 2015.

[77] Lin Zhihong, S. Ethier, T. S. Hahm, and W. M. Tang. Verification of gyrokinetic particle simulation of device size scaling of turbulent transport. *Plasma Science and Technology*, 14(12):1125, 2012.

[78] J. P. Goedbloed and H. J. L. Hagebeuk. Growth rates of instabilities of a diffuse linear pinch. *Physics of Fluids (1958-1988)*, 15(6):1090–1101, 1972.

[79] Roger D Blandford and Roman L Znajek. Electromagnetic extraction of energy from kerr black holes. *Monthly Notices of the Royal Astronomical Society*, 179(3):433–456, 1977.

[80] Alan H Bridle and Richard A Perley. Extragalactic radio jets. *Annual review of astronomy and astrophysics*, 22:319–358, 1984.

[81] HC Spruit. Theory of magnetically powered jets. In *The Jet Paradigm*, pages 233–263. Springer, 2010.

[82] Vasily S Beskin. Magnetohydrodynamic models of astrophysical jets. *Physics-Uspekhi*, 53(12):1199, 2010.

[83] R.D. Blandford and D.G. Payne. Hydromagnetic flows from accretion discs and the production of radio jets. *Mon.Not.Roy.Astron.Soc.*, 199:883, 1982.

[84] Rachid Ouyed and Ralph E. Pudritz. Numerical simulations of astrophysical jets from keplerian disks. i. stationary models. *The Astrophysical Journal*, 482(2):712, 1997.

[85] G. V. Ustyugova, A. V. Koldoba, M. M. Romanova, V. M. Chechetkin, and R. V. E. Lovelace. Magnetocentrifugally driven winds: Comparison of mhd simulations with theory. *The Astrophysical Journal*, 516(1):221, 1999.

[86] R Do Blandford. Accretion disc electrodynamicsa model for double radio sources. *Monthly Notices of the Royal Astronomical Society*, 176(3):465–481, 1976.

[87] RVE Lovelace. Dynamo model of double radio sources. *Nature*, 262(5570):649, 1976.

[88] D Lynden-Bell. Magnetic collimation by accretion discs of quasars and stars. *Monthly Notices of the Royal Astronomical Society*, 279(2):389–401, 1996.

[89] GV Ustyugova, RVE Lovelace, MM Romanova, H Li, and SA Colgate. Poynting jets from accretion disks: Magnetohydrodynamic simulations. *The Astrophysical Journal Letters*, 541(1):L21, 2000.

[90] H Li, RVE Lovelace, JM Finn, and SA Colgate. Magnetic helix formation driven by keplerian disk rotation in an external plasma pressure: the initial expansion stage. *The Astrophysical Journal*, 561(2):915, 2001.

[91] RVE Lovelace, H Li, AV Koldoba, GV Ustyugova, and MM Romanova. Poynting jets from accretion disks. *The Astrophysical Journal*, 572(1):445, 2002.

[92] Michael L Norman, Jack O Burns, and Martin E Sulkanen. Disruption of galactic radio jets by shocks in the ambient medium. (335):146 – 149, 1988.

[93] Michael L Norman, Karl-Heinz A Winkler, and Larry Smarr. *Propagation and morphology of pressure-confined supersonic jets*. Springer, 1983.

[94] J Ma[a] Martí, E Müller, and J Ma[a] Ibanez. Hydrodynamical simulations of relativistic jets. *Astronomy and Astrophysics*, 281:L9–L12, 1994.

[95] David A Clarke. A consistent method of characteristics for multidimensional magnetohydrodynamics. *The Astrophysical Journal*, 457:291, 1996.

[96] G Bodo, P Rossi, S Massaglia, A Ferrari, A Malagoli, and R Rosner. Three-dimensional simulations of jets. *Astronomy and Astrophysics*, 333:1117–1129, 1998.

[97] Ian L Tregillis, TW Jones, and Dongsu Ryu. Synthetic observations of simulated radio galaxies. i. radio and x-ray analysis. *The Astrophysical Journal*, 601(2):778, 2004.

[98] JH Croston, MJ Hardcastle, DE Harris, E Belsole, M Birkinshaw, and DM Worrall. An x-ray study of magnetic field strengths and particle content in the lobes of fr ii radio sources. *The Astrophysical Journal*, 626(2):733, 2005.

[99] PP Kronberg, QW Dufton, H Li, and SA Colgate. Magnetic energy of the intergalactic medium from galactic black holes. *The Astrophysical Journal*, 560(1):178, 2001.

[100] B. I. Cohen, C. A. Romero-Talams, D. D. Ryutov, E. B. Hooper, L. L. LoDestro, H. S. McLean, T. L. Stewart, and R. D. Wood. The role of the n=1 column mode in spheromak formation. *Physics of Plasmas (1994-present)*, 16(4):042501, 2009.

[101] Henry K. Moffatt. Field generation in electrically conducting fluids. 1978.

[102] A Al-Karkhy, PK Browning, G Cunningham, SJ Gee, and MG Rusbridge. Observations of the magnetohydrodynamic dynamo effect in a spheromak plasma. *Physical review letters*, 70(12):1814, 1993.

[103] Yang Chen, Scott E. Parker, J. Lang, and G.-Y. Fu. Linear gyrokinetic simulation of high-n toroidal alfvn eigenmodes in a burning plasma. *Physics of Plasmas (1994-present)*, 17(10):102504, 2010.

[104] Jeffery Freidberg. Ideal magnetohydrodynamics. 1987.

[105] Yasutaro Nishimura, Z Lin, JLV Lewandowski, and S Ethier. A finite element poisson solver for gyrokinetic particle simulations in a global field aligned mesh. *Journal of Computational Physics*, 214(2):657–671, 2006.

Appendix A

Shooting Method

A.1 Formulation

This appendix describes an MHD eigenmode formulation used to benchmark with GTC simulations of the internal kink mode in cylindrical geometry. To construct the eigenmode code, we follow the formulation and notation in *Ideal Magnetohydrodynamics* written by Jeffery Freidberg[104]. This eigenmode code uses cylindrical coordinates (r, θ, z). The equilibrium axial magnetic field B_z, poloidal magnetic field B_θ, and equilibrium pressure p_0 are required for this formulation and can be solved for using the screw pinch force balance equation, as will be shown in subsection A.2.

Taking a single poloidal mode number m and axial wave number k, the linear ideal MHD equations can be reduced to a 1D differential equation as derived by Goedbloed et al[78]. The variable being solved for is the MHD displacement function $\boldsymbol{\xi} = \xi\hat{\boldsymbol{r}} + \xi_{||}\hat{\boldsymbol{b}} + \eta\hat{\boldsymbol{\eta}}$, where

$\hat{\boldsymbol{b}} = \left(B_z\hat{\boldsymbol{z}} + B_\theta\hat{\boldsymbol{\theta}}\right)/B_0$ and $\hat{\boldsymbol{\eta}} = \hat{\boldsymbol{r}} \times \hat{\boldsymbol{b}} = \left(B_z\hat{\boldsymbol{\theta}} - B_\theta\hat{\boldsymbol{z}}\right)/B_0$. To simplify the notation we define the following terms:

$$\begin{aligned} F &= \mathbf{k} \cdot \mathbf{B}_0 = kB_z + mB_\theta/r \\ G &= \hat{\mathbf{r}} \cdot \mathbf{k} \times \mathbf{B}_0 = mB_z/r + kB_\theta. \end{aligned} \tag{A.1}$$

The terms F and G might be better known in other notations as $k_{||}$ and $k_\perp - k_r$, respectively. The sound speed V_s, the Alfvén speed V_a, and α are defined as:

$$\begin{aligned} V_s^2 &= \gamma p_0/\rho, \\ V_a^2 &= B_0^2/\mu_0\rho, \\ \alpha^2 &= \frac{4V_s^2\omega_a^2}{k_0^2(V_s^2 + V_a^2)}, \end{aligned} \tag{A.2}$$

where the variable γ is the ratio of specific heats, ρ is the mass density, and $k_0^2 = m^2/r^2 + k^2$. The following frequencies are defined as:

$$\begin{aligned} \omega_a^2 &= \frac{F^2}{\mu_0\rho}, \\ \omega_h^2 &= \left(\frac{V_s^2}{V_s^2 + V_a^2}\right)\omega_a^2, \\ \omega_g^2 &= \frac{V_s^2}{V_a^2}\omega_a^2, \\ \omega_{f,s} &= \frac{1}{2}[k_0^2(V_s^2 + V_a^2)][1 \pm \sqrt{1 - \alpha^2}]. \end{aligned} \tag{A.3}$$

We can use the generalized Hain-Lust Equation[78], which reduces the ideal MHD equations in a screw pinch equilibrium to a single 1D equation assuming there is a single poloidal mode m and a single axial wavenumber k_z. The 1-dimensional eigenmode Hain-Lust equation is:

$$\frac{d}{dr}\big[A\frac{d}{dr}(r\xi)\big] - C(r\xi) = 0 \tag{A.4}$$

where,

$$A = \left[\frac{\rho(V_s^2 + V_a^2)}{r}\right]\frac{(\omega^2 - \omega_a^2)(\omega^2 - \omega_h^2)}{(\omega^2 - \omega_f^2)(\omega^2 - \omega_s^2)} \tag{A.5}$$

and,

$$C = -\frac{\rho}{r}(\omega^2 - \omega_a^2) + \left(\frac{4k^2V_a^2B_\theta^2}{\mu_0 r^3}\right)\frac{(\omega^2 - \omega_g^2)}{(\omega^2 - \omega_f^2)(\omega^2 - \omega_s^2)} + \frac{d}{dr}\left[\frac{B_\theta^2}{\mu_0 r^2} - \left(\frac{2kB_\theta^2 G}{\mu_0 r^2}\right)\frac{(V_a^2 + V_s^2)(\omega^2 - \omega_h^2)}{(\omega^2 - \omega_f^2)(\omega^2 - \omega_s^2)}\right]. \tag{A.6}$$

The other two vector quantities of the displacement function can be written in terms of the radial displacement function.

$$\xi_\parallel = -\left(\frac{i\gamma p_0 F}{r\rho B(\omega^2 - \omega_f^2)(\omega^2 - \omega_s^2)}\right)\left[(\omega^2 - \omega_a^2)(r\xi)' + \left(\frac{2kGB_\theta}{\mu_0\rho}\right)\xi\right] \tag{A.7}$$

$$\eta = -\left(\frac{i}{r\rho B(\omega^2 - \omega_f^2)(\omega^2 - \omega_s^2)}\right)\left[G\left(\gamma p_0 + \frac{B^2}{\mu_0}\right)(\omega^2 - \omega_h^2)(r\xi)' + \frac{2kB^2B_\theta}{\mu_0}(\omega^2 - \omega_g^2)\xi\right] \tag{A.8}$$

In order to solve the Hain-Lust eigenmode(Equation A.4), we must supply the boundary conditions. Assuming a conducting wall, ξ must be zero at the outer boundary. For the inner boundary, if we take a power series of ξ about the origin, we find that:

$$\xi \sim r^{|m|-1}$$

.

For the $m = 1$ mode, approaching the $r = 0$ boundary, ξ will be approximately constant in r, and ξ' approaches zero.

$$\xi(0) = 1 \quad , \quad \xi'(0) = 0$$

With these boundary conditions, the shooting method can be used, which reduces the boundary value problem into an initial value problem to find the correct growth rate and the eigenmode structure. This is done by picking an initial guess for the frequency ω, and narrows the guess down down until a mode structure that satisfies the outer boundary condition $\xi(a) = 0$ is found.

A.2 Testing Eigenmode Formulation

To make sure that the results from this eigenmode code are correct, it is benchmarked against the solution by Goedbloed and Hagebuek[78] in this section. The magnetic field configuration used in this benchmark is a Lundquist field:

$$\begin{aligned} B_z &= B_0 J_0(\nu r), \\ B_\theta &= B_0 J_1(\nu r), \end{aligned} \tag{A.9}$$

where J_0 & J_1 are Bessel functions, and B_0 is the on-axis magnetic field. In Figure A.1, while setting $\nu a = 8$, the growth rate of the internal kink mode is calculated for various values of k/ν. The growth rate scan with our MHD eigenmode code matches the result from Goedbloed et al[78].

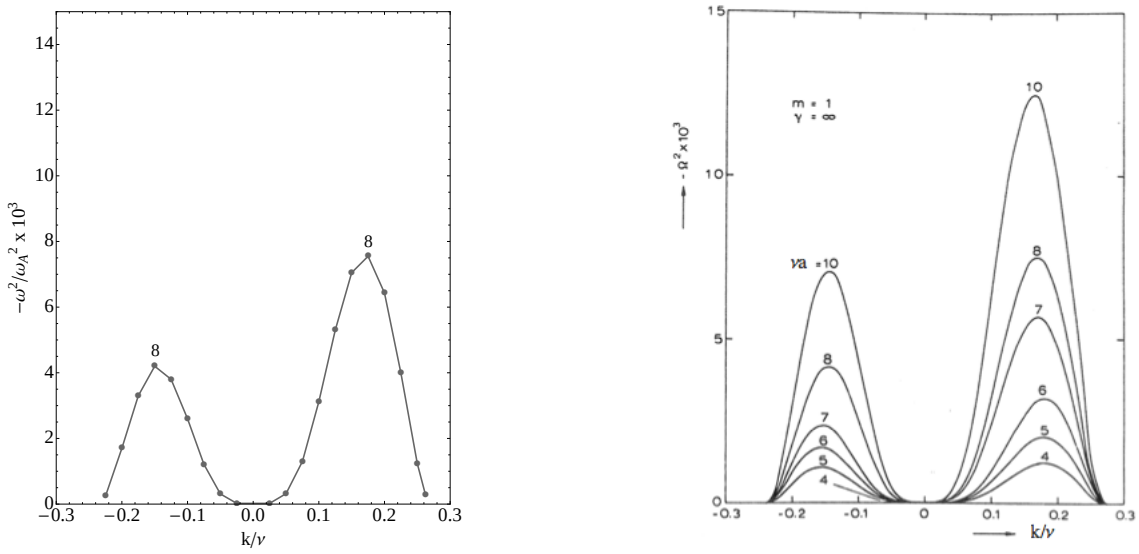

Figure A.1: Growth rate of the m=1 internal kink mode with $\nu = 8$ for various k/ν from the 1D MHD eigenmode code on the left, the result from Goedbloed et al. on the right[78]. The figure from Goedbloed et al. is reprinted with permission from AIP Publishing LLC.

In Figure A.2, the mode structure of the internal kink mode for $\nu a = 8.0$ and $k/\nu = 0.2$ is shown. The mode structures from the eigenmode code and Goedbloed et al.[78] are the same, verifying this eigenmode code.

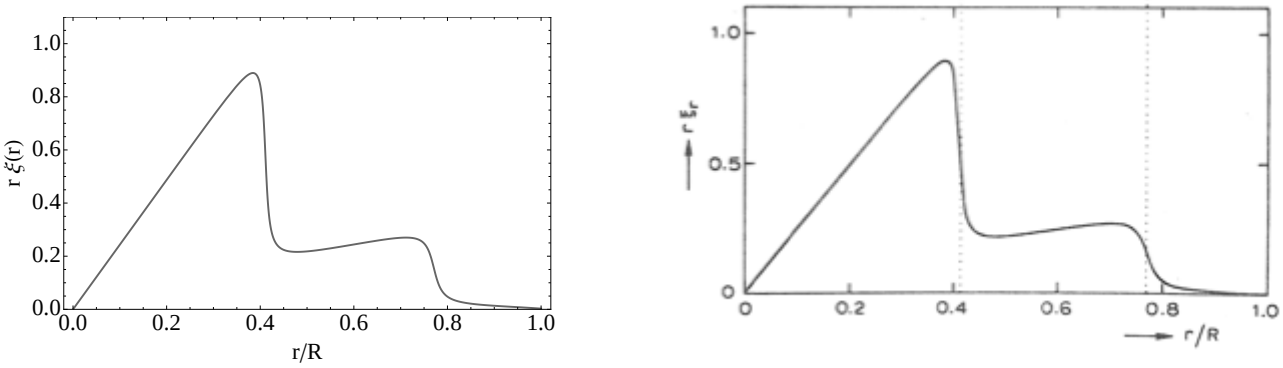

Figure A.2: The MHD eigenmode code mode structure of $r\xi(r)$ is plotted on the left, the result from Goedbloed et al. on the right[78]. The figure from Goedbloed et al. is reprinted with permission from AIP Publishing LLC.

A.3 Eigenmode formulation in Cylinder

This eigenmode code requires the screw pinch force balance equation to be satisfied. To obtain the fields B_θ and B_z, the desired safety factor $q = \frac{rB_z}{R_0 B_\theta}$ and pressure profile p_0 are substituted into the screw pinch force balance equation. These two profiles reduce the force balance equation to a 1D ordinary differential equation, as shown below.

$$\frac{d}{dr}\left(p_0(r) + \frac{B_\theta^2(r) + q^2(r)R_0^2/r^2 B_\theta^2(r)}{2\mu_0}\right) + \frac{B_\theta^2(r)}{\mu_0 r} = 0 \tag{A.10}$$

This equation can be numerically solved for the equilibrium poloidal field B_θ, and subsequently the equilibrium axial field B_z. Choosing $a/R_0 = 1/2$, $m = 1$, $k = -1/R_0$, and $q(r) = .8 + .8\frac{r^2}{a^2}$, the eigenmode equation can be solved and has the displacement

function ξ shown in Figure A.3 for various inverse aspect ratios a/R_0. Note that the sharp resonant layer of $\xi(r)$ at the mode rational $q = 1$ surface is broader for the low aspect ratio cases. This means that the low aspect ratio cases are easier to simulate since they require less resolution near the mode rational surface.

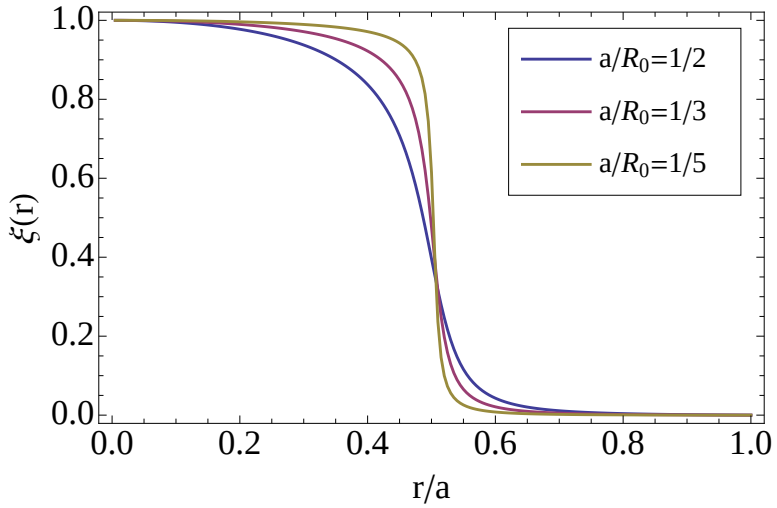

Figure A.3: The radial mode structure of the MHD displacement function ξ is plotted for inverse aspect ratios of $a/R_0 = 1/2, 1/3, 1/5$.

The displacement function ξ is not used in the gyrokinetic equations. To benchmark mode structures between GTC and this eigenmode code, the parallel magnetic potential $\delta A_{||}$ and the electrostatic potential $\delta\phi$ are computed from ξ. Using Ampere's Law, Faraday's Law, ideal Ohm's Law, and assuming that the parallel magnetic field is small such that the magnetic vector potential $\delta\mathbf{A}$ is in the direction parallel to the equilibrium magnetic field $\delta\mathbf{B} = \nabla \times \delta A_{||}\mathbf{b}_0$, the equation to solve for $\delta A_{||}$ is formed:

$$\delta\mathbf{J} = \nabla \times (\nabla \times \delta A_{||}\mathbf{b}_0) = \nabla \times (\nabla \times (\boldsymbol{\xi} \times \mathbf{B_0})). \tag{A.11}$$

Choosing the boundary conditions to be $\delta A_{||}(r = 0)) = 0$ and $\delta A_{||}(r = a)) = 0$, the shooting method is used again to solve for $\delta A_{||}$.

The electrostatic potential can be solved using the equation for the perturbed radial electric field.

$$\nabla\phi \cdot \hat{\boldsymbol{r}} = -\left(\gamma \boldsymbol{\xi} \times \mathbf{B}_0\right) \cdot \hat{\boldsymbol{r}} \tag{A.12}$$

The mode structure of $\delta A_{||}$ and $\delta\phi$ are shown in Figure A.4

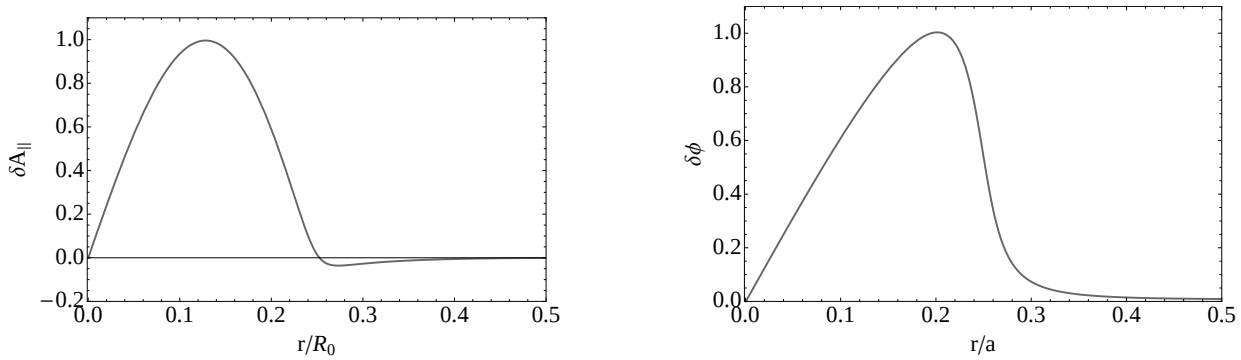

Figure A.4: The mode structure of $\delta A_{||}$ vs. radial coordinate r/R_0 is plotted on the left. The mode structure of $\delta\phi$ is on the right.

Appendix B

Finite Element method implementation for GTC

B.1 Introduction

This appendix describes the implementation of the finite element method in GTC for the gyrokinetic Poisson equation and the gyrokinetic Ampere's Law. The presented material is based on the 2006 finite element paper by Nishimura[105], and will extend the formulation to include toroidicity and electromagnetic simulations.

B.2 Calculation of triangular mesh

When performing finite elements, a triangular mesh that connects the computational grid points is required, and it is important to ensure that the mesh is well formed. A common method of mesh generation is Delaunay triangulation. This method has a strict limit that any two neighboring triangles have their sum of their opposing angles be less than 180

degrees, called the Delaunay condition. Delaunay triangulation is robust in that it makes no assumption on the structure of the grid, however this method can be fairly complicated to implement.

Using the knowledge of how the grid is formed, a more simple method of triangulation is implemented into GTC. The grid point generation algorithm that is used in GTC sets a number radial grid points that are evenly spaced in radial coordinate r, where r is the minor radius. The number of grid points in the poloidal direction θ is chosen such that it ensures that the arc-length between poloidal grid points is approximately constant on each flux surface. This grid creation method turns out to be advantageous for the finite element method, since it helps the grid points be evenly spaced which helps the triangular mesh be well formed. When the radial grid length and poloidal arc length are approximately even, the triangles produced by this method obey the Delaunay condition.

To interpolate solutions between grid points, a linear shape function $S^{(e)}$ is used.

$$S^{(e)} = \frac{1}{4\Delta^{(e)}} \left[(x_i y_k - x_k y_j) + (y_j - y_k)\, x + (x_k - x_j)\, y \right], \tag{B.1}$$

where x and y are the Cartesian coordinates, the subscript i, j, k represent the three grid points that form a triangular element, and $\Delta^{(e)}$ is the area of the triangular element e.

$$\Delta^{(e)} = \frac{1}{2} \left[(x_i - x_k)(y_j - y_k) - (x_k - x_j)(y_k - y_i) \right] \tag{B.2}$$

The calculation of the triangular mesh is done between two flux surfaces at a time. The first triangle is created by taking one point on the inner flux surface, then finding the nearest two

points on the outer flux surface. The quality of shape of each potential triangle is considered by calculating the sum of the square of the length of each side of the triangle as shown below,

$$P = \left((x_i - x_j)^2 + (y_i - y_j)^2\right) + \left((x_k - x_j)^2 + (y_k - y_j)^2\right) + \left((x_i - x_k)^2 + (y_i - y_k)^2\right). \quad \text{(B.3)}$$

The triangle with the smallest value of P is usually the best shaped triangle. Minimizing this function is similar to minimizing the perimeter of the triangle, but there is an extra emphasis of having a triangle with sides of similar length. Applying the constraint that two vertices on the next triangle are fixed and that the third vertex has a similar arc length away from the other two vertices, the triangle with a smaller value of P is most likely the better shaped triangle.

Subsequent triangles are calculated by examining the next point in the poloidal direction on both the inner and outer flux surfaces, and the better formed triangle is chosen by minimizing P. This is demonstrated in Figure B.1, where the potential triangle 1 would have the smaller value of P, and be chosen because of its better shape.

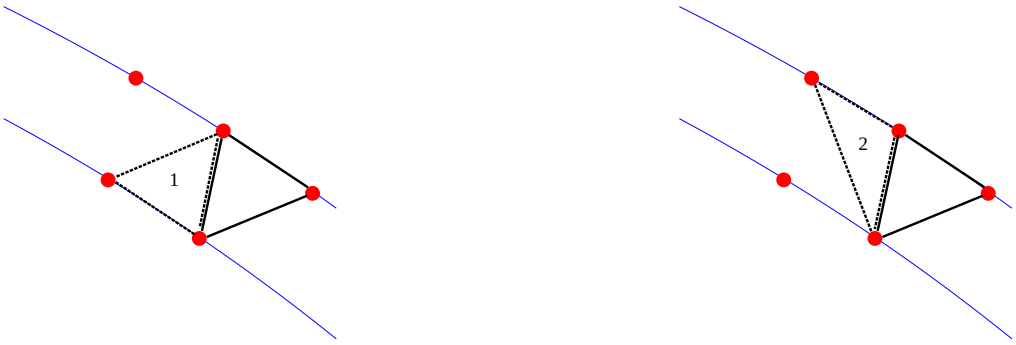

Figure B.1: The original triangle pick in between two flux surfaces is plotted with solid lines, and the next two potential triangles are plotted with dotted lines.

This process is repeated until the entire region between the two flux surfaces is filled, then the entire process is repeated for the rest of the flux surfaces until the entire domain is filled. In Figure B.2, the triangular mesh of the first twenty flux surfaces are plotted. Note that all the triangles on this plot have no angles greater than 90 degrees, automatically satisfying the Delaunay condition.

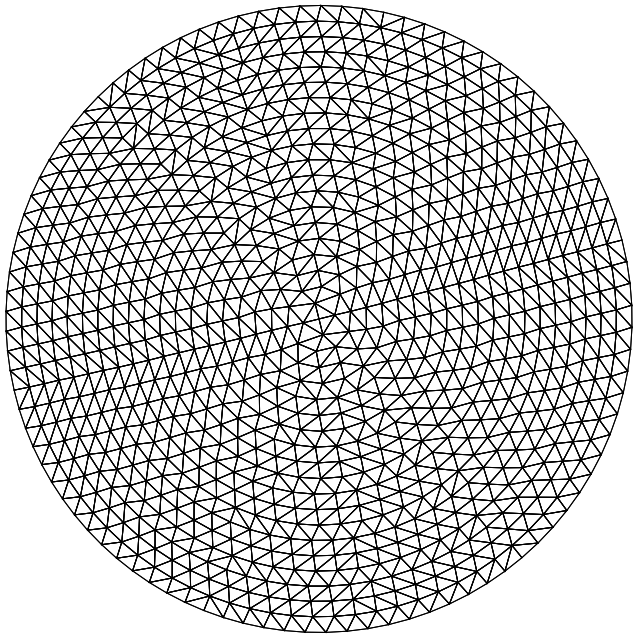

Figure B.2: The triangular mesh of the first twenty flux surfaces are plotted.

B.3 Setup of FEM equations

This section will describe the equations that are solved using finite element method and the construction of the finite element matrix. The equation being solved using finite elements is the gyrokinetic Poisson equation and Ampere's law, which have the form:

$$\nabla_{\perp}^{2} A = b. \tag{B.4}$$

The variables A and b are dummy variables. Note that finite Larmor radius term $\nabla_\perp^2 \rho_i^2 (Z_i \langle \delta n_i \rangle - \delta n_e)$ in the gyrokinetic Poisson equation is ignored for this Appendix to simplify the description of the equations, but it has been added in the code. The perpendicular Laplacian is approximately:

$$\nabla_\perp^2 = \frac{\partial^2}{\partial x^2} + \frac{\partial^2}{\partial y^2}, \tag{B.5}$$

in cylindrical coordinates, and

$$\nabla_\perp^2 = \frac{1}{x}\frac{\partial}{\partial x}\left(x\frac{\partial}{\partial x}\right) + \frac{\partial^2}{\partial y^2}, \tag{B.6}$$

in toroidal coordinates. The finite element matrix can be written in the form:

$$\sum_{j=1}^{N} L_{ij} A_j = d_{ij} b_j. \tag{B.7}$$

For toroidal geometry, the quantities L_{ij} and d_{ij} are:

$$L_{ij} = \frac{1}{4\Delta^{(e)}} \left(b_i b_j + c_i c_j\right) x_i \,, \tag{B.8}$$

$$d_{ij} = \frac{\Delta^{(e)}}{12} \left(\delta_{ij} + 1\right) x_i. \tag{B.9}$$

The variables in Equation B.8 are as follows: $b_i = y_j - y_k$, and $c_i = x_k - x_j$. In cylindrical geometry, the L_{ij} and d_{ij} matrices would not have the x_i term in Equations B.8 and B.9. For one triangle element e with vertices i, j, k, the matrix term in Equations B.8 and B.9 are:

$$\begin{pmatrix} L_{ii} & L_{ij} & L_{ik} \\ L_{ji} & L_{jj} & L_{jk} \\ L_{ki} & L_{kj} & L_{kk} \end{pmatrix} \begin{pmatrix} A_1 \\ A_2 \\ A_3 \end{pmatrix} = \begin{pmatrix} d_{ii} & d_{ij} & d_{ik} \\ d_{ji} & d_{jj} & d_{jk} \\ d_{ki} & d_{kj} & d_{kk} \end{pmatrix} \begin{pmatrix} b_i \\ b_j \\ b_k \end{pmatrix}. \tag{B.10}$$

To construct the final Laplacian matrix, the sum of all matrix elements are taken. The gyrokinetic Poisson equation, using the Padé approximation is:

$$\nabla_\perp^2 \delta\phi = \delta n, \tag{B.11}$$

where $\delta\phi$ is the electrostatic potential, and δn is the charge density. For the gyrokinetic Poisson equation, since $b_{ij} = \delta n$ is a know quantity, the right hand side can be simplified by matrix multiplication.

$$\begin{pmatrix} L_{ii} & L_{ij} & L_{ik} \\ L_{ji} & L_{jj} & L_{jk} \\ L_{ki} & L_{kj} & L_{kk} \end{pmatrix} \begin{pmatrix} \delta\phi_i \\ \delta\phi_j \\ \delta\phi_k \end{pmatrix} = \begin{pmatrix} d_i^{(e)} \\ d_j^{(e)} \\ d_k^{(e)} \end{pmatrix} \tag{B.12}$$

where $d_i^{(e)} = \frac{\Delta^{(e)}}{12}\left[2\delta n_i + \delta n_j + \delta n_k\right]$. This equation can then be solved for the electrostatic potential $\delta\phi$ using PETSc.

Gyrokinetic Ampere's law can be written as,

$$\delta u_{||} = \nabla_{\perp}^2 \delta A_{||}, \tag{B.13}$$

where $\delta u_{||}$ is the parallel charge flow, and $\delta A_{||}$ is the parallel magnetic vector potential. For Ampere's Law, when using the hybrid electron model, the electron current is the physical quantity that is being solved for, as shown below. This means that the finite element method matrix equations have to be reformed for Ampere's law where $b_{ij} = \delta u_{||}$ is solved for. Since

$\delta A_{||}$ is known, the Laplacian matrix L_{ij} can be multiplied by $\delta A_{||}$ to form the right side of the equation.

$$\begin{pmatrix} L_1^{(1)} \\ L_2^{(1)} \\ L_3^{(1)} \end{pmatrix} = \begin{pmatrix} d_{11} & d_{12} & d_{13} \\ d_{21} & d_{22} & d_{23} \\ d_{31} & d_{32} & d_{33} \end{pmatrix} \begin{pmatrix} \delta u_{||1} \\ \delta u_{||2} \\ \delta u_{||3} \end{pmatrix} \tag{B.14}$$

where $L_i^{(e)}$ is L_{ij} matrix multiplied by $\delta A_{||}$. In this form, the paralle charge flow δu is solved for using PETSc.

Appendix C

Extending the simulation to the magnetic axis

In this appendix, a detailed explanation of the extrapolation method used in the internal kink mode simulations in Chapter 4 and 5 is given. The magnetic axis is important to simulate for internal kink modes, since the $m = 1$, $n = 1$ internal kink mode structure has finite value near the magnetic axis. Currently, GTC uses the finite differences method to calculate the two dimensional perpendicular Laplacian for the gyrokinetic Poisson equation and Ampere's law. The perpendicular Laplacian is

$$\begin{aligned}\nabla_{\perp}^{2}F =& g^{\psi\psi}\frac{\partial^{2}F}{\partial\psi^{2}} + 2g^{\psi\theta}\frac{\partial^{2}F}{\partial\psi\partial\theta} + \left(g^{\theta\theta} + g^{\zeta\zeta}/q^{2}\right)\frac{\partial^{2}F}{\partial\theta_{0}^{2}} + \\ & \frac{1}{\mathcal{J}}\left(\frac{\partial\mathcal{J}g^{\psi\psi}}{\partial\psi} + \frac{\partial\mathcal{J}g^{\psi\theta}}{\partial\theta}\right)\frac{\partial F}{\partial\psi} + \frac{1}{\mathcal{J}}\left(\frac{\partial\mathcal{J}g^{\psi\theta}}{\partial\psi} + \frac{\partial\mathcal{J}g^{\psi\psi}}{\partial\theta}\right)\frac{\partial F}{\partial\theta},\end{aligned} \tag{C.1}$$

where ψ is the magnetic poloidal flux, θ magnetic poloidal angle, and ζ is the magnetic toroidal angle. In the above equation, the contravariant tensor is defined as $g^{\alpha\beta} \approx \nabla\alpha \cdot \nabla\beta$,

where α and β are any combination of the magnetic coordinates ψ, θ, or ζ. The computational grid is evenly spaced in poloidal angle θ_0, and is nonuniformly spaced in poloidal magnetic flux coordinate ψ. The differencing of the derivatives with respect to ψ and θ are given below for a location with radial grid point i and poloidal grid point j.

$$\begin{aligned}
\frac{\partial F}{\partial \psi} &= w_2 \frac{F_{i+1,j^*} - F_{i,j}}{h_2} + w_1 \frac{F_{i,j} - F_{i-1,j^*}}{h_1} \\
\frac{\partial^2 F}{\partial \psi^2} &= \frac{2}{h_1 h_2}(w_1 F_{i-1,j^*} + w_2 F_{i+1,j^*} - F_{i,j}) \\
\frac{\partial F}{\partial \theta} &= \frac{F_{i,j+1} - F_{i,j-1}}{2\Delta\theta} \\
\frac{\partial^2 F}{\partial \theta^2} &= \frac{F_{i,j+1} - 2F_{i,j} + F_{i,j-1}}{\Delta\theta^2} \\
\frac{\partial^2 F}{\partial \theta \partial \psi} &= \left(\frac{w_1}{h_1} - \frac{w_2}{h_2}\right) \frac{F_{i,j+1} - F_{i,j-1}}{2\Delta\theta} + \frac{w_2}{h_2}\frac{\partial F_{i+1}}{\partial \theta_0} + \frac{w_1}{h_1}\frac{\partial F_{i-1}}{\partial \theta_0}
\end{aligned} \tag{C.2}$$

The variables are defined as: $\Delta\theta = \theta_i - \theta_{i-1}$, $h_1 = \psi_i - \psi_{i-1}$, $h_2 = \psi_{i+1} - \psi_i$, $w_1 = h_2/(h_1+h_2)$, and $w_2 = 1 - w_1$.

Due to the choice of magnetic flux coordinate system, there are some numerical difficulties solving the Laplacian near the magnetic axis($\psi = 0$). These numerical difficulties are most problematic for low poloidal mode number m modes.

C.1 Extrapolating to the magnetic axis

In this section, a method to extrapolate the solutions of $\nabla_\perp^2$ near the magnetic axis to avoid numerical error is discussed. We can solve the Laplacian up to a certain point using finite differences, then use a linear radial boundary condition for the transition point between the finite differences region. This transition point for the extrapolation region will be called "FD

Boundary" for short. Solutions can be extrapolated from the lowest order Bessel function J_m to the magnetic axis.

$$\nabla^2 J_m(\alpha r)\cos(\theta-\zeta) \approx cJ_m(\alpha r)\cos(m\theta-\zeta) \tag{C.3}$$

We can use this relationship to extrapolate the behavior of $\delta\phi$ and $\delta A_{||}$ near the magnetic axis for $m = 0, 1$ modes. Expanding near the magnetic axis, the Bessel functions are approximately:

$$J_0(\alpha r) \approx 1 - (\alpha^2 r^2/2), \tag{C.4}$$

and

$$J_1(\alpha r) \approx \alpha r/2 - (\alpha^3 r^3/16). \tag{C.5}$$

If close enough to the magnetic axis, $\alpha r << 1$, only the lowest order solution needs to be kept. Fourier decomposing the "FD Boundary" surface, we can project the lowest order solution to the magnetic axis. The boundary surface will be referred to as $i = l$ in equations.

$$\begin{aligned} a_0 &= \frac{1}{m}\sum_j^m F_{i=l,j} \\ a_1 &= \frac{2}{m}\sum_j^m F_{i=l,j}\cos(2\pi i/m) \\ b_1 &= \frac{2}{m}\sum_j^m F_{i=l,j}\sin(2\pi i/m) \end{aligned} \tag{C.6}$$

With the Fourier coefficients a_0, a_1, and b_1, the Laplacian near the magnetic axis is approximated as:

$$\nabla_\perp F = a_0 + a_1\frac{r}{r_l}\cos\theta_i + b_1\frac{r}{r_l}\sin\theta_i. \tag{C.7}$$

C.2 Changes to the size of Laplacian matrix

To explain the changes made to the Laplacian matrix in GTC, we use an example of the Laplacian matrix for a simple uniform 1D grid with only four grid points as shown below.

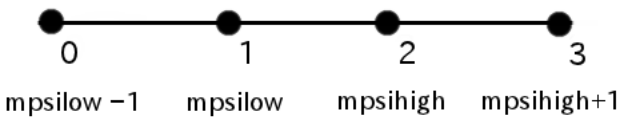

Figure C.1: 1D grid for simple Laplacian matrix example.

The finite differences 1D Laplacian is:

$$\nabla^2 F = \frac{d^2 F}{dx^2} = \frac{F_{i+1} - 2F_i + F_{i-1}}{\Delta x}. \tag{C.8}$$

Considering only zero boundary conditions for simplicity, the first and the last grid points are set to be zero. The previous method for handling the Laplacian matrix would be to have a 4×4 matrix where the boundary points in the matrix Ξ are very large numbers. Ξ being a very large forces F to be very small when solving the matrix equation, effectively setting the boundaries to zero.

$$\nabla^2_\perp F = \frac{1}{\Delta x^2} \begin{pmatrix} \Xi & 0 & 0 & 0 \\ 1 & -2 & 1 & 0 \\ 0 & 1 & -2 & 1 \\ 0 & 0 & 0 & \Xi \end{pmatrix} \begin{pmatrix} F_0 \\ F_1 \\ F_2 \\ F_3 \end{pmatrix} \tag{C.9}$$

Having Ξ in the matrix allows for only the possibility of zero boundaries. For the new version, the boundaries were removed from the matrix and explicitly set F_0 and F_3 to zero. For this simple example, instead of having a 4×4 matrix, we would then only have a 2×2 matrix.

$$\nabla^2_\perp F = \frac{1}{\Delta x^2} \begin{pmatrix} -2 & 1 \\ 1 & -2 \end{pmatrix} \begin{pmatrix} F_1 \\ F_2 \end{pmatrix} \tag{C.10}$$

C.3 New boundary conditions

For GTC, the radial boundaries were previously set to zero. The inner and outer radial boundary would be expressed as Ξ in the old matrix, and would no longer be included in the new matrix form. Having the matrix without the inner and outer boundary allows us to implement different boundary conditions as desired; e.g. for external kink modes, peeling ballooning modes, etc.

For the inner flux surface boundary, there is no $l-1$ term in the matrix. We can remove dependance of the $l-1$ term by assuming the solution is linear in r. This gives us the equation:

$$F_{l-1,j^*} = 2F_{l,j} - F_{l+1,j^*}. \tag{C.11}$$

Plugging in Equation C.11 into the finite difference equations:

$$g^{\psi\psi}\frac{\partial^2 F}{\partial \psi^2} = \frac{2g^{\psi\psi}}{h_1 h_2}\{(2w_1 - 1)F_{l,j} + (w_2 - w_1)F_{l+1,j^*}\}, \tag{C.12}$$

$$\frac{1}{\mathcal{J}}\left(\frac{\partial \mathcal{J} g^{\psi\psi}}{\partial \psi} + \frac{\partial \mathcal{J} g^{\psi\theta}}{\partial \theta_0}\right)\frac{\partial F}{\partial \psi} = \frac{1}{\mathcal{J}}\left(\frac{\partial J g^{\psi\psi}}{\partial \psi} + \frac{\partial \mathcal{J} g^{\psi\theta}}{\partial \theta_0}\right)\left(\frac{w_1}{h_1} + \frac{w_2}{h_2}\right)\left(F_{l+1,j^*} - F_{l,j}\right), \tag{C.13}$$

$$2g^{\psi\theta}\frac{\partial^2 F}{\partial\psi\partial\theta} = 2g^{\psi\theta}\left(\frac{w_1}{h_1}+\frac{w_2}{h_2}\right)\left(-\frac{F_{l,j+1}-F_{l,j-1}}{2\Delta\theta_i}+\frac{\partial F_{l+1,j^*}}{\partial\theta_0}\right). \tag{C.14}$$

Note that the $\frac{\partial F}{\partial\theta}$ and $\frac{\partial^2 F}{\partial\theta^2}$ terms were not explicitly rewritten out again since they remain unchanged as they have no differencing in the radial direction.

Appendix D

Increasing order of the spline algorithm for analytic equilibria

For implementation of the realistic toroidal geometry equilibrium, the Cartesian coordinates $X(\psi, \theta)$ and $Z(\psi, \theta)$ are approximated for construction of a 2D spline. This is done because of the need to transform from the geometric poloidal coordinate θ_0 to the magnetic poloidal coordinate θ.

$$\theta = \theta_0 + \epsilon\theta_0 \tag{D.1}$$

While the equilibrium is only of order $\epsilon = a/R_0$, this transformation of the spline coefficients from geometric coordinate to magnetic coordinate must be of higher order to preserve the

circular cross-section of the equilibrium. Previously, the X and Z spline corrections were only taken to second order in ϵ, as shown below.

$$\begin{aligned} X =& \epsilon \cos\theta_0 \\ =& \epsilon \cos(\theta - \epsilon \sin\theta) \\ \approx& \epsilon \cos\theta - \epsilon^2 \sin^2\theta \end{aligned} \tag{D.2}$$

$$\begin{aligned} Z =& \epsilon \sin\theta_0 \\ =& \epsilon \sin(\theta - \epsilon \sin\theta) \\ \approx& \epsilon \cos\theta + \epsilon^2 \sin\theta \cos\theta \end{aligned} \tag{D.3}$$

Panel(a) of Figure D.1 shows the last flux surface both analytically and using the X and Z splines that keep only second order corrections in the transformation from geometric to magnetic coordinate. The error produced from only keeping the second order correction is quite significant. This suggests that higher order corrections must be kept to maintain concentric flux surfaces. The X and Z splines with the third order ϵ correction is shown below.

$$\begin{aligned} X &\approx \epsilon \cos\theta - \epsilon^2 \sin^2\theta - 1/2\epsilon^3 \sin^2\theta \cos\theta \\ Z &\approx \epsilon \sin\theta - \epsilon^2 \sin\theta \cos\theta - 1/2\epsilon^3 \sin^3\theta \end{aligned} \tag{D.4}$$

Panel(b) of Figure D.1 shows the last flux surface keeping third order corrections has much better agreement than only keeping second order corrections.

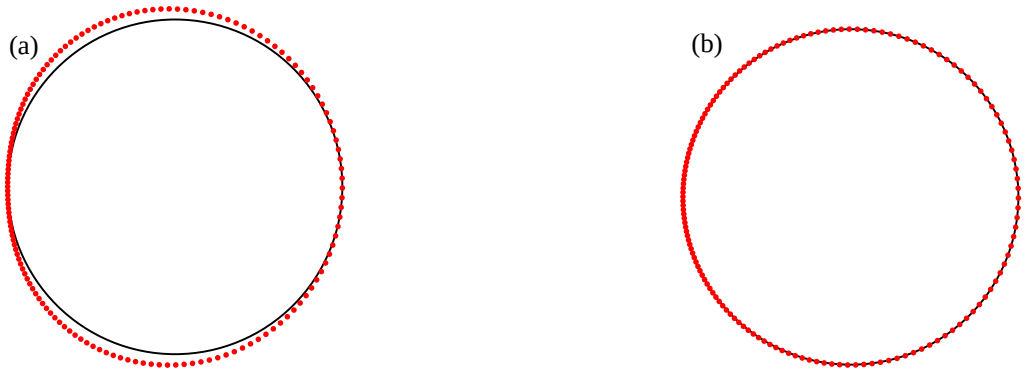

Figure D.1: The last flux surface is plotted in the X-Z plane. The black line represents the analytic value for the last flux surface $r = a$. The red dots represent the last flux surface using the X and Z splines. Panel(a) keeps second order correction for X and Z splines in ϵ. Panel(b) keeps third order corrections for X and Z splines.

The same procedure is also performed for the magnetic field spline. Previously the magnetic field spline only kept ϵ^2 corrections, and dropped any higher order terms as shown below.

$$B = 1 - X + \epsilon^2 \cos^2\theta \tag{D.5}$$

This causes a distortion in the magnetic field strength, which can be seen in panel(a) of Figure D.2. To remove this distortion of the magnetic field, we can write the magnetic field as second order in ϵ while using the geometric coordinate, then keep higher order ϵ terms associated with the coordinate transformation. When this is done, the magnetic field is no longer distorted which can be seen in panel(b) of Figure D.2.

$$\begin{aligned} B =& 1 - \epsilon\cos\theta_0 + \epsilon^2\cos^2\theta_0 \\ =& 1 - X + X^2 \end{aligned} \tag{D.6}$$

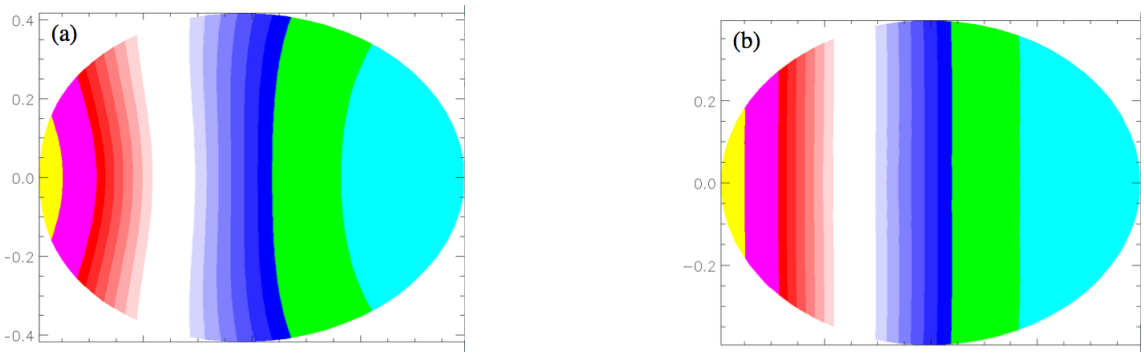

Figure D.2: Panel(a): The magnetic field B_0 is plotted keeping second order corrections is ϵ for X and Z splines while using the magnetic coordinate θ_0. Panel(b): The equilibrium magnetic field is plotted keeping third order corrections is ϵ for X and Z splines while using the geometric coordinate θ_0.